EUROPEAN ORGANIZATION FOR NUCLEAR RESEARCH

CERN-SPSC-2013-XX
SPSC-EOI-007-Add.1

Proposal
for large-scale neutrino detectors prototyping and phased performance assessment in view of a long-baseline oscillation experiment (LBNO-Proto)

Author list under construction

(Dated: June 23, 2013, **Version 1.1**)

Under submission to the SPSC

Executive Summary

In June 2012, an Expression of Interest for a long-baseline experiment (LBNO) [1] has been submitted to the CERN SPSC and is presently under review. LBNO considers three types of neutrino detector technologies: a double-phase liquid argon TPC and a magnetised iron detector as far detectors. For the near detector, a high-pressure gas TPC embedded in a calorimeter and a magnet is the baseline design.

A mandatory milestone in view of any future long baseline experiment is a concrete prototyping effort towards the envisioned large-scale detectors, and an accompanying campaign of measurements aimed at assessing the systematic errors that will be affecting their intended physics programme. Following an encouraging feedback from 108th SPSC on the technology choices, we have defined as priority the construction and operation of a $6 \times 6 \times 6\mathrm{m}^3$ (active volume) double-phase liquid argon prototype.

The prototype is an industrial prototype of the design proposed in the EoI and scalable to 20 kton or more. It is to be constructed and operated in a controlled laboratory and surface environment with test beam access, such as the CERN North Area (NA). Its successful operation and full characterisation will be a fundamental milestone, likely opening the path to an underground deployment of larger detectors. The response of the LAr prototype will be measured and understood with an unprecedented precision in a charged particle test beam (1-20 GeV/c). The exposure will certify the assumptions and calibrate the response of the detector, and allow to develop and to benchmark sophisticated reconstruction algorithms, such as those of 3-dimensional tracking, particle ID and energy flow in liquid argon. All these steps are fundamental for validating the correctness of the physics performance described in the EoI, which so far rely essentially on simulated data, before committing to build the large-scale detector.

We anticipate that a successful operation of the double-phase $6 \times 6 \times 6\mathrm{m}^3$ LAr prototype and its campaign exposure to a charged particle beam, will provide very important and vital feedback for long baseline programmes, and in general for the field. It will represent a so-far never-achieved milestone for LAr detectors. While of the same mass scale of ICARUS, the design of the double-phase prototype presented here, specifically addresses and represents a concrete step towards an extrapolation of the technology to very large masses in the multi-kton range. The potential to extrapolate this design to very large scales has been considered and studied for several years within the EU FP7 funded LAGUNA/LAGUNA-LBNO design studies. The parameters of the prototype will be directly scalable and the components mass-produceable. Long drift paths will be assessed on a large scale.

We submit our proposal now in view of its realisation and an exposure to the charged particle beam before the LHC LS2.

Contents

1 Introduction

1.1 Main goals of the prototype

The main objectives of LBNO in the coming years are to develop demonstrators of the neutrino detector technologies considered in the Expression of Interest (EoI) submitted to the SPSC [1], needed to leverage large risks associated to the extrapolation from existing experience to the huge mass required for far detectors. The SPSC has endorsed the physics case for CP-violation and neutrino mass hierarchy determination described in the EoI, the choice of the LAr detector technology, and encourages the development of the kind of activities envisaged in this document.

The concept of the LAr Time Projection Chamber (LAr TPC) [2] and its excellent tracking-calorimeter performances allow for massive neutrino detectors with higher signal efficiency and effective background discrimination compared to other techniques. The pioneering work of ICARUS on prototypes of ever increasing mass (0.003 [3], 0.05 [4], 3 [5], and 10 tons [6]) has culminated in the construction and operation of the T600 detector (478 tons) on surface [7], its characterization [8–13], and eventually to its underground commissioning [14]. The so-called GLACIER design [15, 16], based on the double phase Large Electron Multiplier (LEM) readout "sandwich" with charge extraction and amplification, coupled to a very long drift paths in a single non-evacuated LNG-type tank has been advocated as an attractive solution to reach very large detector masses, beyond what is realistically achievable by linear extrapolation of the ICARUS design. The successful phases of R&D and prototyping on small-scale double phase LAr LEM TPC setups [17–20], benefitting from the worldwide effort on the general development of Micro Pattern Gas Detectors (MPGD) [21] – in particular GEMs [22], MicroMegas [23] and LEMs/THGEMs [24] – already demonstrated the significantly improved performance of this novel concept. The collection-only readout mode (avoiding the use of induction planes) is also an important asset in the case of complicated topologies, like e.g. in electromagnetic or hadronic showers. Three examples of cosmic events obtained with typical electric field configurations (the drift field of ≈0.4 kV/cm) and 35 kV/cm in the LEM holes are presented in Figure 1. Using a simple event display images for two projections, i.e. xt- and yt-projections, can be obtained for each event: x- and y-coordinates are two horizontal coordinates orthogonal to each other and t-coordinate corresponds to the vertical coordinate z.

The LAGUNA and LAGUNA-LBNO EU FP7 design studies have been focussed on the GLACIER concept, a large double phase Liquid Argon TPC with a long drift and charge-sensitive detectors in the gas phase. According to these studies it is technically feasible to build a large (20-100 kt) underground tank, based on the LNG industrial technology. In a more recent related development these studies have

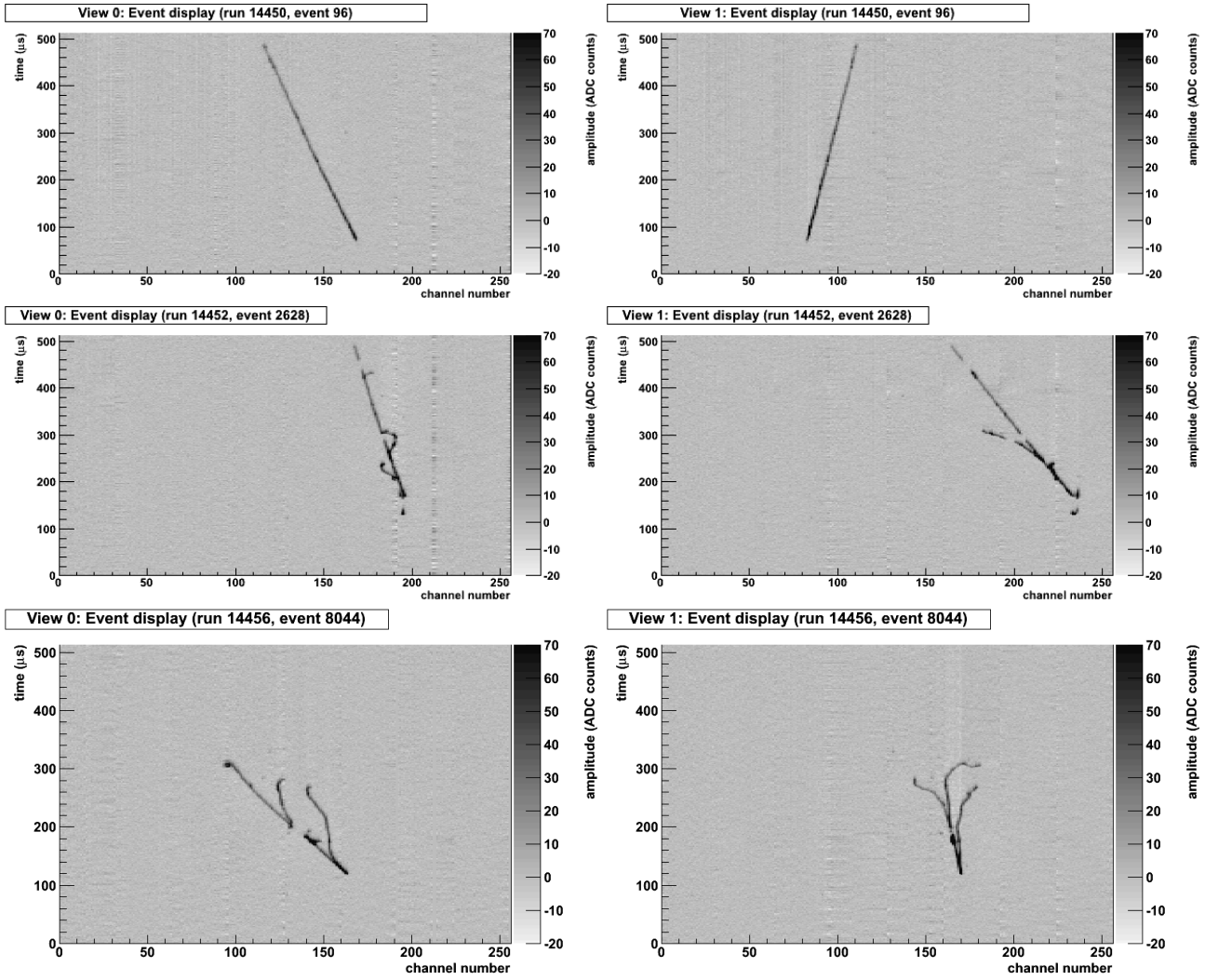

FIG. 1: Event display for three cosmic events recorded using the 40×80 cm^2 LAr LEM-TPC [18]. The left and right columns correspond to the xt- and yt-projections, respectively. Top: a straight muon track crossing from top to bottom of the field cage. The time of the start ($t_0 \sim 60$ μs) and the end ($t_{\max} \sim 490$ μs) of the extraction are clearly visible. Middle: an example of a "grazing" muon track with delta rays, where the extraction starts later at $t \sim 150$ μs. Bottom: interacting event.

also considered a novel technique for the tank construction involving the membrane technology for the tank. In this technology, the functions of structural support, insulation and liquid containment are all realised by different components, namely an outer concrete structure, specially designed insulating panels and a thin layer of steel plates. These development are very promising for the realisation of a large underground detector, however several areas need to be verified on a large scale prototype.

In order to measure and assess the detector performance for LBNO, we consider dedicated test beam campaigns, to test and optimise the readout methods and the calorimetric performance of such detectors. The proposed test beam will address the following points:

1. Electron, neutral pion, charged pion, muon reconstruction: A crucial feature of the LAr TPC is

the possibility for a very fine sampling, which should deliver unmatched performances in particle identification and reconstruction.

2. Electron/π^0 separation: Another central feature of the LAr TPC is the possibility to precisely measure and identify electrons from neutral pion backgrounds.

3. Calorimetry: A specific feature of the LAr TPC is its 100% homogeneity and full sampling capabilities. As an extension of the measurements performed in above, more refined measurements with low energy particles will yield actual calorimetric performance and determine the ability to reconstruct full neutrino events in the GeV-range.

4. Hadronic secondary interactions: With the large statistics expected, an exclusive final state study of pion secondary interactions will be attempted. Comparison of the data obtained with MC (e.g. GEANT4) will allow to cross-check and eventually tune these models.

The reconstruction of electrons, neutral and charged pions and muons will be demonstrated in the dedicated test beam campaign. The obtained results will optimise the readout parameters to be used in the far detector of LBNO. They will represent a major milestone in the definition of LAGUNA/LBNO which involves low energy neutrino beams or sensitive searches for proton decay, and will complement direct measurements in a low energy neutrino beam. The LAr TPC reconstruction software with a fully automatised reconstruction will be developed. Samples of hadronic interactions produced by particles of well-known momentum will allow benchmarking these software tools and determining their performance with high precision.

FIG. 2: Areal view of the foreseen extension of the CERN EHN1 (Bat 887) building to host the LAGUNA/LBNO detector prototype (September 2012).

1.2 Location of the prototype and needed infrastructure

The cryogenic vessel required for a detector of the size of $6 \times 6 \times 6\text{m}^3$ is hardy transportable, and is most conveniently constructed *in situ*. On the other hand, the detector components will be assembled and tested offsite, transported sealed onsite, and installed inside the vessel, equipped during the installation phase as a clean-room.

An extension of the CERN EHN1 experimental hall (See Figure 2) would provide an appropriate location to host the $6 \times 6 \times 6\text{m}^3$ prototype. This extension fulfils the following requirements:

- possibility to host the infrastructure needed during the construction and installation phase, such as crane, access, electricity, services, by extending the presently existing services in EHN1;
- controlled area for safe cryogenic operation;
- charge particle test beam by extension of the existing lines in EHN1.

We are not aware of official cost estimates specific to such an EHN1 extension. These should be provided by CERN, via their technical experimental area support teams. We propose to locate the detector in a recessed floor region (≥16m large, ≥16m long, ~7m deep) of the EHN1 extension, as illustrated in Figure 3. Please refer to Section 6.1 for a general list of space and infrastructure requirements.

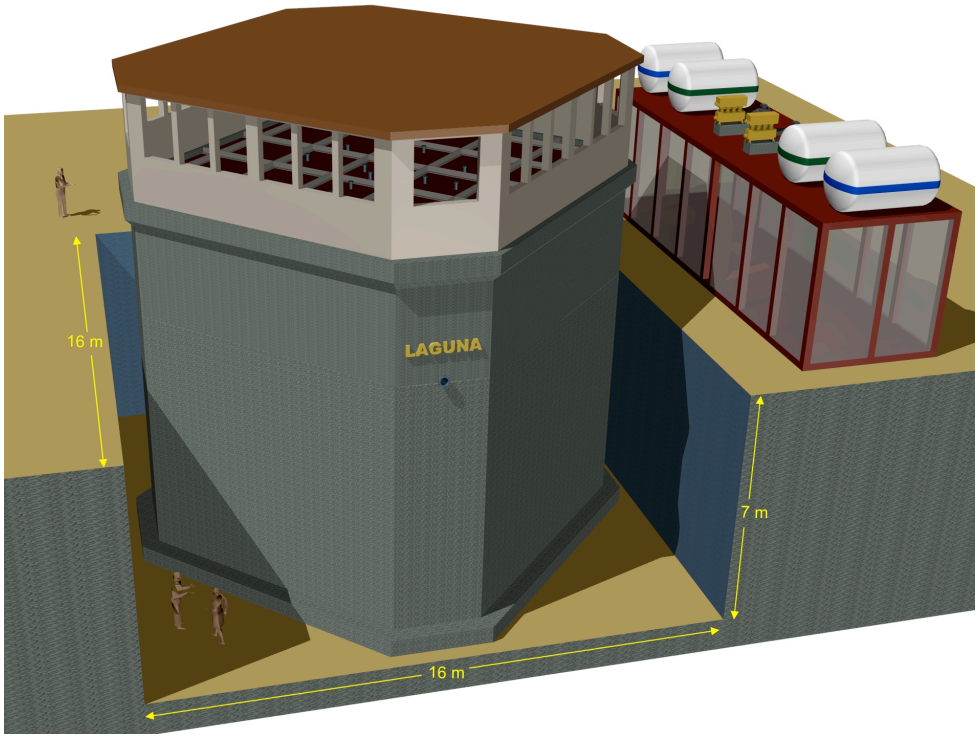

FIG. 3: Illustration of the prototype in the trench.

2 Scientific and technical motivations

2.1 Calorimetry in charge particle beams

Besides its tracking capabilities, the LAr TPC can also be considered as a fully homogeneous liquid argon ionization chambers, allowing the energy measurement by total absorption, in the spirit of the liquid argon calorimeter proposed by Willis and Radeka [25]. As was pointed out in their pioneering work, liquid argon is a medium that satisfies all requirements better than many other materials. All the energy is ideally converted into ionization through the development of the cascade showers, which is then drifted across a gap and readout electronically. The integral charge, once calibrated, yields the incoming particle energy. In practice, the precision of the ionization measurement is limited by (i) particle leakage out of the surface of the detector, (ii) energy carried off by neutrinos, (iii) nuclear interactions releasing or absorbing binding energies, (iv) charge recombination (v) charge quenching of heavy nuclear fragments, alpha particles and nuclear evaporation products (saturation of response on densely ionizing particles) and (vi) electronic noise. The energy resolution of the calorimeter will be determined by the fluctuations in the above effects.

Just as in the case of the liquid argon ionization chamber, the LAr TPC is a single-carrier device as far as charge collection is concerned, since only the drifting electrons induce visible signals as they arrive nearby the readout electrodes in the LAr TPC, which is picked up by a charge sensing preamplifier, and then sampled and converted to digital information. Offline the integrals of the digitized signal waveforms yield the full amount of charge of the ionization electrons. This situation is similar to that of calorimeters where positive ions, due to their very low mobility, contribute little to the signal charge in the short time electrons take to drift across the gap (which for uniformly distributed ionization across the gap yields half the charge).

In order to study the calorimetric response of the LAr TPC, Monte Carlo simulations with the GEANT3/GFLUKA and GEANT4 (QGSP_BERT physics list) were performed in the full geometry of the LAr detector. Charge recombination R was taken into account according to the Birks law:

$$R = \frac{A}{1 + k/E_{drift}\,(dE/dx)} \tag{2.1}$$

where $A = 0.8$, $k = 0.0486$ kV/cm$\frac{\mathrm{g/cm^2}}{\mathrm{MeV}}$ and E_{drift} is the drift field [11]. For 1 kV/cm, about 30% of the produced ionization charge recombines in the case of minimum ionizing particles. The digitization of the charge is performed using the expected response of the charge preamplifier. The charge is reconstructed using the same automatic reconstruction algorithm as used for data.

The electromagnetic and hadronic responses were studied with 1, 3, 5, 7 and 10 GeV/c electrons and charged pions. Since pure liquid argon is a non-compensating medium, electromagnetic and hadronic showers require different calibrations. The e/π compensation is performed offline and the reconstructed energy is therefore defined as

$$E_{reco} = \alpha E_{had} + \beta E_{em} \tag{2.2}$$

where E_{had} is the reconstructed hadronic component, E_{em} is the reconstruction electromagnetic component and α, β are tunable parameters. Neglecting the electromagnetic components from the charged pions, the parameters α and β are measured from the hadronic and electromagnetic energy response. The results are shown for the case of GEANT3 and GEANT4 in Figure 4 on the left. Both simulations

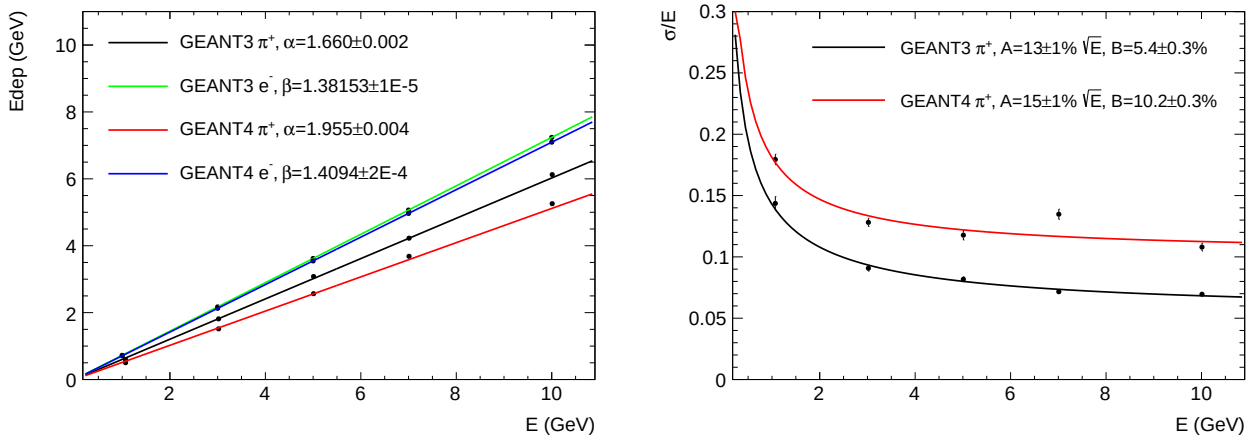

FIG. 4: LAr energy response of MC generated (GEANT3/GEANT4) e^- and π^+ events for energies up to 10 GeV. The left plot shows the obtained results for the correction factors α and β. On the right the reconstructed energy resolution for π^+ particles is shown.

are in agreement for the electron showers, with a consistent value for $\beta \simeq 1.4$, as expected from the charge recombination effect. On the other hand, the results differ for hadronic showers, with GEANT4 predicting about 30% less ionization than GEANT3. This difference is also reflected in the predicted hadronic energy resolutions. The right plot shows the energy dependence of the hadronic shower resolution, superimposed with the fit $\sigma/E = A/E \oplus B$. The stochastic terms are similar at the level of 15%, while the predicted constant term is significantly larger with GEANT4 which predicts 10% than with GEANT3/GFLUKA which gives 5%. The study of calorimetry will be performed with the LAGUNA/LBNO prototype with unprecedented statistics of charged particles crossing the detector of well-defined energy and direction. The understanding of calorimetry is a fundamental milestone to achieve the required level of precision in the reconstruction of the neutrino energy, fundamental in the future oscillation searches at long baselines.

As specified above, the calorimetric resolution of the chamber is limited by particle leakage out of the surface of the detector. The best energy resolution is obtained if the resulting cascade shower is fully contained within the fiducial volume of the detector. The containment of the showers in the $6 \times 6 \times 6\text{m}^3$ were studied by comparing the reconstructed energy[131] of π^+ events with two other simulated detector geometries: (i) LBNO/GLACIER 20kton, which is the far detector described in the LBNO expression of interest [1]. Here the event is generated at the center of the detector and the volume is large enough that the event is fully contained (ii) $3 \times 1 \times 1\text{m}^3$ which is a chamber of 3 m along the beam direction 1m transverse and 1 m drift.

Figure 5 shows an event display of a shower initiated by a 3 GeV π^+ in each of those detectors. For a detailed discussion on the simulation of detector geometries and particle transport please refer to Section 5.3. The distributions of reconstructed energies were compared for generated π^+ of 0.2, 0.5, 1, 3, 5 and 10 GeV in the three detector geometries. The distributions of reconstructed energies are shown in Figure 6 for pions of 1 and 10 GeV. If the event is fully contained, as is the case with the LBNO/GLACIER 20kton geometry, the distribution of reconstructed energy is centered on the initial energy of the particle. On the other hand if the fiducial volume is not large enough (e.g in the $3 \times 1 \times 1\text{m}^3$), the distribution is shifted to lower energies. The mean of the distribution of reconstructed energy versus the initial energy of the pion is plotted in Figure 7. It shows that the $6 \times 6 \times 6\text{m}^3$ detector is large enough to contain pion showers even/at least up to 10 GeV, and is adequate for energies up to 20 GeV as envisioned. On the other hand, the smaller $3 \times 1 \times 1\text{m}^3$ is not adequate to contain hadronic showers.

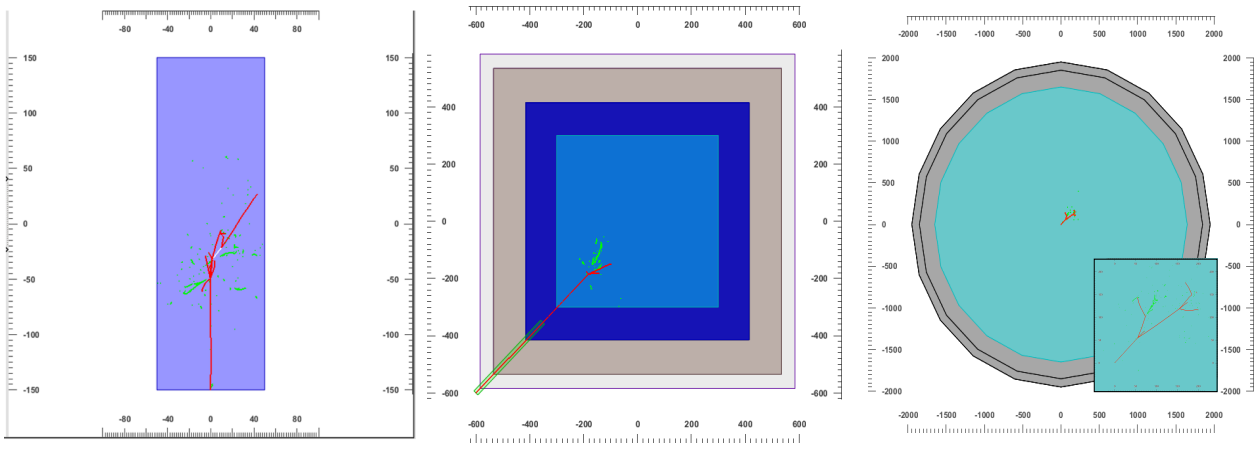

FIG. 5: Topview of a simulated 3 GeV π^+ in the $3{\times}1{\times}1\text{m}^3$ (left), the $6{\times}6{\times}6\text{m}^3$ (middle) and the LBNO/GLACIER 20kt with a zoom on the shower (right).

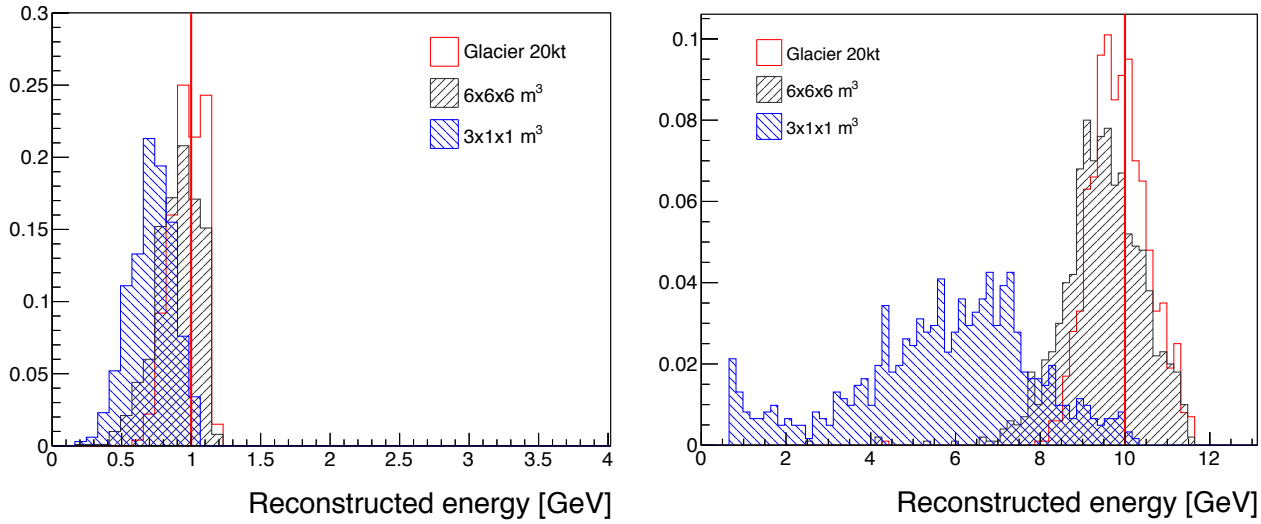

FIG. 6: Distribution of reconstructed energy for a π^+ event of 1 GeV/c (left) and 10 GeV/c (right) for three different detector geometries. The initial energy of the particle is indicated by a red line.

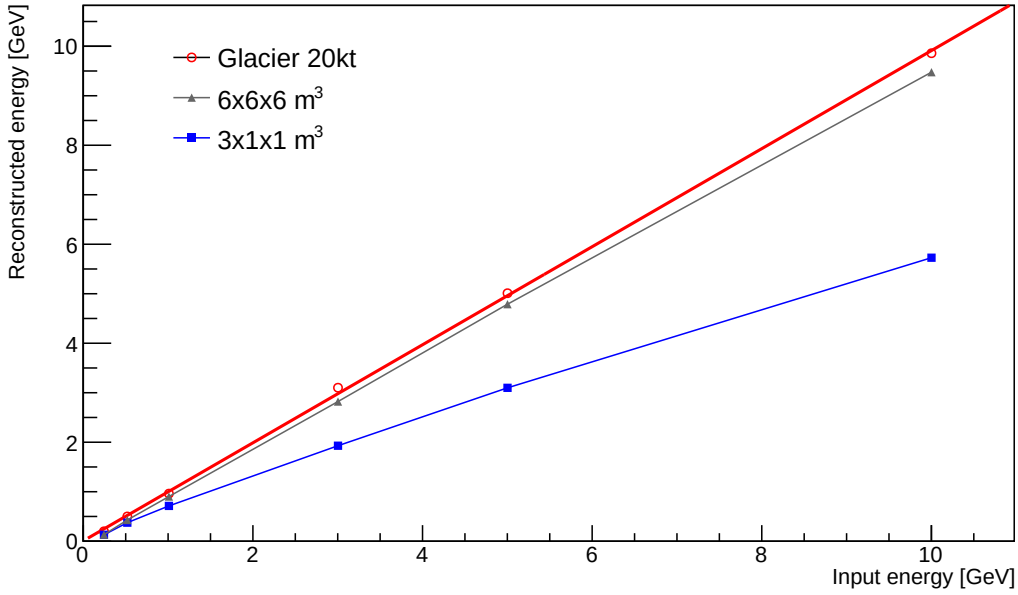

FIG. 7: Mean of the reconstructed energy as a function of the π^+ initial energy for the three considered geometries.

2.2 Development and proof-check of industrial solutions

The technical goals are to develop and assess the design in view of an extrapolation to a multi-kton mass scale and a long-term stable operation (>10 years), as necessary to accomplish the LBNO physics programme [1]. One fundamental issue is the drift length, whose optimisation involves the interplay of several technical components, such as the high-voltage (for the drift field), the purity, the mechanical aspects of the field cage, etc. It can only be addressed with a prototype with a drift length of several

meters. To test the feasibility and the performance of an ultimate drift length of 20 m [15], a minimum length of 6 m is required, where the longer drift conditions expected at a drift field of 1 kV/cm can be reproduced by the shorter drift length of 6 m at a field of about 0.3 kV/cm. From the technological point of view the most urgent questions to be addressed are summarised in the following:

- **Very high purity**. The drift of ionization electrons over a distance of 20 m requires a very clean environment, with impurities at the level of 100 ppt O_2 equivalent for an electron lifetime of 3-10 ms. While this has been achieved on small prototypes, this will be the first test with a large scale non-evacuable prototype and the same tank construction technique foreseen for the far detector.

- **Large field cage.** This is a large structure with demanding requirements on its mechanical precision and capable of sustaining a large potential difference (up to 500 kV).

- **Very high voltage generation.** A very low noise and stable power supply able to reach 600 kV to generate an uniform drift field of 1 kV/cm (300 kV power supplies with the required specification are commercially available).

- **Large area micropattern charge readout.** A large 36 m^2 surface will be instrumented with a charge sensitive device providing gas amplification in ultra pure argon vapour.

- **Cold front-end charge read-out electronics.** A good S/N is crucial to reach the required physics performances, especially for the low energy neutrino physics. An innovative solution with preamplifiers located as close as possible to the charge-sensitive anode, but yet accessible without opening the inner vessel, will be tested.

- **Long term WLS coating.** A method based on WLS deposition with very long stability (> 10 years) will be implemented and tested.

- **Integrated light readout electronics.** New integrated devices will be developed for the digitisation of argon scintillation light, scalable to very large detectors.

3 Detector overview

3.1 Design concept of the $6 \times 6 \times 6\mathrm{m}^3$ prototype

The $6 \times 6 \times 6\mathrm{m}^3$ prototype is illustrated in Figure 8. Following the GLACIER concept, the LAr detector has the shape of a vertically standing volume, where electrons are drifted vertically towards the liquid-vapor interface, extracted from the liquid into the gas phase, amplified and collected at a

segmented anode [17–19]. The main parameters are summarised in Table I. The horizontal and vertical sections are shown in Figures 9 and 10.

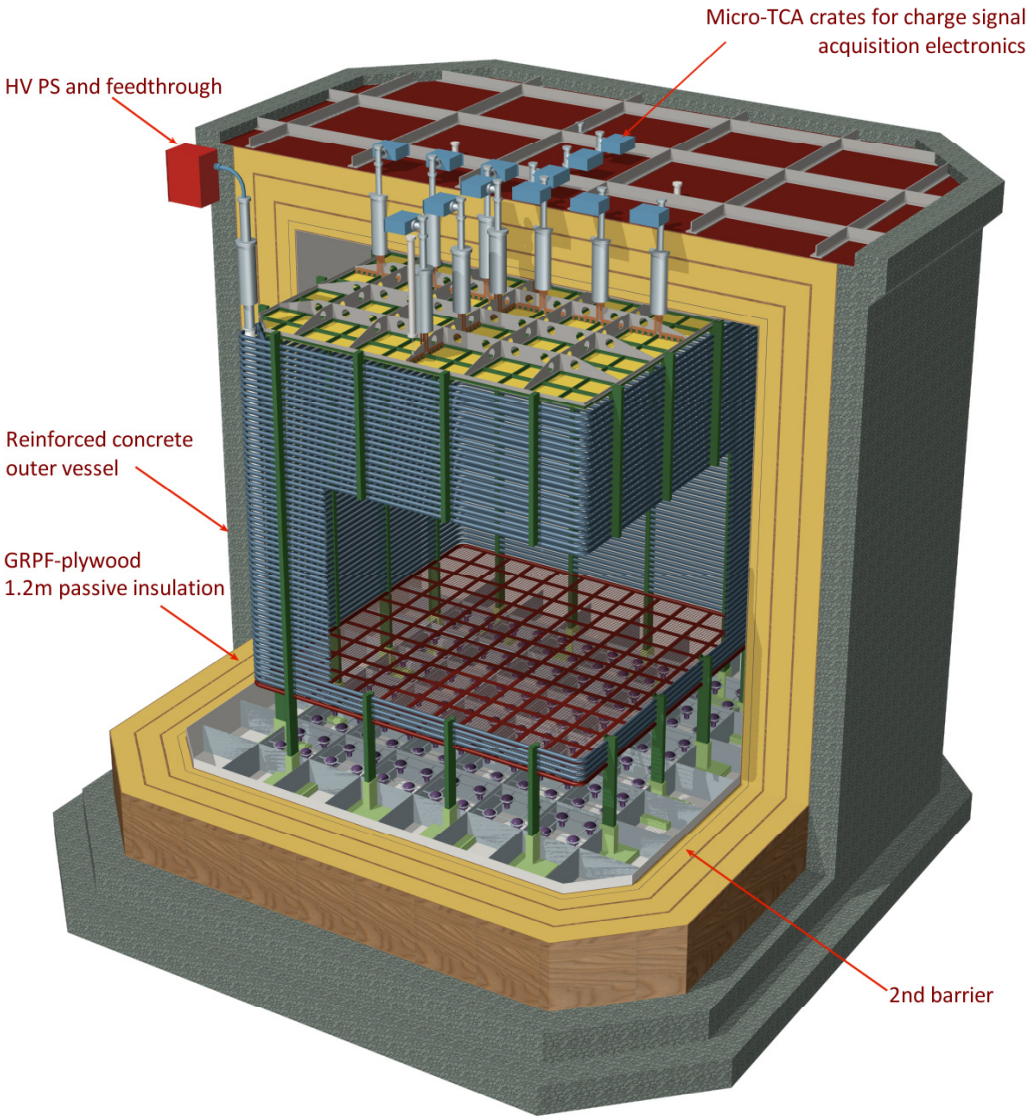

FIG. 8: Illustration of the $6 \times 6 \times 6 m^3$ with the inner detector inside the cryostat.

The uniform drift field is created by a field cage composed of several equally-spaced stainless-steel tubes, supported by insulating mechanical structures which are sitting on the bottom of the vessel with a spacing adapted to the membrane corrugation. The anode deck is suspended with stainless-steel ropes linked to the top roof. The bottom field is closed by a transparent cathode and the top field by an anode, which also serves as the charge readout. The light readout consists of PMTs uniformly distributed below the cathode.

The detector is configured as a $6 \times 6 \times 6$ m^3 liquid argon TPC with liquid-to-gas ionisation electron extraction and multiplication before collection. The ionisation charge is collected in a 2-dimensional

Liquid argon density	T/m^3	1.38
Liquid argon volume height	m	7.6
Active liquid argon height	m	5.99
Hydrostatic pressure at the bottom	bar	1.03
Inner vessel size (WxLxH)	m^3	8.3 × 8.3 × 8.1
Inner vessel base surface	m^2	67.6
Total liquid argon volume	m^3	509.6
Total liquid argon mass	t	705
Active LAr area	m^2	36
Charge readout module (0.5 x0.5 m^2)		144
N of signal feedthrough		12
N of readout channels		7680
N of PMT		144

TABLE I: Main parameters of the LBNO prototype.

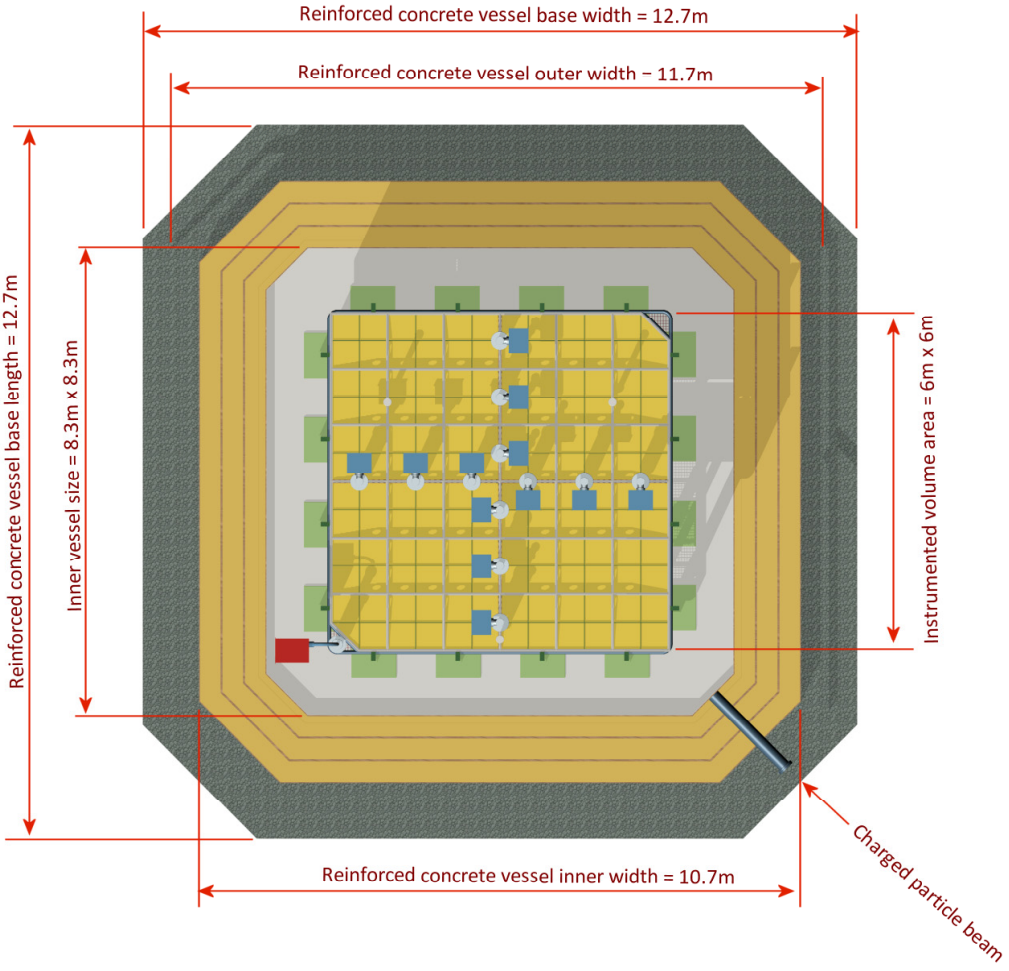

FIG. 9: Horizontal cross section.

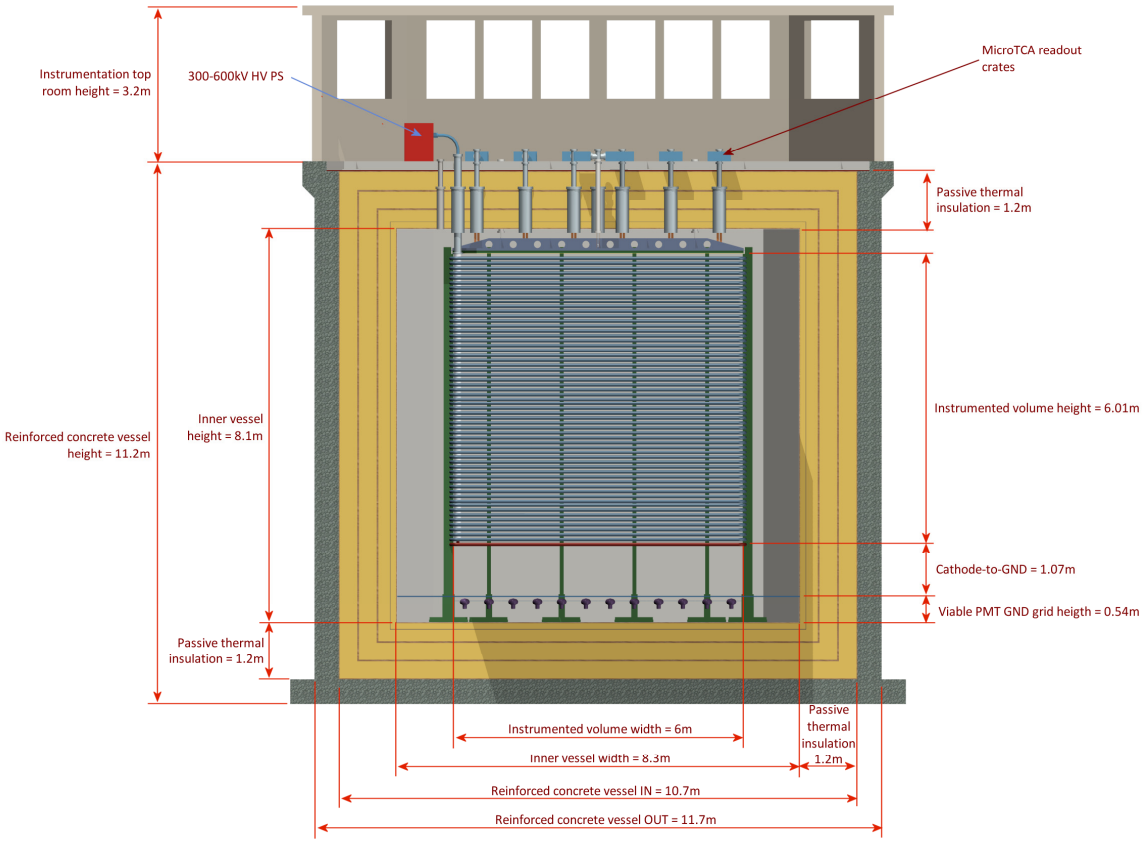

FIG. 10: Vertical cross section.

readout plane on the top of the volume with an area of 6×6 m^2 and finely segmented with a 3 mm strip pitch. The full active volume of ~216 m^3 is under an uniform electric field $E \simeq 0.5 - 1.0$ kV/cm generated from a bottom cathode plane (also 6×6 m^2) operated at ≃300-600 kV and kept uniform by a stack of field shaping electrodes (round pipes along a square path, with rounded corners) polarised at linearly decreasing voltage from the cathode voltage to ground.

The cathode plane is gridded and transparent to light to allow the detection of the scintillation light by an array of photomultipliers located at a distance of ~1m under it. Ionization charge signals are sent to a set of signal feedthroughs (12), located on the top face of the hosting LAr vessel and hosting the cold readout electronics. Other chimneys/feedthroughs are foreseen for HV (1 or 2), top readout plane suspension and level regulation (3), PMT high voltage and signal readout (4), monitoring instrumentation (level, temperature, 1 or 2). The front-end electronics is based on analog preamplifiers implemented in CMOS ASIC circuits for high integration and large scale affordable production. The baseline design is to integrate this electronics on the feed-through flange terminating the chimneys on the roof of the tank, under the insulation layer in order to be cooled to a temperature near that of liquid argon. Cathode and field shaping electrodes are kept in their position by a set of insulating

supports/spacers resting on the inner vessel floor. The inner vessel has a cubic shape with chamfered vertical edges. Its walls are built with the so-called corrugate membrane technique, to compensate thermal shrinkage. A manhole and a detail-introduction hole are located in its top face. Thermal insulation is passive, based on GRPF (glass reinforced polyurethane foam) layers, interspersed with pressure distributing layers of plywood. Its thickness and composition are such to reach a residual heat input of 5 W/m^2. The estimated total heat input including also the losses through the feed-throughs, cables, etc., and introduced by the LAr process, is ~4 kW at liquid argon temperature, to be dissipated by cryocooler(s). The passive insulation is contained in a reinforced concrete "vessel" with $\simeq$ 0.5 m thick walls. The top outer ceiling is made by a framework reinforced stainless steel plane, able to support the inner anode and outer instrumentation (electronics, cryogenics, control).

A charged beam pipe (evacuated) is indicated as crossing the concrete outer vessel and the thermal insulation layers. Its vertical orientation is adapted to the charged beam vertical axis in its last section.

3.2 Liquid argon as detector medium and electron drift

Liquid argon, and liquid noble gases in general, have interesting properties for detecting particles, what makes them a good choice as target material. A summary of the most important argon properties is given in Table II. Because of its density of 1.4 g/cm^3, liquid argon is a good stopping material with an average energy loss dE/dx of 2.12 MeV/cm for a minimum ionizing particle (mip). Also, an interaction of a particle with an argon atom excites it and creates scintillation light, or the atom is ionized. The mean excitation energy of W_γ = 19.5 eV, and the mean ionization energy W_{ion} = 23.6 eV, give a very good energy resolution also for detecting low energetic particles. The possibility to drift charges within the liquid noble gas along the electric drift field, without big diffusion, gives the option to read out ionising tracks with a high spacial resolution. The basic principle of every time projection chamber is that free charge carriers are produced in a relatively large volume and then drifted towards an electrode. The time needed between the initial ionisation and the moment the signal is read out from the electrode defines, together with the drift velocity, the distance between the interaction and the electrode along the lines of the electric field. In case of the double phase LAr TPC, the drift velocity in gas argon as also in liquid argon have to be taken in account.

Argon is a byproduct from the air liquefaction process and therefore relatively cheap compared to other noble gases. This makes it the only viable candidate for very large detectors of several kilotons of active volume.

General properties	
Atomic number	18
Molecular weight	39.948 g/mol
Most important stable isotopes	^{36}Ar (0.34%) ^{38}Ar (0.06%) ^{40}Ar (99.60%)
Concentration in air	0.934%
Melting point (1 atm)	83.8 K
Boiling point (1 atm)	87.3 K
Triple point	83.8 K and 0.687 bar
Ratio LAr/GAr (1 atm)	835 vol/vol
Gaseous phase properties	
Gas density (at boiling point resp. 15 °C)	5.85 resp. 1.67 kg/m^3
Heat capacity at constant pressure C_p (1 bar and 25 C°)	0.02 kJ/mol · K
Heat capacity at constant volume C_v(1 bar and 25 C°)	0.012 kJ/mol · K
Thermal conductivity of GAr (1 atm and 273 K)	16.36 mW/m · K
Thermal conductivity of GAr (boiling point and 1 atm)*	5.66 mW/m · K
Ionization energy in gas W_{ion}	26.4 eV
Liquid phase properties	
Liquid density (at 87.3 K)	1392.8 kg/m^3
Latent heat of vaporization L_v (1 atm)	160.81 kJ/kg
Thermal conductivity of LAr (87.3 K)*	127 mW/m · K
dE/dx_{min} for mip	2.12 MeV/cm
Ionization energy in liquid W_{ion}	23.6 eV
Excitation energy W_γ	19.5 eV
Maximum of emission spectrum	~ 128 nm
Radiation length X_0	14 cm
Molière radius	9.28 cm
Nuclear interaction length	84 cm
Maximal breakdown strength	1.1 – 1.4 MV/cm

* Value linear extrapolated from [26]

TABLE II: Physical and chemical properties of argon.

3.3 Drift velocity and diffusion in argon gas

Applying an electric field, the electron is drifted along the field line and the total energy depends on the electric field strength as shown in Figure 11. The Figure is normalized to a reduced electric field E/N with Townsend unit (Td=[E/N] = 10^{-17} V cm^2), where E is the electric field and N the molecular density. The top label indicates the values for SATP conditions (Standard Ambient Temperature and Pressure: 20 °C and 1 bar).

For electrons drifting in gas, the energy gained between two collisions is, because of their small mass, rather large. The drift velocity hence depends strongly on the total scattering cross-section between the electrons and the atoms of the medium, as shown in Figure 12. It is not uniform but has a minimum

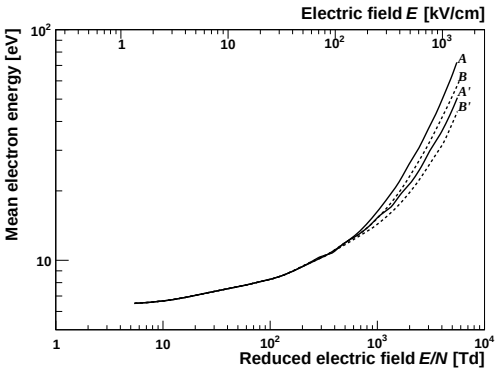

FIG. 11: The mean energy in argon gas as a function of the external (reduced) electric field. In case A, both the elastic and inelastic scatterings are according to the elastic differential cross-section. In case B the inelastic scattering is isotropic. A and B are the values before and A' and B' after scattering [28]. The scale of the electric field E is given for 1 bar and 20 °C.

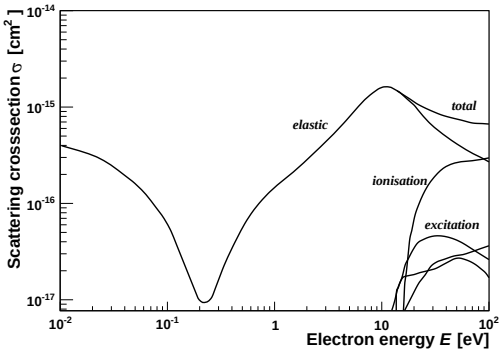

FIG. 12: The cross-section between electrons and argon gas as a function of the total energy of the electron, calculated with Magboltz [29]. Clearly visible is the Ramsauer-minimum around 0.2 eV.

around ~ 0.2 eV caused from quantum mechanical effects (Ramsauer-minimum [27]). In the energy range relevant for the drifting electrons, there is mainly elastic scattering. In a first approximation the drift velocity u is given by the acceleration in the electric field E and the characteristic time τ_c between two collisions

$$u = \frac{e\,E\,\tau_c}{m} \equiv \mu E \tag{3.1}$$

where μ is the mobility. The characteristic time τ_c is a function of the electric field E [30]. This is only an approximation since it is assumed that the electron completely stops after each interaction. An actual measurement of the drift velocity is reported in [31] and shown in Figure 13.

An important property is the electron cloud diffusion. In case of an electric field, we have to distinguish between the diffusion in drift direction and the diffusion normal to it. The longitudinal and transversal diffusions are given by

$$\sigma_{l,t}^2 = 2D_{l,t}\,t = 2D_{l,t}\,L/u \tag{3.2}$$

where L is the drift length, u the drift velocity along the electric field lines and $D_{l,t}$ the diffusion coefficients in longitudinal and the transversal directions, respectively. As shown in Figure 14, the diffusion coefficients are depending on the electric field. Also it is shown that for low electric fields the diffusion in the transversal direction is almost one order of magnitude bigger than the one in longitudinal direction.

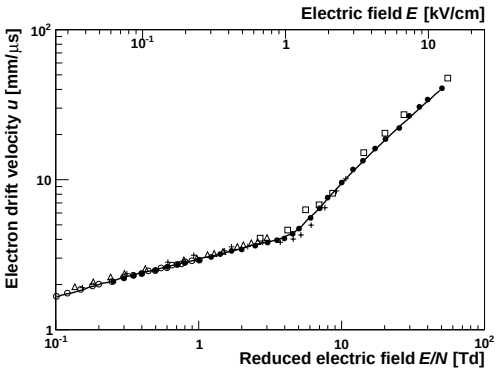

FIG. 13: The electron drift velocity u in gaseous argon as a function of the normalized electric field ([Td] = 10^{-17}Vcm^2) according to [31]. The scale for the electric field E is derived for SATP conditions.

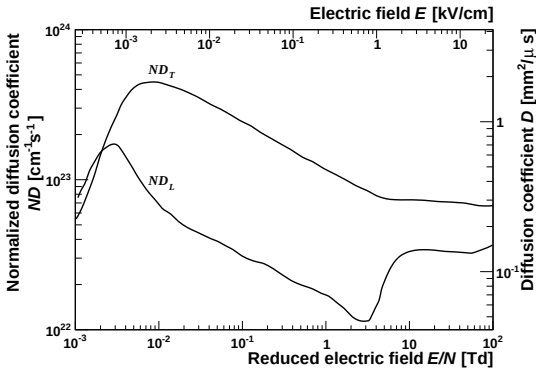

FIG. 14: The normalized longitudinal and transversal diffusion coefficient ND for gaseous argon according to [32]. The scale of the diffusion coefficient D and the electric field E are under SATP conditions.

3.4 Drift velocity and diffusion in liquid argon

The liquid phase changes the properties for drifting electrons. Electrons drift through a non-polar medium and locally, the argon atoms are polarised by the charge. The local field is no longer only given by the distance between the electron and the scattering atom but also by the sum of all other fields due to the induced dipoles in the neighbouring atoms. This interaction changes the scattering cross-section and the Ramsauer-minimum disappears [33]. Other parameters besides the electric field affect the drift velocity. A relatively large effect is due to the temperature of the liquid argon. In [34] an average temperature gradient of u has been reported to be

$$\frac{\Delta u}{\Delta T \cdot u} = (-1.72 \pm 0.08)\ \% \cdot \mathrm{K}^{-1} \tag{3.3}$$

Experimentally, the drift velocity of electrons in liquid argon is measured by their drift time in a known electric field. One possibility for the measurement is to use crossing muons through the detector. There is a trigger on the primary scintillation light and the stopping trigger is either on secondary scintillation light or on the charge extracted and read out by an anode [35]. Another option is to knock out the electrons from the HV cathode by the use of a laser [34] or a pulsed xenon lamp [36]. The trigger is the pulse from the cathode when an electron is knocked out, and, as a stopping signal, again the arrival of the charge on the anode is used. Figure 15 shows the drift velocity as a function of the electric field, compiled from the literature [34, 36–40]. The data from the different sources are corrected to a common temperature of 87 K and fitted with a polynomial function[132], as proposed by [36].

The electron cloud diffusion in the liquid is an important parameter to determine the maximum drift

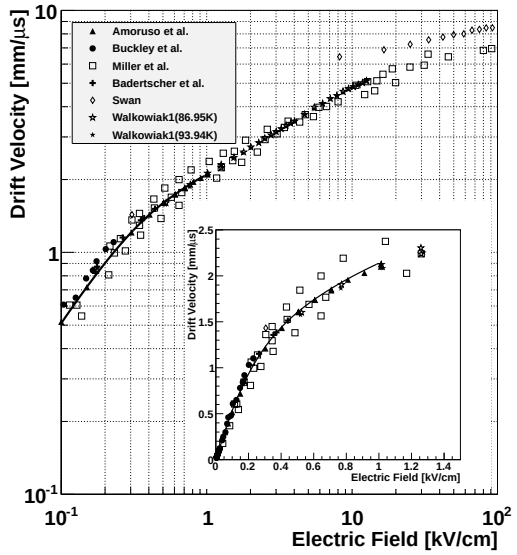

FIG. 15: Drift velocity in liquid argon for fields up to 100 kV/cm. The general plot (data collected from [34, 36–40]) is in log-scale to give a good overview, while the zoom-in, in the interesting region of the electric field for ArDM, is in linear scale. The solid line is a 5^{th} order polynomial proposed by [36]. It is fitted between 0 and 2 kV/cm and includes all the presented data. All data are corrected according to Equation (3.3) to a common temperature of 87 K.

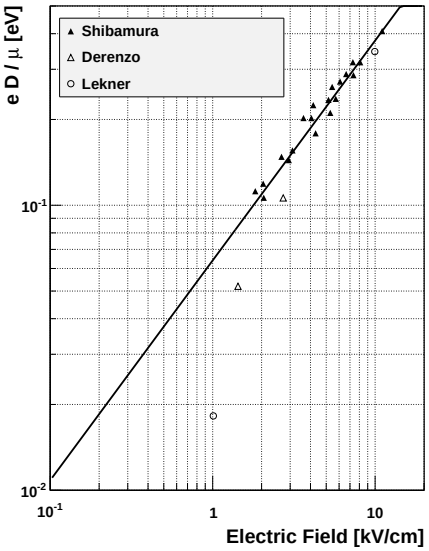

FIG. 16: Field dependence of the ratio $\frac{eD}{\mu}$ in liquid argon [41], where D is the diffusion coefficient and μ the electron mobility. The different sets of data are described in [41].

length of a detector, which is presently not fully known experimentally. The theoretical background for diffusion is similar to the diffusion in gas. It is derived from Einstein's theory about the molecular kinetic motion of particles suspended in a fluid [42]. Electrons in the liquid and with an electric field below ~ 200 V/cm can be assumed to be thermal electrons, and the ratio between diffusion coefficient and mobility is given by:

$$\frac{eD}{\mu} = kT = \frac{2}{3} < \epsilon > \tag{3.4}$$

where D is the diffusion coefficient. Figure 16 shows the ratio $\frac{eD}{\mu}$ as a function of the electric field measured by [41]. The transversal diffusion σ_t can be derived by multiplication of the coefficient with the electron mobility μ and dividing it by the drift velocity u (Equation (3.2)). The expected diffusion is shown as a function of the drift distance in Figure 17, assuming different electric drift fields ranging from 0.5 to 1.5 kV/cm. For the needed ratio of the diffusion coefficient and the mobility, the data presented in [41] and shown in Figure 16 are fitted with a simple power law, $eD/\mu = 0.064 \cdot E^{0.77}$ where E is the electric field in kV/cm. This might not be true for low electric fields, as shown by the

data points in Figure 16, but the proposed function is giving an upper limit of the ratio. The points measured at lower electric field(empty triangle) might be too low due to space charge effects [41]. The empty circles are theoretical values derived from Equation (3.4) with $< \epsilon >$-values calculated in [33].

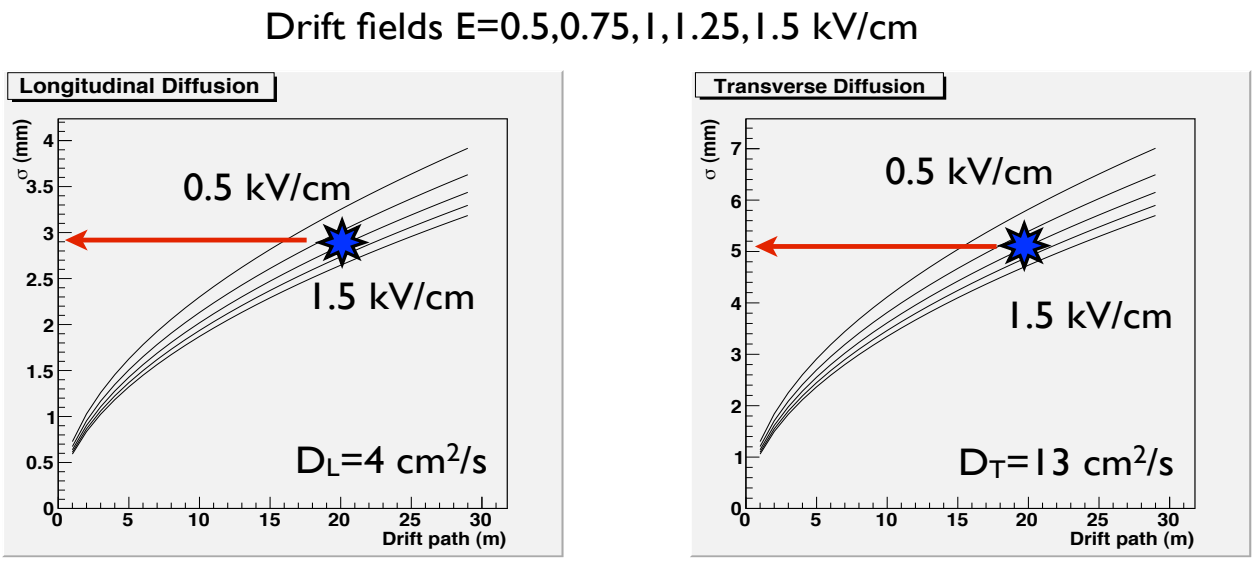

FIG. 17: Expected longitudinal and transversal diffusion in liquid argon as a function of the drift distance, for various drift fields.

From Figure 17 it is clear that even for long drifts of 10 or 20 m the diffusion is still small and a charge readout with a pitch of the readout of ~ 3 mm can be used. Electric drift fields in the range 0.5-1 kV/cm are optimal from the point of view of the resolution and are sufficient for a wide range of detectors, up to a total drift length of up to 20 m [43]).

The $6 \times 6 \times 6\text{m}^3$ will be a fundamental tool to investigate experimentally the effect of very long drift distances. To reach a goal corresponding to drift times of about 10 ms, one is considering a shorter drift distance with a reduced drift field in order to obtain similar drift times and therefore similar diffusions.

3.5 Electrons extraction

The $6 \times 6 \times 6\text{m}^3$ will be operated in double-phase conditions [17–19], involving the transfer of the electron cloud from liquid to the gas phase. The transfer of electrons in excess from a condensed non-polar fluid to its saturated vapor using an electric field is a phenomenon investigated since the seventies [44]. In particular, in argon it is experimentally shown that the electrons are extracted in two stages. Near the triple point part of the charge is emitted on time scales that can be as high as 1 ms, strongly dependent on the electric field applied [45, 46], while at larger temperatures the emission takes less than 100 ns. At high electric fields the slow extraction time reduces, and the fraction of the

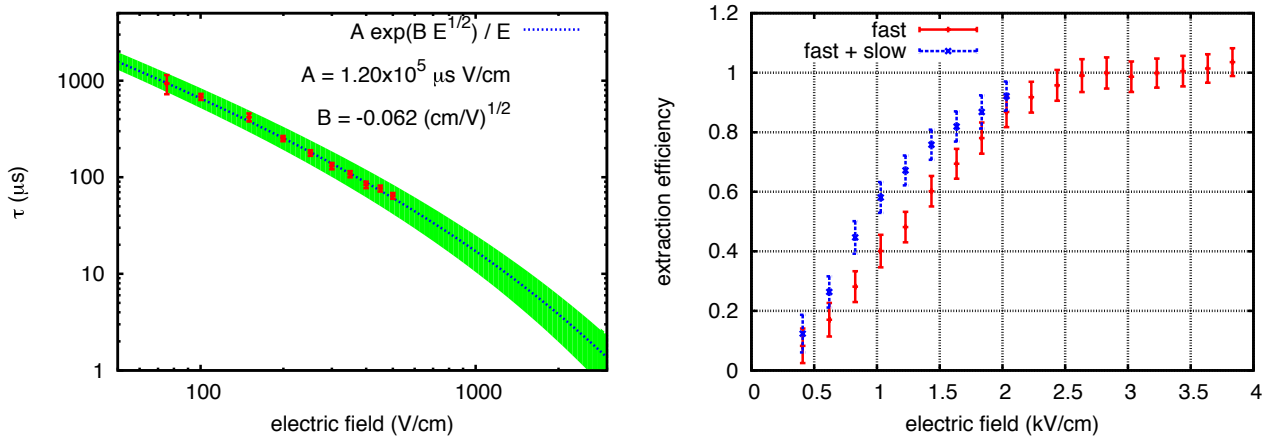

FIG. 18: The left picture shows the dependence of the extraction time on the electric field in liquid argon (T = 87.4 K) as reported in [46]. The picture on the right [45] shows the extraction efficiency for fast and slow components as a function of the electric field in liquid argon (T = 90 K). As described in the paper, due to limitations of the electronics the measurement of the slow component has a semi-qualitative character.

slowly extracted electrons becomes negligible (see Figure 18). This behavior can be understood in the framework of the Schottky model of electric field enhanced thermionic emission [47].

An electron in the vicinity of a dielectric surface feels the force of the charge induced on the surface by its presence. In analogy to a conductor surface one can compute, with a method similar to the mirror charge method [48], the potential energy of the electron. In the presence of an external electric field orthogonal to the liquid-vapor interface of argon, the energy potentials in the liquid (Φ_l) and in the vapor (Φ_v) as a function of the vertical position z (the surface is set at $z = 0$) are [45, 46, 49]:

$$\Phi_l = -V_0 - q_e \mathcal{E}_l z - A_l/z \text{ and } \Phi_v = -q_e \mathcal{E}_v z - A_v/z,$$

with

$$A_l = \frac{q_e^2}{16\pi\epsilon_0\epsilon_l} \frac{\epsilon_l - \epsilon_v}{\epsilon_l + \epsilon_v} \text{ and } A_v = A_l \epsilon_l/\epsilon_v,$$

where the terms inversely proportional to z are due to the presence of the dielectric, $-q_e$ is the charge of the electron, $\mathcal{E}_l$ and $\mathcal{E}_v = \mathcal{E}_l\epsilon_l/\epsilon_v$ are the electric fields in the liquid and in the vapor respectively, ϵ_l and ϵ_v are the dielectric constants of the liquid and of the vapor respectively, ϵ_0 is the permittivity of the vacuum, $-V_0$ is the minimum of the conduction band in the liquid with respect to the vapor (about −0.2 eV [49]). The discontinuity of the potential on the surface is unphysical, but also not relevant for the discussion. The regulated potential around $z = 0$ is shown in the plot on the left in Figure 19 for different externally applied electric fields.

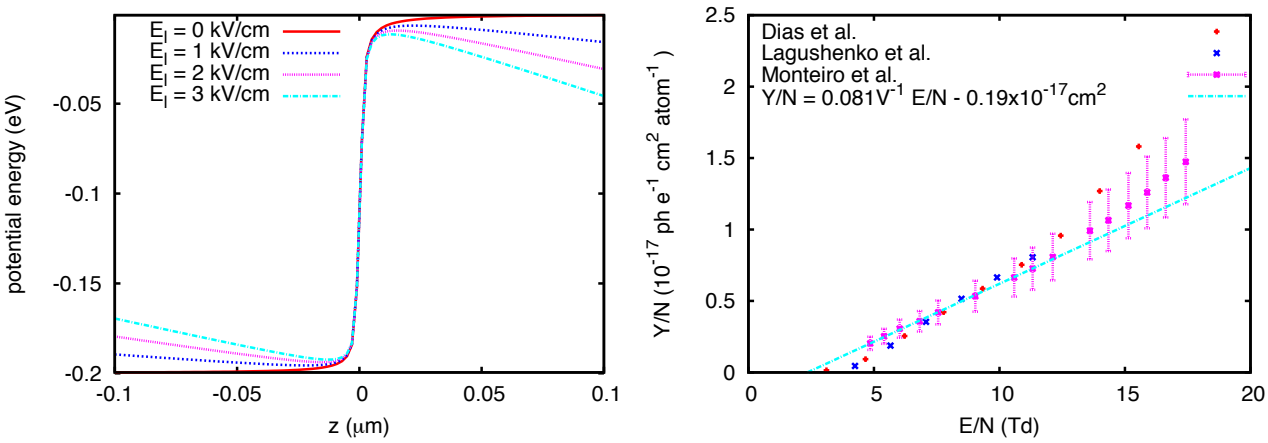

FIG. 19: Left: potential energy of an electron at the liquid vapor interface (at $z = 0$). Right: reduced proportional scintillation yield in pure argon gas simulated by Lagushenko and Dias [50, 51] and measured by Monteiro and collaborators [52].

The minimum and the maximum of the potential in the liquid and in the vapor phase are:

$$\Phi_l^{min} = 2\sqrt{A_l q\mathcal{E}_l} - V_0, \qquad \text{for } z_l^{min} = -\sqrt{A_l/(q\mathcal{E}_l)},$$
$$\Phi_v^{max} = -2\sqrt{A_v q\mathcal{E}_v}, \qquad \text{for } z_v^{max} = \sqrt{A_v/(q\mathcal{E}_v)}.$$

It is interesting to notice that the presence of the electric field reduces the potential barrier by:

$$\Delta\Phi = 2(1 + \epsilon_l/\epsilon_v)\sqrt{A_l q_e \mathcal{E}_l},$$

so that the gap becomes $V = V_0 - \Delta\Phi$.

An electron with momentum p_z perpendicular to the liquid argon surface for which $p_z^2/(2m_e) > V$ (with m_e the mass of the electron) is transferred to the vapor. The electrons with kinetic energy $T > V$, but not satisfying the requirement on p_z, are reflected towards the liquid. They undergo several elastic collisions that randomize the momentum direction almost without loss of energy, and they reach the liquid surface again. If p_z is not yet big enough, they repeat the process until all electrons are extracted in few tens of nanoseconds. These are the so called *hot* electrons (or fast component).

The electrons with $T < V$ are thermalized on the liquid surface and are emitted according to the thermionic emission with a characteristic time that depends on the energy gap [46]. These electrons are the *cold* ones (or slow component).

The electrons in liquid argon gain energy from the electric field. At around 1 kV/cm, the electron average kinetic energy is of the order of 0.1 eV [33, 53], larger than the thermal energy and comparable to the liquid-vapor interface energy gap.

The experimental facts can be summarized and explained:

1. at low temperature the electrons are emitted also slowly because their energy is not always larger than the potential barrier,

2. increasing the electric field the fraction of electrons with energy above the potential barrier increases,

3. the extraction time for the *cold* electrons decreases at high field because the energy gap reduces.

The electrons can be trapped by electronegative impurities diluted in the liquid argon and never be emitted in the vapor. Similarly to what happens to the scintillation light in the presence of impurities, the amount of charge extracted decreases by a factor $\tau_{imp}/(\tau_{ext} + \tau_{imp})$, and the effective extraction time can be written as $\tau_{ext}^{eff} = (1/\tau_{ext} + 1/\tau_{imp})^{-1}$, where τ_{ext} is the extraction time with no impurities and τ_{imp} is inversely proportional to the electronegative impurity concentration.

3.6 Proportional scintillation in gas

The proportional scintillation in argon, also referred to as secondary scintillation and luminescence, is the phenomenon of generating photons in gas or vapor in the presence of free charges and an electric field. In a defined electric field window, that depends on the density of the argon, the amount of photons is proportional to the number of electrons, to the electric field and to the length of the path covered by the electrons.

The electric field range is defined such that between two successive collisions the drifting electrons, accelerated by the electric field, gain enough energy to excite argon atoms, but not ionize them. In the case the electric field is lower, no photons are produced, in the case it is larger, because new charge is created, the amount of light grows nearly exponential with the field and the path length. For the discussion on the charge amplification in gas, see Section 3.7.

In order to take into account the argon density, the quantity used is the reduced electric field, defined as the electric field divided by the argon atomic density (1 Td = 10^{-17} V cm^2), and the reduced light yield, defined as the number of photons produced per electron per unit path length divided by the argon density. On the right of Figure 19 the simulated [50, 51] and measured [52, 54] reduced light yield at room temperature and pressure are plotted versus the reduced electric field. The measured proportional scintillation threshold and ionization threshold are respectively 2.34 Td and 12.4 Td [54], slightly lower than the simulated ones, but still in good agreement.

The electrons, when extracted from the liquid argon to the vapor, produce proportional scintillation. From the data at room temperature and pressure one can extrapolate that in an electric field

of 4.5 kV/cm, corresponding to an extraction field of 3 kV/cm in liquid, over 1 cm one electron generates about 200 photons. Since the total amount of light produced is proportional to the charge extracted, this method is used by some double phase noble gas experiments for the direct Dark Matter searches [55–57] to detect the ionisation charge. In the $6 \times 6 \times 6\text{m}^3$, they will be detected by the scintillation light system to provide a secondary trigger.

3.7 Charge amplification in gas - Townsend avalanche

In a gas an electron accelerated under the action of an electric field (E) gains energy that is released in collisions against neutral atoms. In addition to the diffusive random motion of the electron, the net drift velocity (u) in the direction of the field (but opposite) is obtained. Under the assumption that the duration of the scattering is short compared to the average time between collisions τ_c, and that the electrons undergo elastic collision only, so that the absolute magnitude of their speed does not change appreciably (the mass of the atom is much larger than the electron mass), the drift velocity can be written as in Equation (3.1) [58]. τ_m is inversely proportional to the gas density ρ and the momentum transfer cross-section σ_m [58]. In general, it depends on the energy of the electrons and therefore on E. This makes u proportional to E only for low electric fields. The kinetic energy due to the drift is much smaller than the kinetic energy due to thermal motion. A more realistic computation should take into account the details of the electron velocity distribution. The kinetic energy of the electrons increases by (1) decreasing the gas density and the electron-atom cross section and (2) increasing the electric field. In other words, the peak of the electron energy distribution moves to higher energies with the increase of the electric field, as shown in the right plot of Figure 20. It displays the results of a computation done using Magboltz 8.4 [59] in pure argon gas at 1 atm and 20° C. Magboltz calculates diffusion coefficients, drift velocities and first Townsend coefficients (see later in the text) for gas mixtures in the presence of electric and magnetic fields. The program inputs are tables of cross sections like the one reported on the left plot of Figure 20, provided in [60].

The high energy tail of the electron energy distribution extends beyond the first ionization potential, that for the argon is about 15.7 eV [61]. This means that a fraction of collisions gives rise to ionization of neutral atoms and to the production of new free electrons. This process is called Townsend avalanche and is at the base of all the signal amplification techniques in gas chambers. The larger the electric field is, the more populated becomes the tail above the ionization energy, and the larger the ionization rate is. When the electric field is high enough that the majority of the electrons have an energy above the ionization potential, the ionization rate saturates, and its behavior reflects the ionization cross section dependence on the electron energy. The first Townsend coefficient (α) is the quantity that describes

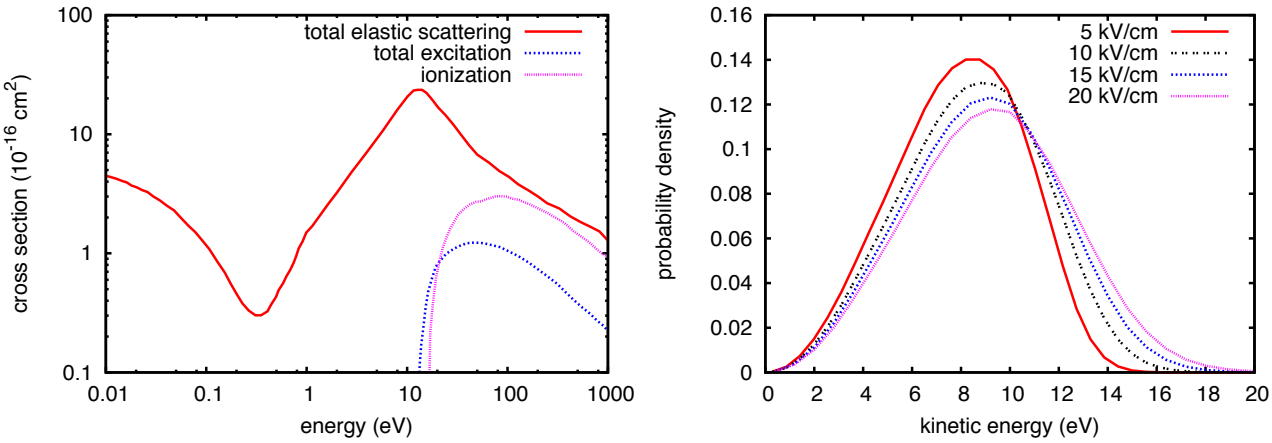

FIG. 20: Left: electron argon atom cross sections for different kind of interactions [60]. Right: energy distribution of free electrons under the action of an external electric field in pure argon gas at 1 atm and 20° C simulated with Magboltz 8.4 [59].

the number of ion-electron pairs created by an electron per unit drift length. A very useful empirical approximation of the first Townsend Coefficient as a function of the electric field and the gas density is:

$$\alpha(\rho, E) = A\rho e^{-\frac{B\rho}{E}}, \tag{3.5}$$

where A and B are constants depending on the gas. The expression α/ρ is a function of E/ρ (also called reduced electric field). The reason of this comes from the following considerations:

1. The electron mean free path (λ) can be written as $(\sigma\rho)^{-1}$, where σ is the electron-atom total cross section (generally dependent on the electron energy, see Figure 20).

2. The energy gained by a free electron between two collisions is proportional to the product of the electric field E and the mean free path λ, i.e. $E/(\sigma\rho)$.

3. $\alpha\lambda$, i.e. $\alpha/(\rho\sigma)$, can be regarded as a quantity proportional to the number of electron-ion pairs produced by an electron *per collision*.

Given a defined gas, in conditions where E and ρ are changed, but E/ρ is kept constant, the electron-atom collisions are not distinguishable, i.e. same energy and, therefore, same ionization probability per collision (proportional to α/ρ). For the very weak assumption that the mean free path of the electrons is much smaller than the size of the avalanche, the total number of electrons n_e created along a drifting

electron path $\mathcal{S}$ starting from n^0 electrons can be written as:

$$n \equiv Gn^0 = n_0 \exp\left[\int_{\mathcal{S}} \alpha(E(s))ds\right], \tag{3.6}$$

and G is the gain, under the assumption that the gas amplification device is operated in proportional mode, meaning that the detected charge is proportional to the initial charge. In a parallel plate gap of length x with a uniform electric field, where the Townsend coefficient is constant, the gain is:

$$G = e^{\alpha x}. \tag{3.7}$$

The above cited quantities must be considered as average values. In fact, the Townsend avalanche is a stochastic process with the following behavior. When $n_e < 10^5$, the number of electrons involved in an avalanche generated by a single electron follows the so called Furry distribution [62]. The probability that an electron frees a second electron traversing an infinitesimal distance dx is αdx. As computed in [63], given one initial particle entering into the uniform field of the multiplication region, the probability that n particles emerge is

$$P(n) = (1 - 1/G)^{n-1}/G.$$

The most probable number of particles at the end of the path is one, the average is $G = e^{\alpha x}$, and the variance is $G^2(1-1/G)$. For large gains the standard deviation of the distribution can be approximated with G, and for the central limit theorem, given a large number n_e^0 of electrons at the beginning of the multiplication path, the distribution of the number of emerging electrons is a Gaussian with average Gn_e^0 and standard deviation $G\sqrt{n_e^0}$. To be noticed is that the relative width of the distribution is independent of the gain, and it decreases the larger the number of electrons at the beginning is.

While the gain is mainly due to the described Townsend mechanism, also secondary effects, caused by the simultaneously produced ions and photons have to be taken into account: although the energy of the produced scintillation light is not sufficient to ionize directly argon atoms, photons can extract electrons from electrodes by photoelectric effect. A similar feedback, though much slower, is due to back drifting ions, which can eject further electrons when they impinge on the collection electrode. Obviously any of the described feedback mechanisms can turn into a continuous current, that may lead to the formation of an electron-ion plasma or a *streamer*. Due to the fact that such a streamer persists until the amplification device is completely discharged, a detector would be paralysed until the fields are back at the working point. As a consequence of the heat production, heavy discharges may

also damage the amplification device. In order to decrease the rate of discharges or to increase the maximum achievable stable gain, typical gas detectors work with a gas mixture, including a so-called quench gas that absorbs scintillation light and thus reduces the feedback. However, since the LAr TPC requires extremely low levels of contaminations of less than 1 ppb in order to drift electrons over large distances in LAr, chemical quenchers cannot be used. In the LAr LEM TPC option described in Section 4.1.2, mechanical quenching is important to stabilise the system and allow high gains to be achieved.

3.8 Electron attachement to impurities

The amount of charge collected at the anode is affected by the amount of electronegative molecules (for example O_2) dissolved in the liquid argon. By capturing free electrons these latter become negative ions which slowly drift towards the anode. Due to their larger mass and scattering cross-section with the argon atoms, they move much slower than electrons. Attached electrons therefore do not contribute to the readout signal. Thus, purity is a fundamental requirement and a possible contamination has to be kept at an extraordinary low level. This means the vessel needs to be sealed and absolutely vacuum tight, with a typical leak rate upper limit of 10^{-9} mbar l s^{-1} to prevent molecule contaminants from entering the argon volume.

In practice, the most common impurities in the welding-grade liquid argon are oxygen, nitrogen and water. In absence of leaks to the outside, the majority of the electronegative impurities come from the outgassing of the detector material itself. Special attention has to be given to composite materials like glue, for they might have chlorine or fluorine compounds. These materials must be prevented from contaminating the liquid argon, since chlorine and fluorine are the most electronegative molecules and immediately capture the drifting electrons.

In general, the attachment in liquid is a three-body process that involves the electron and the molecule to which it is attached. When attaching an electron, the molecular ion is excited and loses its energy to a third body through vibrational states [64].

$$e^- + M + X \xrightarrow{k_s} M^- + X \tag{3.8}$$

where M is the electronegative molecule and X the third body, in our case the argon atom. k_s is the rate constant and it is given as a function of the electric field E by

$$k_s(E) = \int v \cdot \sigma(v) \cdot \mathrm{f}(v, E)\, \mathrm{d}v, \tag{3.9}$$

with v the electron velocity and $\mathrm{f}(\epsilon)$ the Maxwell distribution [65]. If the capture cross section $\sigma(\epsilon)$ is a function of the energy ϵ, the rate constant is given by

$$k_s(E) = \int \sigma(\epsilon) \cdot \mathrm{f}(\epsilon, E)\, \mathrm{d}\epsilon \tag{3.10}$$

For $E = 0$ the distribution $\mathrm{f}(\epsilon)$ is

$$\mathrm{f}(\epsilon) = \frac{2}{\sqrt{\pi}\ k_B T} e^{-x} x^{1/2} \tag{3.11}$$

with $x = \epsilon/(k_B T)$. The effects of an external electric field on the rate constant k_s are described in [65] and shown in Figure 21 for different molecules. Experimentally, the rate constant k_s can be obtained by looking at the decay of the electron current after a controlled release of electrons from the cathode or inside the liquid argon by ionization.

In case of a small number of released electrons N_e with respect to the amount of impurities N_s ($[N_s] = mol/l$), the number of electrons captured per time interval is

$$\frac{\mathrm{d}N_e}{\mathrm{d}t} = -k_s \cdot N_s \cdot N_e \tag{3.12}$$

and therefore, for a homogeneous impurity contamination and drift field, the number of electrons N_e as a function of time is

$$N_e(t) = N_{e\,0}\ e^{-t/\tau} \tag{3.13}$$

where τ is the mean electron lifetime and $N_{e\,0}$ the initial number of released electrons. The lifetime is directly related to the amount of impurities.

$$\tau = \frac{1}{k_s N_s} \tag{3.14}$$

As shown in Figure 21, the rate constant k_s for attaching electrons is not only depending on the kind of molecule but also on the electric field strength. For electric fields up to $\sim$ 1 kV/cm, k_s is approximately constant for oxygen and Equation (3.14) can be written as [37]

$$\tau[\mu\mathrm{s}] \approx \frac{300}{\rho_{O_2}[\mathrm{ppb}]} \tag{3.15}$$

where $\rho_s = N_s/N_{Ar}$ is the amount of impurities of the molecule s with respect to the amount of argon.

Recent measurements of the electron lifetime in liquid argon have brought attention to water [67].

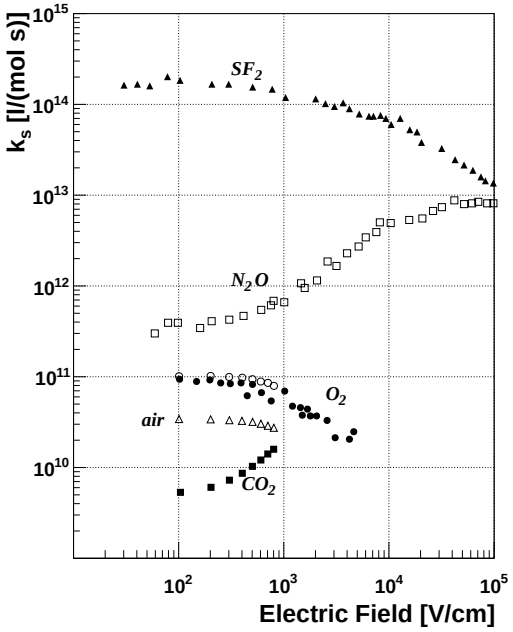

FIG. 21: Rate constant for the electron attachment to different molecules. The data points for SF_6 (▲), N_2O (□) and O_2 (•) are from [65], the data points for O_2 (∘), air (△) and CO_2 (■) from [66].

Derived from the presented data, a lifetime of

$$\tau[\mu\text{s}] = \frac{17.4 \pm 0.5}{\rho_{H_2O}[\text{ppb}]} \tag{3.16}$$

has been found. This measurement has been presented without any information about the electric field, used for drifting the electrons. In general, impurities are given as "oxygen equivalent" impurities. In that case, 1 ppb of water corresponds to ~ 17 ppb of oxygen.

3.9 Liquid argon purity requirements

As discussed in the previous section, a long drift path requires an ultra-high level of purity in the medium. The expected ionisation charge attenuation due to attachment to impurities as a function of the drift path for various oxygen-equivalent impurity levels and electric fields is shown in Figure 22. The arrows indicate the drift length of the ICARUS T600 [7], MicroBOONE [68], LBNE [69] and LAGUNA-LBNO GLACIER [16, 70]. The free of electro-negative molecules (like O_2, H_2O, etc.) must reach a level below 100 ppt O_2 level. An impurity level of < 30 ppt O_2-equivalent is needed to obtain an electron lifetime greater than 10 ms. Compared to commercially available bulk liquid argon deliveries which typically contain ppm-level purities, the goal is to reduce those impurities by a factor 10^4–10^5 before filling the main vessel tank. Excellent purity has been reproducibly achieved in various setups

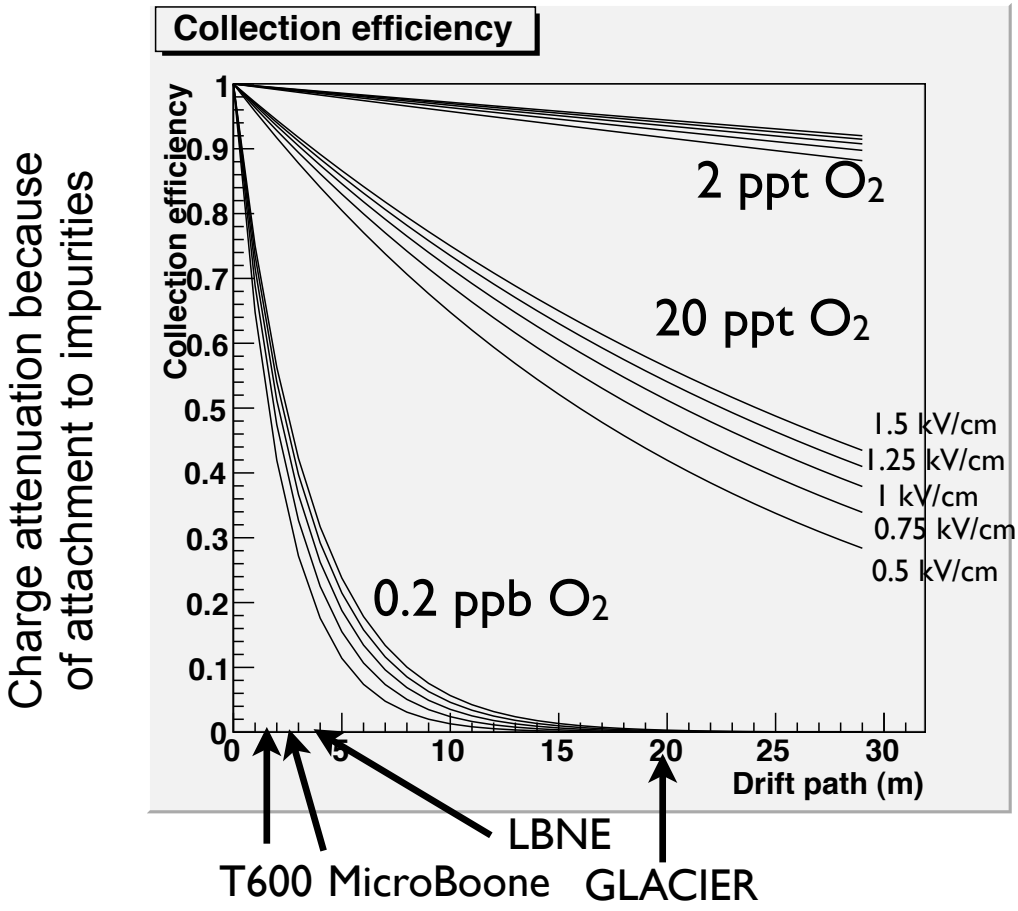

FIG. 22: Expected ionisation charge attenuation due to attachment to impurities as a function of the drift path for 0.2 ppb, 20 ppt and 2 ppt Oxygen-equivalent impurity levels and electric fields in the range 0.5–1.5 kV/cm. The arrows indicate the drift length of the ICARUS T600, MicroBOONE, LBNE and LAGUNA-LBNO GLACIER.

always relying on commercially available techniques, of various sizes and capacities, and should not pose a show-stopper for long drift paths.

Several independent groups performed numerical simulations and concluded that the vacuum evacuation of the main detector volume could be avoided for larger detectors, thanks to (1) a more favourable surface / volume ratio for larger volume (also larger volumes are less sensitive to micro-leaks), (2) a purification from ppm to << 1 ppb is anyhow needed since the initial purity of argon when delivered is typ. ppm O_2 (see above), and (3) the outgassing of material is mostly from hot components and impurities frozen at low temperature. GAr flushing and purging were shown to be effective ways to remove air and impurities. Purging on 6 m^3 volume has been successfully demonstrated [71]. The piston effect was seen in gas and the impurities reached 3 ppm O_2 after several volumes exchange.

Although the $6 \times 6 \times 6 m^3$ adopts a drift length which is significantly longer than the others such as ICARUS T600, MicroBOONE or LBNE as mentioned above, it should be noted that all experiments

require in order to collect efficiently ionisation charges a liquid argon purity in the range below 0.1 ppb = 100 ppt of oxygen equivalent (See Figure 22). Hence, the challenge to reach the required level of purity starting from commercially available ppm-level bulk argon is not mitigable by a shorter drift length in the meter range. It exists for all considered detectors.

4 Detector components

4.1 Anode Charge Readout Plane

4.1.1 The top anode deck

The top anode deck (see Figure 23) is composed of the reinforced frame holding the independent Charge Readout Planes (CRPs). The deck is suspended via ropes passing through dedicated feedthroughs. The large surface (36 m^2) to be instrumented with a large number (144) of individual modules. This will require a semi-industrial production with external suppliers and a dedicated QA/QC validation and calibration effort. The anode modules provide two independent coordinate views, and are segmented with strips of 3 mm pitch. The height of the deck is controlled externally and positioned precisely above the liquid level. The baseline option for the CRP is based on the LAr LEM TPC technique, as described in the next section. In addition, we are also developing a second option based on the MicroMEGAS technique, as described in Section 4.1.4.

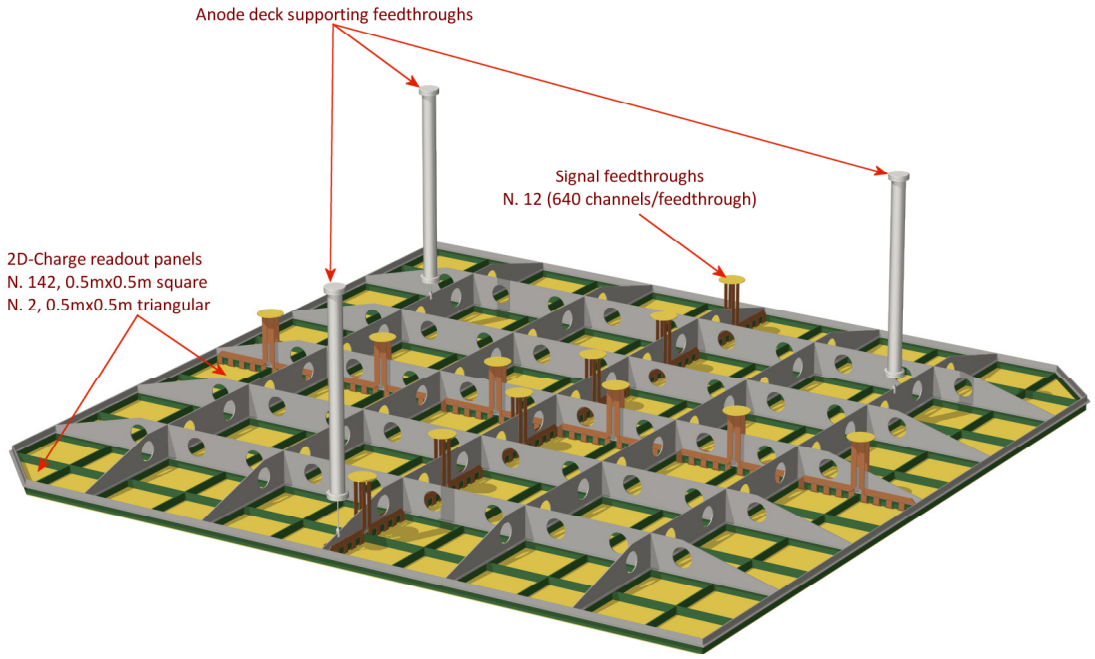

FIG. 23: The top anode deck.

4.1.2 The LAr LEM TPC option

The design concept of the novel Liquid Argon Large Electron Multiplier Time Projection Chamber (LAr LEM TPC) and its promising performances have been demonstrated experimentally with a detector prototype having an active area of 10 × 10 cm^2 [19, 20] and 40×80 cm^2[17, 18]. This new type of LAr-TPC, operating in the double-phase (liquid-vapor) mode in pure argon, is characterized by its charge amplifying stage (LEM) and its projective anode charge readout system. Situated in the vapor phase on top of the active LAr volume, these latter provide an adjustable charge gain and two independent readout views, each with a canonical and optimal pitch of 3 mm, since the amplification stage produces sufficient charge to be shared among several readout electrodes (smaller pitch sizes could be considered). With T_0 time information provided by the LAr scintillation, they provide a real-time three-dimensional (3D) track imaging with dE/dx information and the detector acts as a high resolution tracking-calorimeter. A high signal-to-noise ratio can be reached in the LAr LEM-TPC thanks to the gas amplification stage. This significantly improves the event reconstruction quality with a lower energy deposition threshold and a better resolution per volumetric pixel (voxel) compared to a conventional single-phase LAr-TPC [20]. In addition the charge amplification compensates for potential loss of signal-to-noise due to the charge diffusion and attachment to electronegative impurities diluted in LAr, which both become more important as the drift length increases. The collection-only readout mode (avoiding the use of induction planes) is also an important asset in the case of complicated topologies, like e.g. in electromagnetic or hadronic showers.

The extracted drift electrons in the vapor phase are finally drifted towards a collection plane where they are detected. Due to the applied electric field, electrons are accelerated in between two collisions with argon atoms and produce the *Townsend avalanche* (see Section 3.7). Being positioned on top of the LAr TPC in the vapor phase, the LEM is responsible for the multiplication of the ionization charges. Similar to the more established Gaseous Electron Multipliers (GEMs) [22], the basic idea of the LEM is to create electron avalanches in the gap of two holed metal planes, which are spaced by an electrical insulator. While the GEMs are made of 50 μm thick Kapton foils that are likely not applicable to cryogenic double phase detectors, the LEM or THGEM (for THick GEM) is a macroscopic, sturdy structure, made with standard PCB techniques. It consists of a 1 mm thick FR4 substrate with thin copper sheets laminated on both sides. The electrode-insulator-electrode sandwich is perforated with 800 μm spaced cylindric holes with a diameter of 500 μm. The view from top is shown in the scheme on the left and the picture on the right of Figure 24. The scheme shows that the hole diameter of the electrode (red) exceeds the diameter of the hole through the insulator (yellow). As demonstrated in [72] these so-called dielectric rims, typically about 50 μm thick, significantly

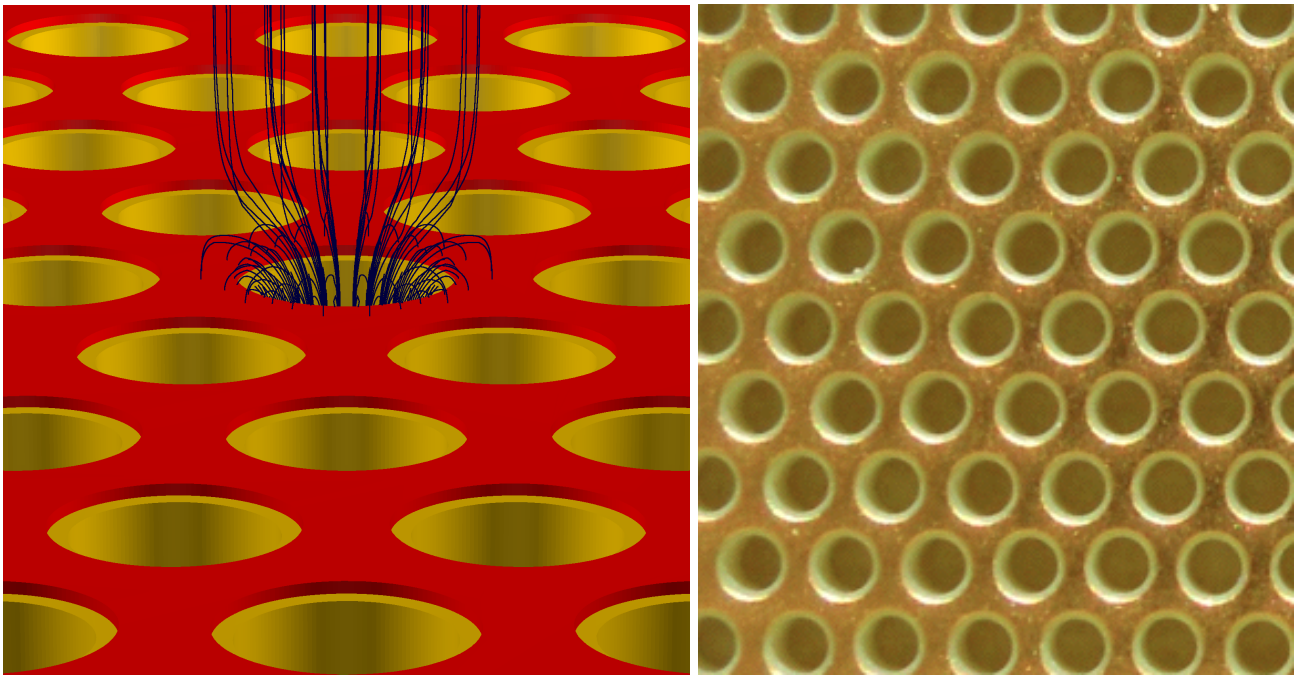

FIG. 24: Left: schematic drawing of the LEM, consisting of the copper electrode (red) and the insulating material FR4 (yellow). The field lines passing through the central hole are drawn in black. Right: closeup picture of a manufactured LEM. As in the schematic drawing on the left, the dielectric rim is clearly visible. [See text for more details.]

reduce the occurrence of discharges and therefore increase the maximum achievable gain. Besides the dielectric rims, the discharge probability is further reduced by the hole geometry of the LEM. Since the avalanche is happening inside the 1 mm long and 0.5 mm wide holes that are only surrounded by insulating material and no metal surfaces, secondary effects due to emitted scintillation light are suppressed. This is sometimes called *mechanical quenching*. A very detailed discussion of the discharge mechanisms, including finite element simulations, can be found in [73].

The 10×10 cm^2 and 40×80 cm^2 are characterised by (1) a single 1-mm-thick LEM amplification stage and (2) a 2D readout anode realized on a single PCB. The system has a multi-stage structure consisting of two extraction grids, a LEM, a 2D readout anode and two signal collection planes as illustrated in Figure 25. The distances between the stages and typical configurations for the potentials and the inter-stage electric fields are summarized in Table III. In typical configurations a positive HV of ~1 kV is applied to the anode while the extraction grid in liquid is operated at a negative HV of ~ −7 kV, resulting in a virtual ground within the LEM plane. The LEM is a macroscopic hole electron multiplier built with standard PCB techniques[133]. It is a 1-mm-thick FR4 plate, double-side cladded with a passivated copper layer. Of the order of half a million holes 500 μm in diameter are CNC (Computer Numerical Control) drilled through the plate at a pitch of 800 μm between the centers of adjacent holes. After the PCB has been manufactured and drilled, the copper layers are

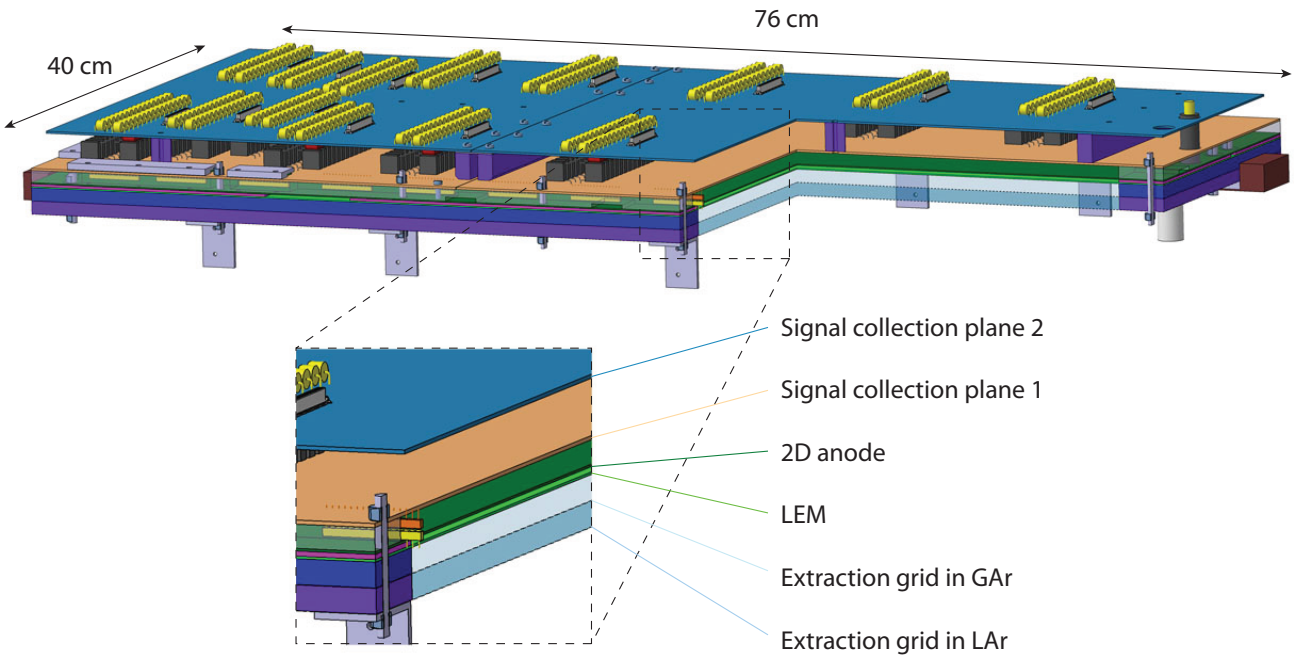

FIG. 25: Structure of the 40 × 80 cm^2 charge readout system incorporating a LEM (Large Electron Multiplier) and a 2D anode successfully built and operated. Right-front corner is cut in the illustration to present different stages in the multi-stage structure.

	Distance to the stage above (cm)	Typical operating potential (kV)	Field to the stage above (kV/cm)
Signal collection plane 2	–	0	–
Signal collection plane 1	2	+1	–
2D anode	1	+1	–
LEM (top electrode)	0.2	+0.5	2.5
LEM (bottom electrode)	0.1	−3	35
Extraction grid in GAr	1	−4	1
Extraction grid in LAr	1	−7	3
Cathode	60	−31	0.4

TABLE III: Baseline LAr LEM charge readout system configurations.

further chemically etched to create 40 μm wide rims around the holes. A HV of typically 3.5 kV is applied across the two faces creating a strong electric field of 35 kV/cm in the LEM holes leading to multiplication of electrons by avalanches. The 2D anode plane has two orthogonal sets of readout strips on the bottom face providing two independent readout views. On top of the strips for one view, those for the other view are laid with a thin (50 μm) polyimide (Kapton) insulating bed underneath. For each view, copper strips are formed by etching at a pitch of 600 μm covering nearly the full area of 76 × 40 cm^2. The readout pitch of 3 mm is obtained by bridging five strips at one end. The strips on top are narrower (120 μm) than those lying underneath (500 μm) optimizing for an equal charge collection by the two views operating at the same potential. A more detailed description of

the 2D anode can be found in Ref. [19] and references therein. The strips for both of the views are tilted by 45° with respect to the sides of the rectangular plate, to have symmetric conditions for both views. We use two signal collection planes, between which HV decoupling capacitors (270 pF) are connected. Each readout channel is routed to a collective 32-channel connector to a flat cable. A surge arrester protecting the readout electronics from discharges is mounted for each channel. The cables bring the signals through a custom-made feedthrough on the upper flange, connected to the readout electronics placed outside of the vessel. The LEM charge readout system is assembled as a multi-layered "sandwich" unit with precisely defined inter-stage distances and inter-alignment. The multiplied charges coming from the ionization in LAr are finally collected on a charge readout plane. The *2D anode* basically consists of two perpendicular sets of electrode strips (or: *views*), which are separated by a very thin insulating layer. Due to the semi-transparent design of the device, arriving charges produce a similar response on both sets of strips, finally delivering the two coordinates of the detected charges. Although the concept was adapted from the readout for GEM detectors [74], the design parameters had to be optimized for the application in a LAr TPC. In order to define an optimal electrode geometry, we have considered the response of a point-like energy deposition in LAr. As a consequence of the electric field focussing and defocussing by the extraction grids and the LEM but also the diffusion in gaseous argon, a δ-function like charge distribution in LAr arrives at the anode as a 1 mm extended charge cloud. Given this assumption, the induced signals on both views of the anode have to be mono-polar, fast and with similar amplitudes. Mono-polarity is guaranteed, since all the electrodes act in charge collection mode. As can be shown using the method of W. Shockley and S. Ramo [75, 76], electrons always drift against the weighting field of the corresponding collection electrode, inducing an entirely negative replacement current. Since the current is proportional to the electron drift speed in gas, the expected signal rise times are < 0.5 μs.

As sketched on top of Figure 26, the readout consists of a FR4 substrate with 500 μm wide copper strips (*covered strips*), spaced by 600 μm. On top of them, thin Kapton strips provide the electrical separation from the second set of 120 μm wide readout strips (*exposed strips*). The intrinsic readout pitch of 600 μs for each view ensures that even point-like charge deposits in the detector induce signals on both views, guaranteeing a correct reconstruction of the (x, y) coordinates. In order to collect in average equal amounts of charges on both views (exposed and covered strips), the local electric field was simulated with finite element methods[134]. It can be seen in the cut through the anode shown on the bottom left plot of Figure 26 that the exposed electrodes have a focusing effect on the electric field lines. Simulating different geometries, we have found that roughly half of the field lines end up on each of the two views if the width of the exposed strip equals 120 μm, as shown in the figure. The

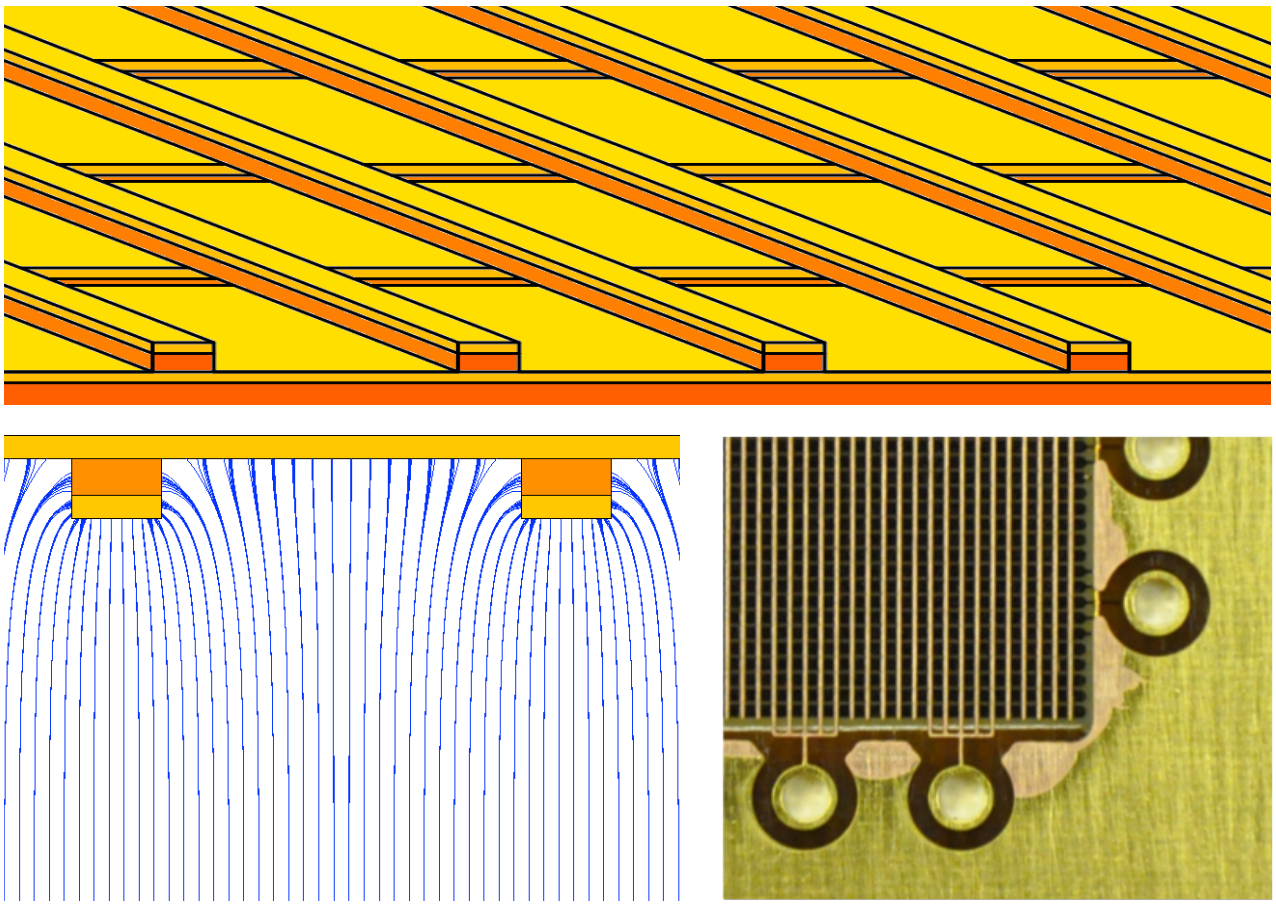

FIG. 26: Top: scheme of 2D anode (upside-down) with the FR4 substrate on the bottom (orange), followed by two perpendicular sets of electrodes (yellow), which are separated from each other by a thin Kapton layer (orange strips underneath the thin copper electrodes). Bottom left: electric field simulation to show that equal amount of charges are collected by both electrode sets. Bottom right: picture of manufactured 2D anode of the 3 L prototype [19].

picture on the bottom right of Figure 26 shows the anode of the 3L prototype. It can be seen that the desired readout pitch of 3 mm is obtained by connecting five consecutive strips with the intrinsic pitch of 600 μm together. Published performance obtained with these kind of detectors can be found in Refs. [17–20]. The 40 × 80 cm^2, the largest detector operated so far, has been operated during more than 1 month in 2011 under controlled pressure of ±1 mbar. The effective gain in stable condition was 14.6 with a $S/N = 30$ for m.i.p. The charge sharing between the two views was within 8%.

4.1.3 The CRP for the $6 \times 6 \times 6\mathrm{m}^3$

The CRP readout unit module of the 6×6×6m^3 is a direct extrapolation of the successful 10 × 10 cm^2 prototype [19] and 40 × 80 cm^2 [17, 18] to an active area approximately as large as 100 × 100 cm^2. No device of the final configuration has been operated yet, but simplification in the design compared to the previously operated chambers have been introduced and successfully tested on the 10 × 10 cm^2

chamber. Large data-sets of cosmic muons have been collected in order to further study the uniformity of the gain, the stability of the gain and signal-to-noise ratio for extended running periods, to monitor the occasional discharges across the LEM and detect any potential effect on the gain stability, and to finally simplify further the design in view of large scale production.

The new design has a simplified scheme with a single extraction grid allowing for higher electron transparency and less absolute voltage. A new anode design, based on a multilayer PCB with a new electrode design has been implemented to reduce the strip capacitance to about 100 pF/m, in view of large area detector with strip length up to 4 m. A chamber with the new design has been successfully operated over a period of several weeks with a chosen working point with gain at 15. A stable gain of 90 has been achieved at the highest fields with the new 0×10 cm^2 prototype, surpassing the anticipated working point for the $6 \times 6 \times 6$m^3 at a gain of 20.

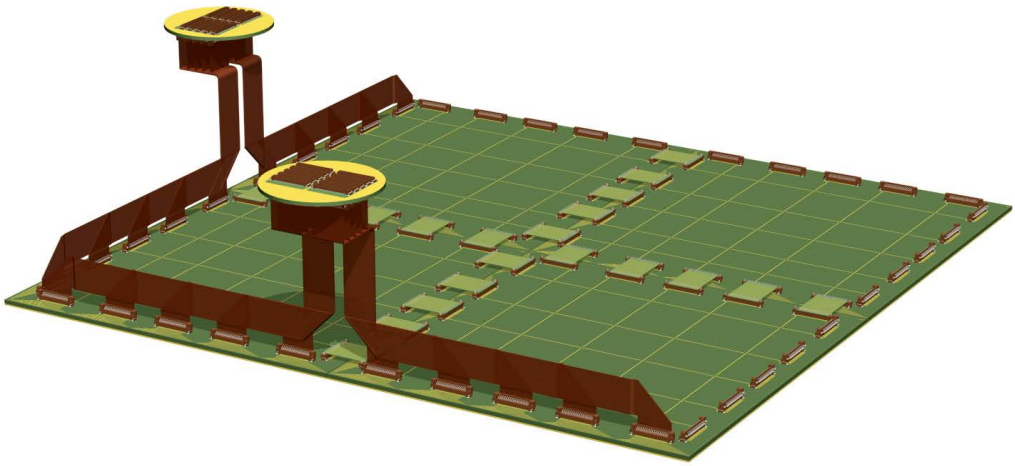

FIG. 27: Design concept of the 1×1 m^2 CRP.

Although not yet finalised, the design of the CRP for the $6 \times 6 \times 6$m^3 has made significant progress. The design concept is illustrated in Figure 27. The CRP module will be composed of four independent modules of 50×50 cm^2 with a single extraction grid. The LEM thickness will be 1 mm and the multi-layer PCB anode will have connectors on both ends. One end will connect to the signal cables bringing the signals to the signal feed-throughs, where the cold front-end preamplifiers will be located. The other will be used to connect two adjacent CRP modules. See Figure 28 for details. It is planned to assemble and test a first CRP module soon.

4.1.4 The MicroMEGAS option

Micro-Pattern Gaseous Detectors (MPGDs) such as GEM/THGEM/LEM are well established and high performance devices widely used in particle physics experiments. The MICRO-MEsh GAseous

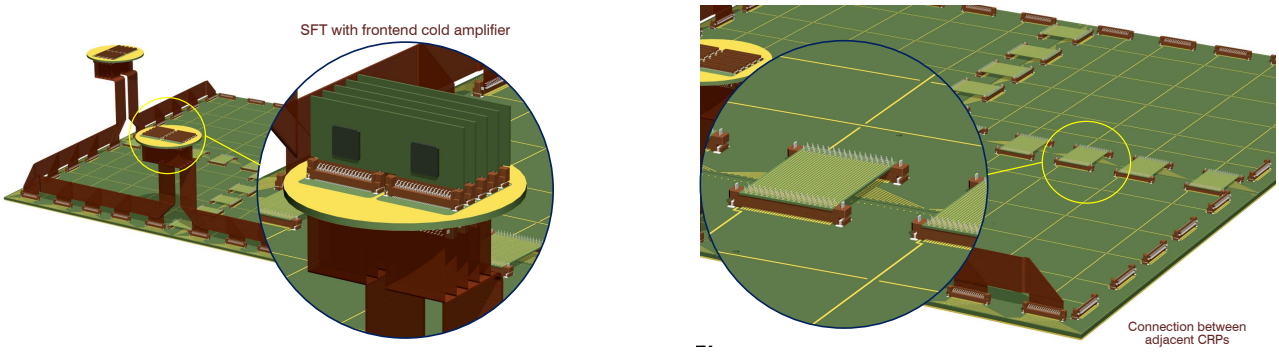

FIG. 28: Details of the 1×1 m^2 CRP: (left) signal feed-through (SFT) with cold frontend preamplifier; (right) signal electrical connection between adjacent CRP modules.

Structure or MICROMEGAS is a MPGD invented in 1996 which amplifies electrons in a typical 100 μm gap defined by a metallic micromesh placed on top of an anode Printed Circuit Board (PCB)[77]. In 2004, a new method to build this detector was introduced and called the bulk-micromegas[78]. A woven micromesh is embedded on top of the segmented anode plane of the micromegas by use of standard photolithographic techniques. This technology was chosen to instrument the 3 TPCs of the ND280 near detector of the T2K experiment for its performances in terms of gas gain uniformity, energy resolution and space point resolution, and for its capability to efficiently pave large readout surfaces with minimized dead zones. Eighty six 128 μm gap 34×36 cm^2 bulk-micromegas modules were produced in 18 months. Eighty of them, for an equivalent total surface of 9 m^2 passed the quality and performance tests. The dispersion of gas gain and energy resolution at 5.9 keV within the whole surface of each module were respectively 2.8% and 6% r.m.s. The dispersion of mean gain and mean 5.9 keV energy resolution over the eighty modules were found to be respectively 8% and 3% r.m.s[79]. These facts illustrate the maturity of the bulk-micromegas technology for a uniform, cheap and high quality mass production.

One advantage of the Micromegas technique is the possibility to easily produce large detectors, with a quality suitable for the instrumentation of a large area HEP detector. The industrial production of large area detectors is being investigated by the RD51 collaboration at CERN [135], in particular for the ATLAS Small Wheel project.

In 2010, the T2K IRFU group started a R&D to test the feasibility of using bulk Micromegas to instrument a double phase LAr. In the first phase, the gas amplification process was tested in argon at room temperature up to a pressure of several bars. Gains up to several hundred were observed. Then, a 10×10 cm^2 bulk Micromegas with an amplification gap of 128 μm was tested in the 3L ETHZ Liquid Argon TPC at CERN [80] (see Figure 29). The anode was made of 32 1D 3mm pitch strips. The device operated successfully in this cryogenic environment for several days. In particular the following

points were demonstrated:

- compatibility with the high purity environment;
- operation in the cryogenic environment;
- successful charge readout, with observation of tracks of cosmic rays;
- charge amplification, up to approximately 5.

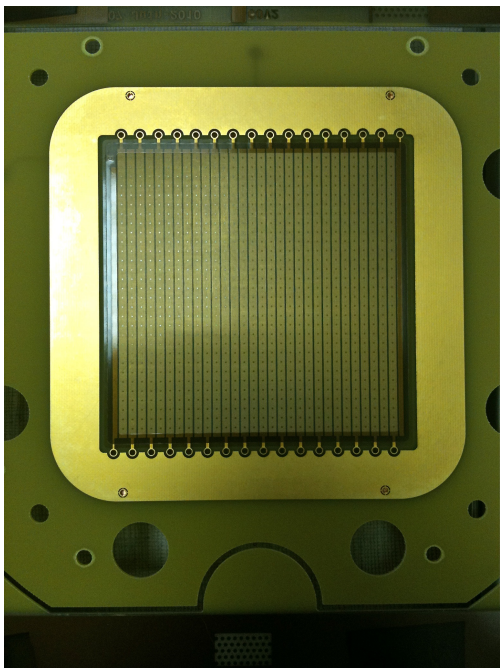

FIG. 29: The 10×10 cm^2 bulk Micromegas tested in a Liquid Argon TPC. It has 32 strips with 3mm pitch.

This first test gave therefore promising results. We plan to continue these tests in order to optimize the gain for the Liquid Argon application, in particular by testing several amplification gaps and several anode technologies. These tests are foreseen by the Saclay IRFU team in summer and automn 2013, with the setups at University of Liverpool and IPNL-Lyon, for a series of three Micromegas, with gaps ranging from 100 to 192 μm.

4.2 Drift cage

The drift cage is illustrated in Figure 30. It is composed of equally spaced rectangular electrodes which create an uniform drift field with a strength between 500 and 1000 V/cm, resulting in a drift

velocity of the quasi-free electrons ranging between 1.6 and 2.0 mm/s. The field cage is a self-standing structure, held together by FR4 vertical pillars, and supported on the floor by feet adapted to the corrugation of the membrane tank. The bottom of the field cage is closed by the negative HV cathode. The cathode is made of a strong frame with a mesh of tubes. The diameter of the tubes is 60 mm and their spacing is 500 mm. The mesh is filled with meshed grids with a wire diameter of 5 mm and pitch 50 mm. The transparency to light is about 80%, such that scintillation light produced within the liquid argon fiducial volume can be detected by the PMTs located at the bottom of the vessel. The HV feedthrough is placed in a corner of the field-cage. The top of the field cage is closed by the

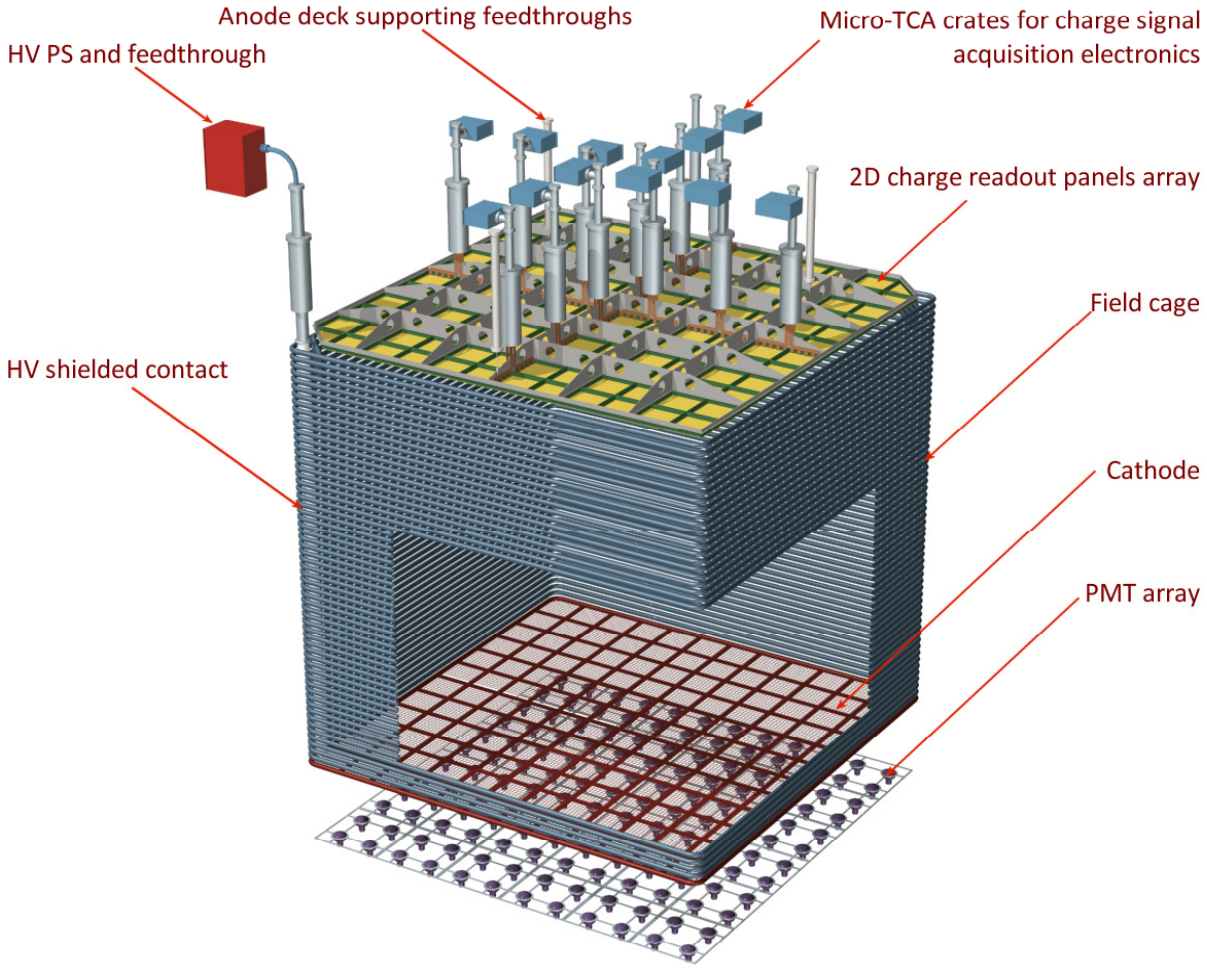

FIG. 30: Conceptual design of the field cage. The high-voltage feed-through is located in the left corner of the cage.

CRP anode deck. It should be noted that the anode deck is actually independently hung from the top via the supporting feed-through. The field-cage and the anode are therefore mechanically independent components, and the anode deck level is adjusted to the level of the liquid-gas argon interface.

4.3 Drift high voltage

The intensity of the drift electric field is one of the important design parameters for liquid argon time projection chambers (LAr-TPCs). A better collection of ionisation charges is attained by increasing the field intensity because: (1) more electron-ion recombination is prevented [11] and (2) attenuation of the drift electrons due to their attachment to residual electronegative impurities such as oxygen decreases. The dependence of the attachment cross section on the electric field is known to be weak in the practical range of the intensity (0.5–1 kV/cm) [10]. The attenuation then is described well by an exponential decrease with drift time, characterised by the drift electron lifetime τ which is determined dominantly by the impurity concentration. The mean drift velocity of the electrons increases with increasing electric field, leading to the shorter collection time and consequently to the less attenuation (see Section 3.8). The drift velocity increases by 30% by doubling the electric field intensity from 0.5 to 1 kV/cm, and again 30% from 1 to 2 kV/cm [81]. From a technical point of view, however, difficulties increase with increasing field intensity which requires higher voltages. Therefore, it should be determined by a right compromise between the detector performance and the practicality of the high voltage. A field intensity between 0.5 and 1 kV/cm is a reasonable compromise for very long drifts.

The loss of the dielectric properties (of a gas, liquid or solid) as a result of application of a strong electric field greater than a certain critical magnitude is called dielectric breakdown. The critical field at which the breakdown occurs is the dielectric strength of the material (or breakdown voltage). It depends on the geometry, on the thickness, the rate of the voltage increase, the shape of the voltage as a function of time, etc. In (pure) liquids, the breakdown mechanism is similar to that in gases where current carriers are free electrons and ions generated by external radiation. In the strong electric field, these particles acquire kinetic energy, large enough to ionise further molecules or atoms, potentially leading to streamers. Compared to gases, the liquid has the advantage of a much higher density, so in a first approximation one can expect the dielectric strength of liquids to be much higher than those of gases (proportional to their relative densities). However, it is known that breakdown in liquid can occur at much lower electric fields due to the formation of bubbles. The geometry of these latter is altered by the field lines and ellipsoids can form and merge into larger high-conductivity channels prone to discharges. A local increase of conductivity increases the temperature in the channel, the liquid can boil, the vapour enlarging further the canal. Such phenomena have for example been observed in liquid under the sudden application of strong electric fields, where electro-striction generates by cavitation a gaseous phase prone to discharges [82]. In general, the influence of a strong electric field in a liquid is

noticeable when the electric field density is comparable to the external pressure p:

$$\frac{1}{2}\epsilon\epsilon_0 E^2 \geq p \tag{4.1}$$

where E is the electric field. For liquid argon and in absence of bubbles, a field of 1 MV/cm=100 MV/m leads to ≈0.5 bar, which will have a noticeable effect. For comparison, the dielectric strength of polyethylene is in the range 20–160 MV/m. A field of 100 kV/cm in liquid argon yields a pressure of about 5 mbar. By assuming that the liquid argon in the $6 \times 6 \times 6\text{m}^3$ will be sub-cooled by e.g. 10 mbar via the liquid argon process system, the condition on the field strength to prevent formation of bubbles is set to $E \leq 100$ kV/cm.

For the $6 \times 6 \times 6\text{m}^3$, a drift field in the range $0.5 - 1$ kV/cm requires a potential difference at the cathode in the range of 300–600 kV. In comparison, the GLACIER drift length of 20 m [16] would require 2 MV. Two different approaches have been considered and realised for the drift field system for very large LAr-TPCs. The first type uses an external HV power supply and feed it into the detector volume using HV feedthroughs [7]. The second type has an internal HV generator directly inside the LAr volume as the Greinacher HV multiplier of the ArDM-1t detector [18, 83]. Its advantages are: (1) all the HV parts are immersed in LAr which has a large dielectric strength as discussed above, (2) thus feedthroughs for very HV are not needed, (3) the circuit itself can be used as a voltage divider, so the system needs no resistive load, (4) thus the power dissipation is virtually zero and (5) this allows a low frequency (e.g. 50 Hz) of the AC input signal which is fully outside of the bandwidth of the charge amplifiers used for this type of detectors. However, a major drawback is the difficulty to access the device in case of failure of a component, such as something that could realistically happen in case of discharge given the amount of energy stored in the circuit.

A HV feed-through and an external power supply will be adopted for the $6 \times 6 \times 6\text{m}^3$. Power supplies up to 300 kV with the required specifications in terms of stability, noise and low residual ripple, are commercially available in catalog (see e.g. Heinzinger electronic GmbH, Rosenheim(D)). Heinziger has also indicated that unique units for 400 kV have been successfully produced and operated. An R&D phase with industrial partners is considered to develop a 600 kV-able power supply. We note that the 300 kV would be sufficient to operate the $6 \times 6 \times 6\text{m}^3$ with the canonical drift field of 500 V/cm. However, in view of the longer drift paths, the $6 \times 6 \times 6\text{m}^3$ facility will be used to perform R&D on higher voltages, with the aim to reach a drift field of 1 kV/cm over 6 m.

As far as the HV feedthrough is concerned, it will be a direct extrapolation of existing design, with an insulating polyethylene thickness of 10 cm. Laboratory tests are been prepared.

4.4 Front-end and DAQ readout

4.4.1 Requirements for the large scale front-end electronics

One of the goals of the LBNO prototype is to establish the large scale readout systems being developed for the far site LAr detector in a configuration as close as possible to their foreseen final architecture. The full scale deployment of the readout systems in the prototype will allow testing their performance with high statistics samples of hadronic interaction showers, their stability and reliability over long time periods and on large data volumes as well as optimizing their integration in the detector.

The large number of charge readout channels, needed for the 20–50 kton LAr detector sizes for LBNO with channel count in the range of 500'000 to 1'000'000, naturally called during the last years for R&D efforts in view of the development of large scale readout solutions. These are characterized by high-integration levels, significant cost reduction and aims to performance improvement. The R&D activities focused on two main axes:

- the developments of cold front-end ASIC electronics;
- the optimization of the data acquisition system based on modern telecommunication technologies.

Both efforts aim to improving the effectiveness and the integration level of the complete readout chain and to cost reductions for the large number of channels to be implemented in the detector. Shortening of cables needed to bring the analog signals outside the cryostat and reduction of the electronic noise can be achieved using analog amplifiers operating at cryogenic temperatures. The current R&D on the front-end electronics is based on analog preamplifiers implemented in CMOS ASIC circuits for high integration and large scale affordable production [84]. The noise is reduced by exploiting its behaviour as a function of temperature, which has a minimum around 100 K, and thanks to the suppression of the cables used to bring signals outside the cryostat, increasing the capacitance at the input of the preamplifier. In our present baseline the ASIC analog amplifiers can be integrated on the feed-through flange terminating the chimneys on the roof of the tank, under the insulation layer, in order to be cooled to a temperature near that of liquid argon (see Section 4.4.2). This solution fully preserves all the benefits of the cold electronics, as described above, while guaranteeing at the same time accessibility to the amplifiers without affecting the inner volume containing ultra-pure LAr.

For what concerns the DAQ, solutions based on Ethernet capable "smart sensors" were developed. The "smart sensors" are Ethernet capable front-end DAQ/processing units acquiring large groups of channels. They are integrated with a time distribution system needed to align the data taken by

different units operating independently. Data are output on a Ethernet network and collected with a system of switches to a computing farm which builds the events on the bases of the time stamps associated to the data packets by the different sensors. This concept was further developed for the LAr readout, since the time of its first implementation in the OPERA experiment, with the following technical improvements [85]:

1. porting it to the Gigabit Ethernet standard;

2. adopting FPGA based virtual processors, in order to achieve cheaper implementation costs and become independent on the market of Ethernet capable front-end processors;

3. integrating the electronics in the micro-TCA form factor, becoming very popular in the world of commercial telecommunication applications;

4. developing a special time distribution system, derived from the Precise Time Protocol standard, integrated in a synchronous Ethernet network. This time distribution scheme achieves a synchronization accuracy among different nodes at better than 1 ns.

This DAQ scheme allows benefiting of the large-scale integrations developments of the telecommunication industry and decoupling from the market lifetime of commercial processors since it relies on a completely virtual implementation of the processors in the FPGA. A complete setup built out of this R&D was developed in 2010 for 128 channels (See Figure 31). The proposed DAQ version for the LBNO prototype detector is an evolution of that system, further increasing the channels density and reducing the costs.

FIG. 31: Picture of a micro-TCA crate containing DAQ boards with 32 ADC channels/board as developed in 2010.

4.4.2 Cold front-end electronics

Since 2006 till 2012, six generations of prototypes of ASIC 0.35 microns CMOS multi-channel preamplifier chips operating at cryogenic temperatures, typically reached in the gas phase above the LAr, were developed. This development was oriented to performance improvement for large size detectors and low cost production. See Figure 32.

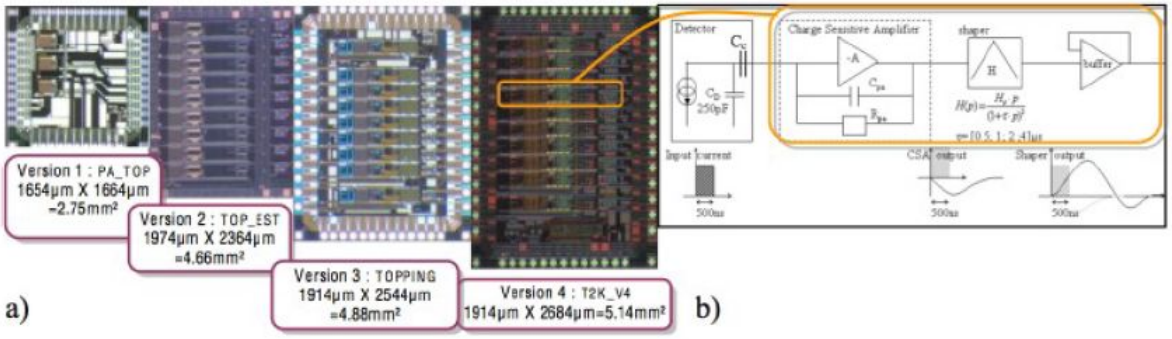

FIG. 32: Four ASIC chip die pictures (a) following the development of the different versions since 2007 and one channel block schematic (b) of the fourth version (V4)

Each amplifier channel on a ASIC chip includes a complete chain with a pre-amplifier, a shaper and a buffer. Some parameters of the analog chain chain response, as the shaping time, may be controlled for the group of channels in the same chip with a distributed I2C bus. The ASICs have a power dissipation of 18 mW/channel. The equivalent noise is around 1400 electrons, corresponding to a detector capacitance of 250 pF. The linear dynamic range extends up to 50 m.i.p. The ASIC configuration was mainly optimized for the most critical configuration of a detector with unitary gain, as a LAr TPC with wires readout, and the related possibility of dealing with bipolar signals as from induction planes.

The current ASIC development version (to be submitted in June 2013) includes 16 channels and the adaptation to a detector with unipolar signals from X and Y anode collection strips with 3 mm pitch and a LEM gain of 20 (See Section 4.1.3). The preamplifier gain is consequently adapted to cope with the detector gain and the dynamics is extended with a double slope regime (see Fig. 33) characterized with a high gain region up to 10 m.i.p signals after which the gain is reduced by a factor 3 matching a total dynamic range of 40 m.i.p. The total strips capacitance at the input of each preamplifier channel, will be around 300 pF, for 3 m long strips. Taking into account 20 m attenuation length of the charges during the drift, the S/N ratio for a m.i.p. signal will vary from 45 to 120 (m.i.p. tracks occurring at the beginning of end of the drift space) for the full size detector of LBNO, and from 90 to 120, for the prototype detector, which has 6 m drift space instead of 20 m. The front-end electronics will

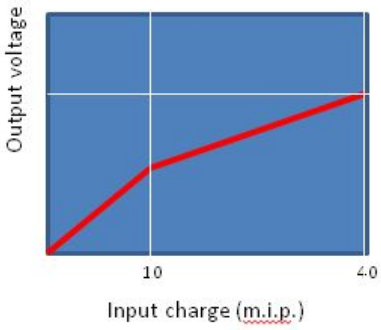

FIG. 33: Double slope gain adjustment for an extended dynamic range of the amplifiers.

be coupled to the DAQ system, described in the following, based on 12 bits ADC, well matching the needed dynamic range.

The design of the $6 \times 6 \times 6\text{m}^3$ prototype includes a total number of 7680 channels for the charge readout of the X and Y strips views. The strips have a pitch of 3 mm and a length of 3 m per channel. Channels are then arranged in groups of 640 per chimney (see Figure 34).

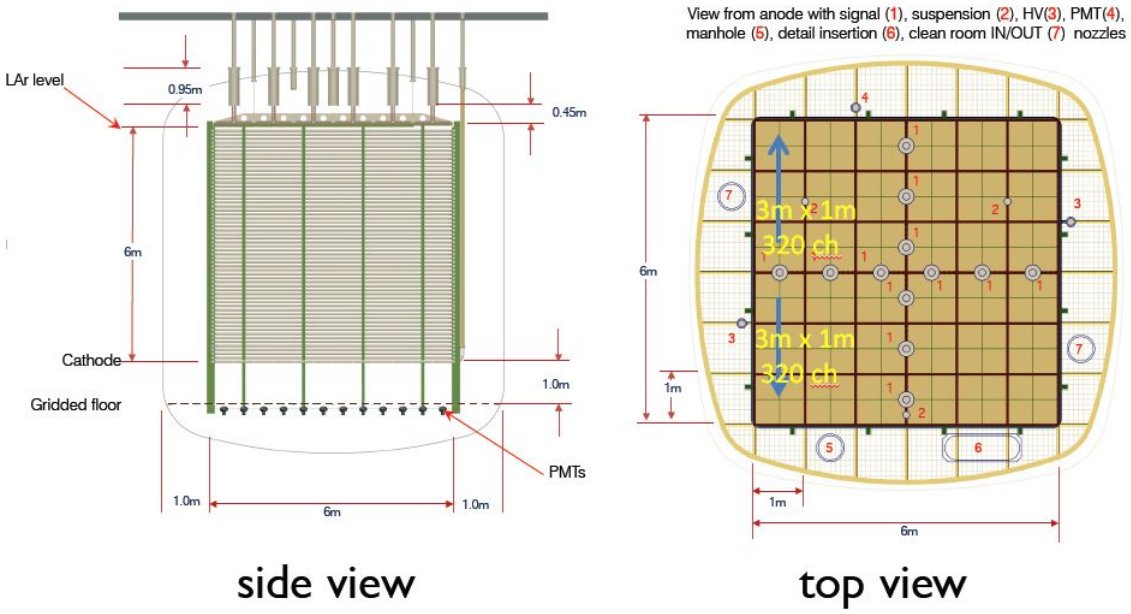

FIG. 34: Scheme of the distribution of the charge readout channels in groups of 640 per chimney.

The 40 ASIC amplifiers needed for the readout of each group of 640 channels will be arranged on cards hosted on the feed-through at the bottom of each chimney (see Figure 35).

The total power dissipation of the front-end electronics will be of of 11.5 W per chimney. The structure of the chimneys allows for heat dissipation in the cryostat and for minimising the connection length from the cards hosting the ASIC chips to the double phase detectors down to half a meter.

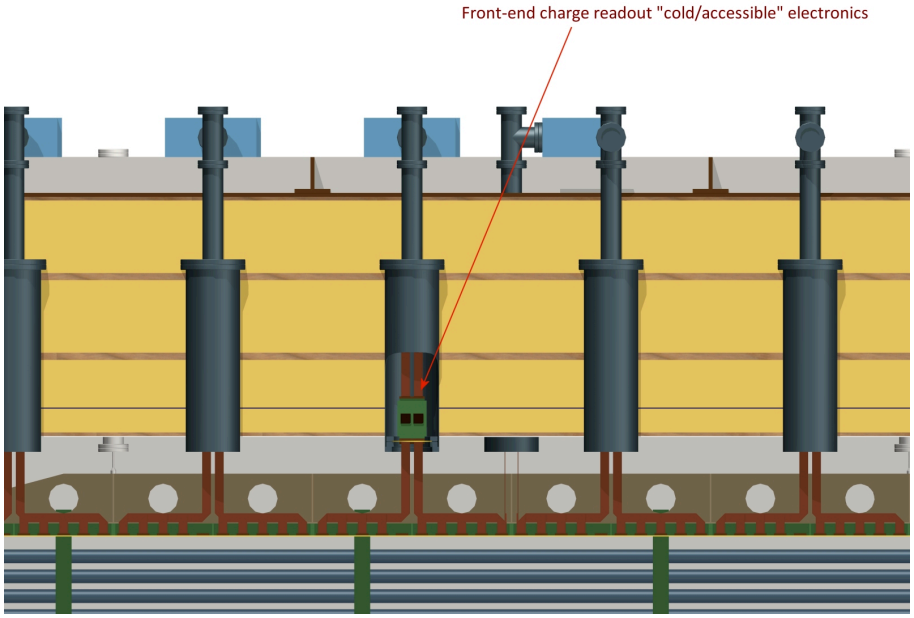

FIG. 35: Location of the FE cards at the bottom of the chimneys.

The ASIC chips needed to equip the final Far Detector can be produced in a dedicated run including 6 wafers for a cost going from 0.28 to 0.37 eur/channel, including encapsulation. This cost varies depending on the fact that the production version will be based on 16 or 32 channels per ASIC. This dedicated production can handle up to 28k ASIC chips in the 16 channels version (14k in the 32 channels version). The production volume needed for the LBNO prototype is much smaller and it will rely on an extended multi-project run with a consequently higher cost (3.91 eur/channel). The total cost per channel for the prototype detector goes up to 6.1 eur per channel when including also the front-end cards and the power supplies. The total cost for the prototype front-end electronics will amount to 54.2 keur, including 15% spare elements.

4.4.3 Fine-tuning of the F/E dynamic range

In order to fine-tune the dynamic range of the preamplifiers the amount of charge collected on the strips was studied with the simulated $6 \times 6 \times 6\text{m}^3$ geometry. The dynamic range should be large enough to allow the digitisation of highly ionising events while still providing good enough resolution for particles that deposit a small amount of charge on the strips (typically a fraction of a m.i.p). To understand the amount of charge collected on each strips, pions and electrons of energies up to 10 GeV were sent through the beam pipe and a distribution of the maximal charge deposited on each strip was retrieved. The results are shown in Figure 36 for the strips belonging to one of the views. Since the

beam pipe is orientated at 45 degrees with respect to the strips the distributions for the other view is identical. Most of the collected charge is below ~ 10 (resp. ~ 20) fC for pion and electron showers. The tails extend to about 50 fC and 100 fC for 10 GeV events. The dynamic range proposed in Section 4.4.1 is therefore suitable as it extends up to signals of 40 m.i.p (≈ 120 fC). In addition the double slope configuration of the preamplifier allows to adjust a range of increased sensitivity. This range is chosen for signals between 0 and 10 m.i.p (≈30 fC) as it is the region where most charge is collected.

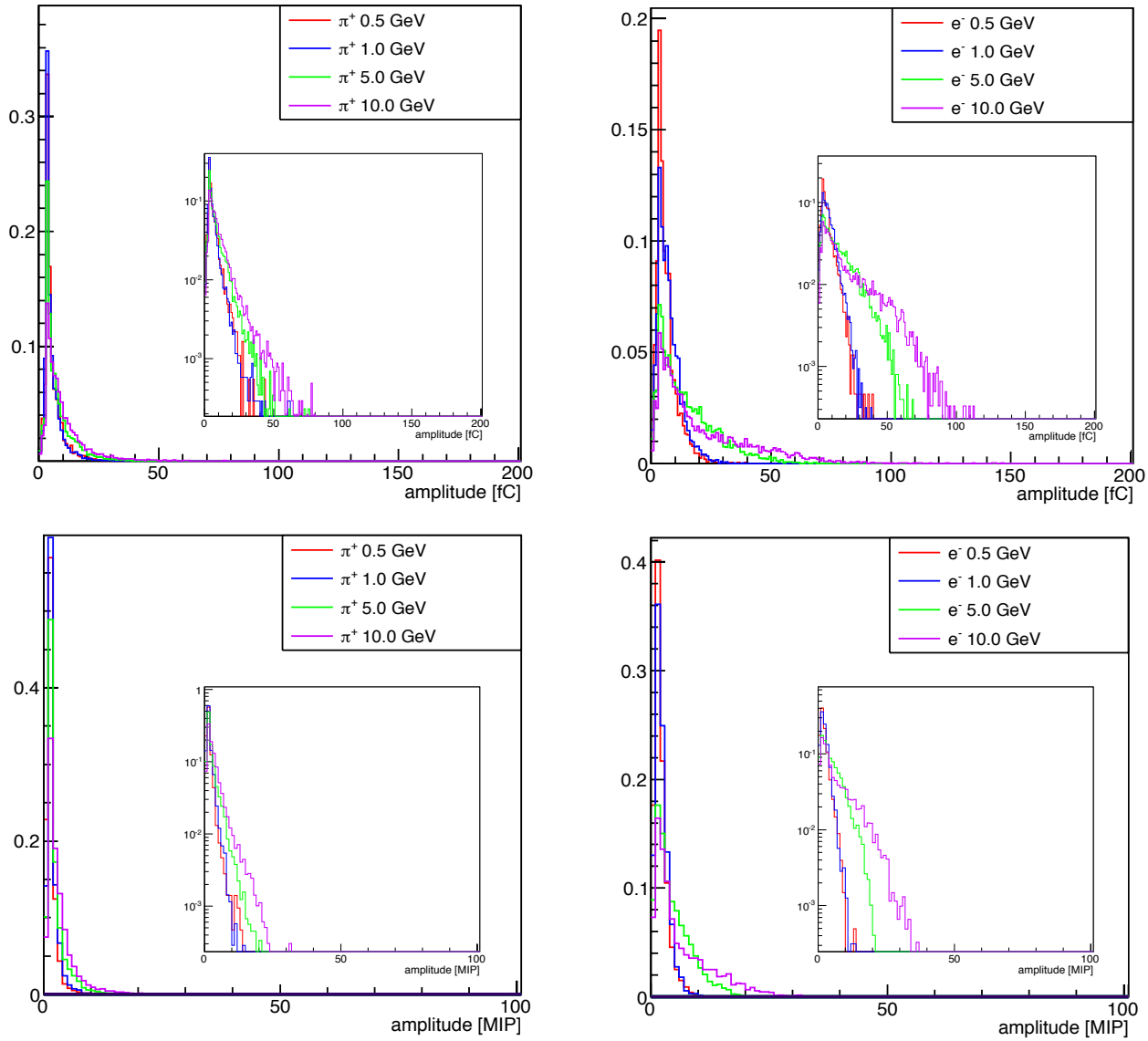

FIG. 36: Distributions of the maximal charge deposited on the strips for π^+ (left) and electron (right) showers of various energies. The distributions are given in unit of fC (top) and m.i.p (bottom).

4.4.4 Back-end electronics and DAQ global architecture

The DAQ system uses micro-TCA standards which offers a very compact and easily scalable architecture to manage a large number of channels at low cost. Those constraints are indeed very close to the one existing in the network telecommunication industry. This has been driving the very first developments based on this type of standards in constant technological evolution and applied to large scale neutrino experiments. A generic scheme of the DAQ architecture is displayed in Figure 37.

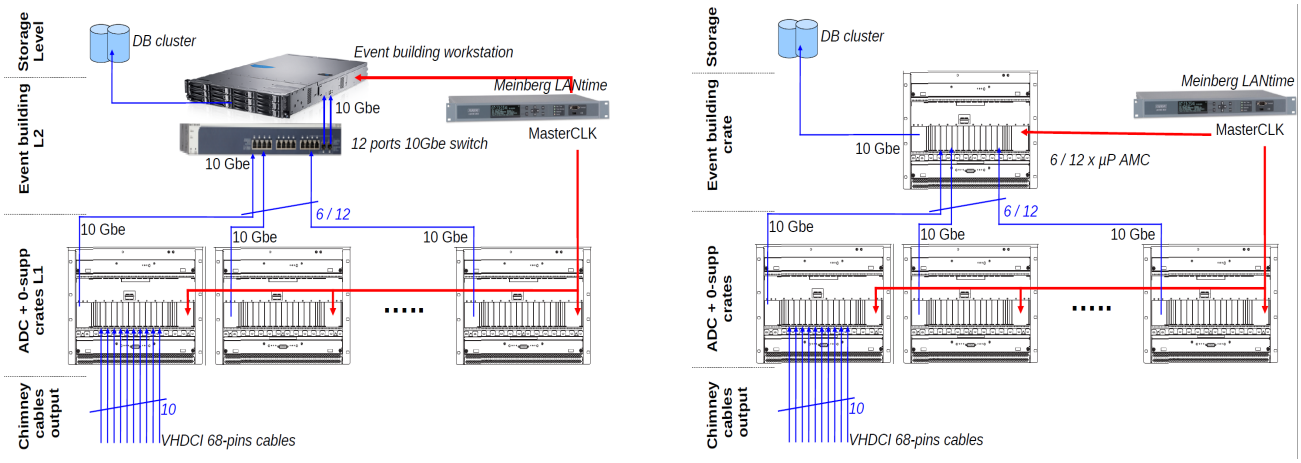

FIG. 37: Global DAQ scheme. At the bottom of each scheme the cables from the F/E electronics. 10 VHDCI cables are connected on each rack. In the baseline option one crate is foreseen per chimney, leading to 12 racks in total for the 1st level (L1). Each crate is connected through a 10Gbe uplink to the next level (L2). Left: the baseline architecture where the L2 directly connects the racks to the event builder workstation via a 10Gbe network switch. Right: 2-levels architecture with processor AMC (one per crate) collected in a crate. The database cluster stores high level processed data. A stable common clock is distributed to L1 and L2, as well as the trigger signals (from PMT and beam). The master clock generator may be derived from a Meinberg LANtime generator.

The main component of this DAQ system is an Advanced Mezzanine Board (AMC) reading out the input signals from the front-end electronics and sending the formatted data through a micro-TCA backplane using a Gigabit or a 10 Gigabit Ethernet link. In the following, details are given on the design of this AMC and the possible alternatives existing to the Ethernet link on the backplane (e.g. PCI express). The connections from the front-end use the Very High Density cable interconnect (VHDCI) standard to minimize the number of cables.

A micro-TCA crate (or shelf) interconnects a fixed number of AMC cards through the backplane to collect the data and send them through a standard 10 Gbe Microtca Carrier Hub (MCH) and to distribute a common clock signal issued from a single, stable, GPS-locked Master Clock (MC).

The clock is made available on the backplane through a dedicated AMC (one per crate) which receives it from an external connection, together with the trigger signals (internal trigger from the PMT array and external beam trigger). Those triggers are split and distributed through conventional

systems.

A network hierarchical structure is implemented where all crates are interconnected either to a standard 10 GBbe switch or to higher level crates in which dedicated micro-processor AMC perform further data processing, filtering and transmission to the highest level for storage. Since the requirements on that higher processing level are not so constraining and more flexible for the present detector design, a standard 10 Gbe network level is foreseen in the present proposal.

The storage is defined as the highest level of the DAQ chain and implies the use of a redundant 2-servers cluster linked to a RAID-5 disks array system.

4.4.5 MicroTCA standard and crates

MicroTCA offers the possibility to interconnect distributed applications while offering a standard, compact and robust form factor with simplified power supply management, cooling and internal clocks distribution. The microTCA backplane is based on high speed serial links arranged in various possible topologies. Lanes on a microTCA backplane support a large variety of protocols like for example Ethernet 1G or 10G, PCI Express or SRIO.

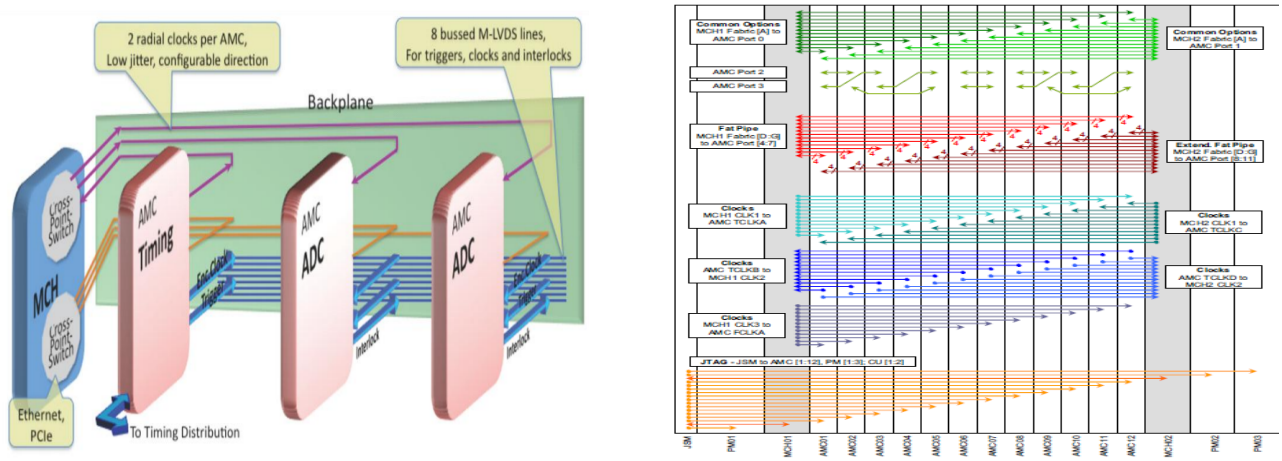

FIG. 38: Left: global microTCA crate organization. AMC cards (providing basic ADC functions) are connected to the crate controller or MCH which uplinks the external systems. A dedicated AMC for the clock receives dedicated signals (masterclock, trigger signals) from the timing distribution system and transcript them onto the backplane. Right: backplane technology of the Schroff 11850-015 reference.

The boards plugged into a microTCA shelf are called Advanced Mezzanine Card (AMC) [86]. Each AMC board is connected to one or two MicroTCA Carrier Hub (MCH) through the backplane serial links which provides a central switch function allowing each AMC to communicate with each other or towards external systems through an uplink access. The backplane also provides the connectivity for the clock distribution allowing the AMC board synchronisation. Figure 38 provides a sketch of the backplane technology and its implementation in one retained shelf reference.

The first developments performed for the LAr TPC readout with the microTCA systems were based on the microTCA.1 standard with connections to the user input signals from the front side only. In the baseline option we stay as close as possible to this standard although additional standards have emerged like the microTCA.4 offering the possibility to enter in a crate both from front and rear sides.

In the microTCA.4 standard each slot of a crate's backplane is linked directly to one AMC and indirectly to one microRTM card. Both cards may offer similar functions for the user but only the AMC manages the link with the backplane. On the Figure aside one compares the naked PCB's of AMC and microRTM cards and to a standard VME board. The main drawbacks of this microTCA.4 option are the requirement of a double development since AMC and microRTM cards are not symmetric and more stringent constraints on each slot's bandwidth. Nevertheless this option may be evaluated.

In the microTCA.1 baseline option, one has 1 crate per output chimney, handling 640 channels dispatched over 10 AMC. A candidate crate is the 11850-015 8U shelf from Schroff (Figure 39). We are also considering other references from various providers (like the NATIVE-R9 from NAT) in the spirit of evolving to the microTCA.4 standard. In this case each crate will be located between 2 nearby chimneys. The main features of the 11850-015 Schroff crate references are listed below:

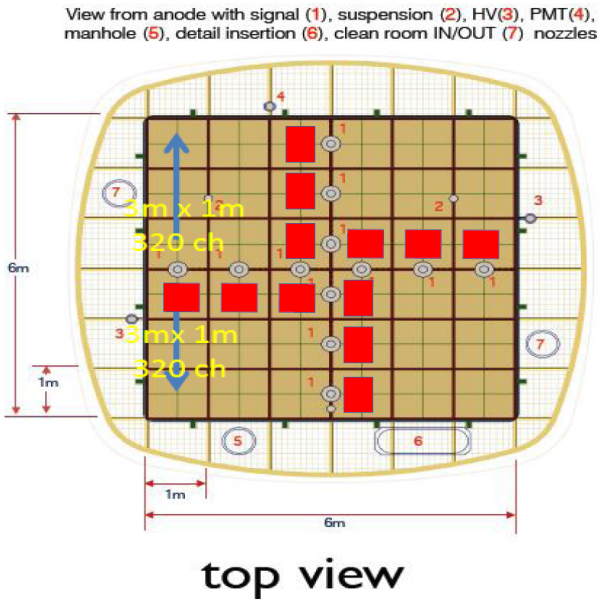

FIG. 39: Left: picture of the Schroff 11850-015 8U shelf. Right: sketch of crates implementation on the top layer of the prototype detector. Each red box features a crate. The inter-chimney distance, of the order of 1 meter, allows this type of crate disposal which minimizes the constraints on cables lengths.

- 8 U microTCA Shelf, 12+2+3+1 slot for AMC double Mid-size modules,
- 19" rack mountable,
- 12 AMC Double Mid-size slots,
- 2 redundant MicroTCA Carrier Hub (MCH) slots (Double Full-size),
- 2 Power Module (PM) slots (6 HP Double) at the right side,
- 1 Power Module (PM) slots (12 (9) HP Double) at the left side,
- 1 slot for a JTAG module (Double compact),
- 5 splitting kits to install single module in a double slot.

Various MCH references may be used in that design. The VADATECH MCH(UTC001) is available with PCIe, SRIO, 10GbE layer three managed, GbE layer two managed and SAS fabric interfaces. It runs Linux 2.6 on its MCMC CPU and is hot-swappable and fully redundant when used in conjunction with a second instance of the module. The NAT MCH has comparable features, SRIO (Gen2), PCIe (Gen3), 1GbE and 10GbE (XAUI), central management up to 13 AMCs, 2 cooling units and 4 power modules, e-keying, redundancy and load sharing. Final choice will be driven by the performance and the cost.

4.4.6 MicroTCA dedicated AMC

a) AMC board design

The idea is to develop only the user AMC offering the desired functions. The generic functional diagram of the AMC is displayed in Figure 40. The AMC chosen is a double-size module (also compatible with microTCA.4 standard) with a single input connector and a 10GbE or PCIe link to the backplane. The input stage performs the 64 channels digitization through 8 8-channels 14-bits ADC readout at a 2.5MHz frequency. The ADC readout sequence is controlled by 2 EP3C40 FPGA from Altera which makes the data available on a double port memory (DPRAM with 9k-samples width from IDT). Two banks (B0/B1) are attached to each channel and work in ping pong mode. The write state machine manages the bank address working as a circular buffer. If no trigger conditions is detected the samples are written continuously into the memory, the oldest ADC being overwritten by the newest ones. The ADC values and the address location in the bank are written into an intermediate FIFO for each bank (B0/B1). If a trigger occurs, the write state machine keeps on storing the event corresponding to the TPC drift. If the second bank is available, the main state machine tells the write state

machine to continue to store the samples into this new active bank. The read state machine sets a flag corresponding to the availability of an event in a bank. All the read state machines are interconnected through a token ring like structure. The zero-suppression algorithm is applied on all samples available in the bank, the pedestals (mean and width) being computed on the samples themselves. The recorded samples are then formatted and sent out. These operations are managed by a third FPGA (EP5CE from Altera), which sends the data on the backplane. The baseline option foresees to send the data directly through a 10GbE link (UDP was used in the first prototype). The readout scheme and hardware implementation is very close to the first prototype designed in IPNL (Figure 40) with slight changes: replacement of the single FPGA by three cost-effective FPGA's and direct implementation of the ADC layer on the motherboard (in the first version ADC's were on a mezzanine board).

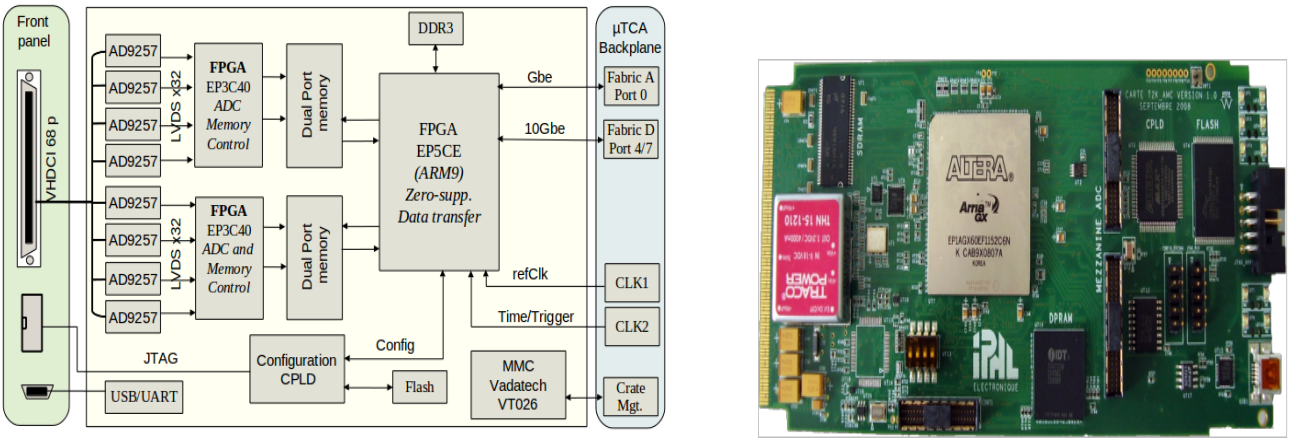

FIG. 40: Left : AMC bloc diagram scheme. The input stage digitizes the 64 input channels. The ADC readout sequence is controlled via 2 FPGA (one for 32 channels) which handles also the writing into a double bank memory. The management of the trigger input, data output, and link to the backplane if performed by a third FPGA. The link to the backplane may be direct 10GbE or PCI-e. Right: the first AMC version, single height for 32 channels. Present design is an extension of this board.

b) ADC readout chain

The analog signals from the F/E ASICS are connected to the AMC front-panel through a 68 pins VHDCI connector. The 8×14-bits ADC 8 ch. AD9257 ADC from Analog Device, including a serial LVDS output, has been chosen. The translation from single ended to differential signals is performed upstream of the ADC. The readout scheme is displayed on Figure 41. This design offers a high integration level required by the large density of input signals.

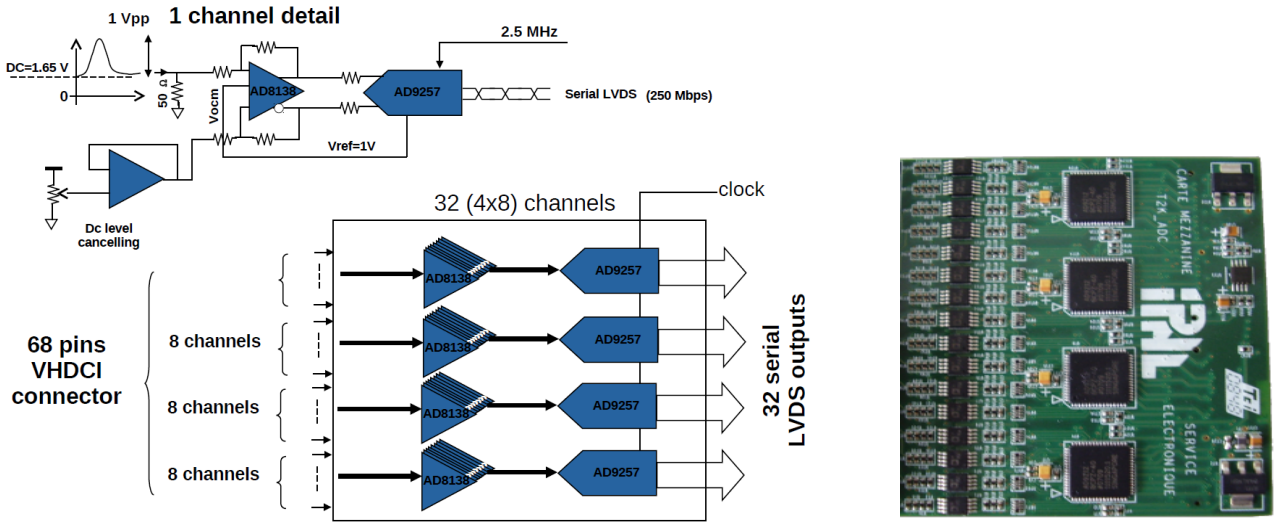

FIG. 41: Left : ADC readout chain block diagram. The AD amplifier is used to translate the inputs to differential levels. Right: implementation of a 32 channels ADC readout chain in the first prototype version.

4.4.7 Data rate requirements

a) Data reduction

In the present design the useful ADC will be 12-bits resolution and each sample will have 16-bits size. The readout frequency of 2.5 MHz (400ns steps) requires a maximum of 10k samples for the maximal drift time of 4000 microseconds that we want to cover. Given the 6 microseconds shaping of the F/E electronics for a single hit, one obtains: 6(μs)/400(ns)~15 useful samples for a single hit over the 10k of a full bank. To be conservative we assume in the following a 100 reduction factor given by the zero suppresion algorithm.

b) Data rate constraints

In this context we may compute the saturation limits for one crate and for the full detector. One crate is used to readout a full chimney, that is 640 channels (10 AMC). The maximal affordable data rate to saturate the 10GbE uplink of the crate is therefore: 10(GbE)/(16(bits)×640(ch.)×10k(samples)/100(zero-suppression))≃10kHz. Given the fact that we have 12 crates of the same type, the actual limit for the full detector is around 800Hz of external trigger rate. This allows a comfortable margin to record beam events and take cosmic data between the beam cycles or the beam spills.

4.4.8 Detailed costs

A detailed survey of market prices has been undertaken to evaluate the total cost of the present DAQ design, including AMC, fully equipped crates (MCH, power modules, cooling units), data network

(10GbE inputs and uplinks), data computing and data storage. The details are given in the Table below. The present estimates lead to a cost per channel of 27euro for the microTCA-DAQ system,

Item	Unit cost (euro)	Number of items	Total cost (keuro)
microTCA crate	3500	12	42
AMC board	850	120	102
MCH	1500	12	18
AMC clock	1500	12	18
VHDCI cables	75	120	9
Master CLK	5000	1	5
10GbE switch	3500	1	3,5
Event building WS	3000	1	3
DB cluster	5000	1	5,5
Total	-	-	206

TABLE IV: Costing details for the TPC readout microTCA DAQ + network + computing system.

network and computing. Details on the costs of the AMC board are provided below.

Item	*Unit cost(€)*	*Number of items*	*Total cost (k€)*
ADC : ADC9257	*36*	*960*	*34,6*
FPGA : EP3C40F324C8	*60*	*240*	*11,4*
FPGA : EP5CEBA2U15C7N	*40*	*120*	*4,8*
IDT : IDT70V7339S200BC	*50*	*480*	*24,0*
SDRAM	*10*	*120*	*1,2*
FLASH	*5*	*120*	*0,6*
Local PS	*50*	*120*	*6,0*
PCB 14 layers	*75*	*120*	*9,0*
Mounting	*80*	*120*	*9,6*
Total cost	**843**	**120**	**101,2**

FIG. 42: Details of an AMC board unit costs.

4.4.9 Integration of readout electronics

In the LBNO far detector, several hundred thousands channels will need to be routed from the charge readout plane located inside the vessel to the front-end charge preamplifiers and digitisers to be placed outside the vessel. Given the large number of channels, it will be necessary to pack as many of them into a single flange.

As shown in Figure 27, signal cables of the $6\times6\times6\text{m}^3$ will be similarly routed towards the top of the detector and connected to the signal feed-through flange at the bottom of a chimney. Each chimney will be terminated with a feed-through that must be absolutely ultra-high vacuum leak-tight not to contaminate the pure liquid argon. The dimension of the chosen flange is an ISO CF 200/250 to host 640 channels (20 KEL corporation connectors (`http://www.kel.jp/`) with 20×32 channels) as shown

FIG. 43: Signal feedthrough and connectors from the CRP (left) 3D view (right) 2D top view.

in Figure 43. The flange is actually made of a SS ring, in which a several mm-thick multilayer PCB is glued or sealed. The multilayer PCB is designed in order to accommodate connectors on both faces, but internally signals are routed along a U-shaped path, where the an inner PCB layer is shifted with respect to the top and bottom layers, in order not to have passing through holes. A prototype with 4 connectors has been built and tested (see Figure 44).

As mentioned, the signal flanges will be located at the bottom of their chimneys, and below the thermal insulation panel (See Figure 35). The temperature of the F/E electronics will be close to that of liquid argon and will be monitored remotely. The F/E cards with the preamplifiers will be inserted vertically into the KEL connector. The power dissipation per chimney is 11.5 W which will be taken away to the main vessel. The chimney will be flushed with dry nitrogen and sealed at the top of the chimney. For the final LBNO detector, this concept will be further developed as to allow access and exchange of the front-end electronic boards, independently of the main vessel which can remain filled with liquid argon. We believe that this is an important requirement for the potential long-term (>10 years) operation of the underground detector.

FIG. 44: Prototype of the signal feedthrough flange with 4 connectors.

4.5 Light readout

4.5.1 Primary and secondary scintillation light

Ionizing radiation in liquid noble gases leads to the formation of excimers in either singlet or triplet states [87, 88], which decay radiatively to the dissociative ground state with characteristic fast and slow lifetimes ($\tau_{fast} \approx 6$ ns, $\tau_{slow} \approx 1.6\mu$s in liquid argon with the so-called second continua emission spectrum peaked at 128 ± 10 nm ([89]). This prompt 128 nm scintillation light is exploited in liquid Argon TPCs to provide the absolute times (T_0) of the ionization signals collected at the anode, thereby after matching providing the absolute value of the drift coordinate of fully contained events.

Secondary scintillation light is produced in the gas phase of the detector when electrons, extracted form the liquid, are accelerated. This because the gas is less dense and the mean free path of the electron is longer, i.e., the extracted electrons can gain enough energy to excite argon atoms in collisions so that scintillation light appears. The amount of light is directly proportional to the amount of charge reaching the gas phase. This again is proportional to the amount of charge initially released by the interaction in liquid argon.

Measurements reported in [52] show, depending on the applied field, an amplification in gas of almost 100 photons per electron according to

$$Y_{S_2}/p = 81E/p - 47 \tag{4.2}$$

where p is the gas pressure, $[Y_{S_2}/p]$ = photons/(electron cm bar) the reduced secondary scintillation yield and $[E/p]$ = kV/(cm bar). This formula is valid for room temperature. For the operation at cryogenic temperatures of about 90 K (e.g. argon vapor at 1 bar) the pressure has to be multiplied by a factor 3.36 due to the higher density.

For the extraction with the ArDM detector, a light yield Y_{S_2} of

$$Y_{S_2} = (81 \cdot 4 \text{ kV/cm} \cdot \frac{1}{3.37 \text{ bar}} - 47) \cdot 3.37 \text{ bar} \cdot 0.5 \text{ cm} = 83 \text{ photons/electron} \tag{4.3}$$

is obtained.

The time between the occurence of the primary scintillation light an the secondary scintillation light is equivalent to the drift time of the electrons from the vertex to the liquid argon surface. Figure 45 shows a screenshot from the oscilloscope of a cosmic muon crossing the detector. It interacts with the argon atoms on its straight path through the detector. This means there is a continuous extraction of electrons, what can be seen. Taking the time of 400 μs, during which the signal is recorded (events at

a later time are pie up events) and the total length of the drift cage of 600 mm, this leads to a drift velocity of ~ 1.5 mm/μs. With the given electric field of ~ 480 V/cm the measurement agrees with values from literature as also the curve in Figure 15.

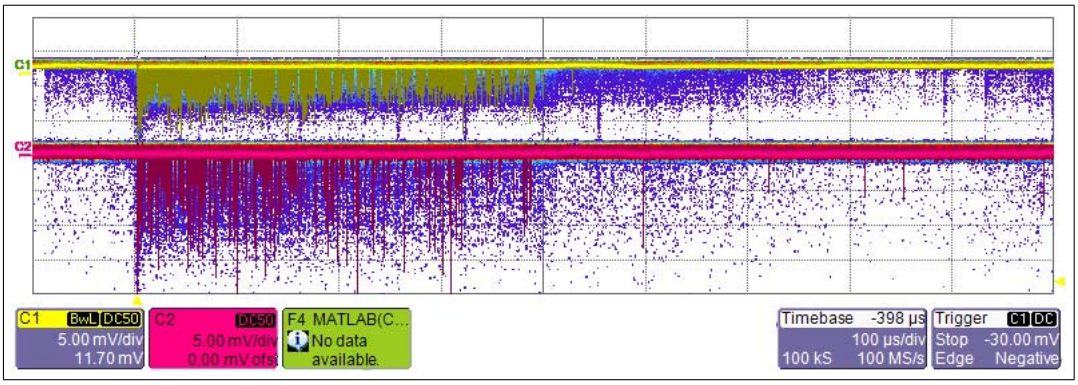

FIG. 45: Oscilloscope screen shot of the secondary scintillation light of a crossing muon through a LAr-TPC with 60 cm drift length and two PMTs at a timebase of 100 μs/div. The yellow and red signal of the two PMTs show a signal for the first 400 mus what can be translated in a drift velocity of ~ 1.5 mm/μs. The violet signals are the signals from previous events in the persistence plot and signals after 400 μs are from pile up events.

4.5.2 Scintillation light detection

Efficient methods to detect the scintillation light in the DUV range have been studied in the context of ArDM-1t for several years [57, 90, 91]. The practical technique for photo-detection based on large area cryogenic photomultipliers coated with a wavelength-shifter is thus well understood. For the WLS, we seek a fast response of the light readout system not to distort the pulse shape of the liquid argon scintillation light. Most organic wave shifting materials are well known for their fast optical response caused by the rapid process of radiative recombination of electron hole pairs at the benzene rings in their chemical structure. The best WLS and commonly used for its well matched emission spectrum to bialkali photocathodes is the Tetraphenyl-butadiene(1,1,4,4-tetraphenyl-1,3-butadiene or TPB). Different methods for coating the WLS have been studied in Ref. [90]. TPB coatings can be made durable with good adherence to the substrate and high resistance to mechanical abrasion. The light collection efficiency is also well reproduced by simulations [91].

Based on this expertise, we have developed a design for the light readout of LBNO which is composed of large area cryogenic PMTs placed uniformly below the (transparent) cathode. We have estimated that the number of PMT needed to have an efficient light threshold above several MeV is approximately 1000 if we adopt 8" photomultipliers with a conservative quantum efficiency at liquid argon temperature of about 10%. The PMT are uniformly located with a coverage of about 1 per square-meter. Their buoyancy in liquid argon (approx 4 kg) is compensated by appropriately adjusting the weight of their

support. They are anchored at the bottom of the tank, or possibly to the side of the inner shell wall. See Figure 46. The HV cathode is placed at a height of 2 m above the bottom of the tank and the PMT plane will be distant enough from the cathode plane, taking into account the high electrical rigidity of liquid (several MV/cm). In order to protect the PMTs an additional mesh plane will be installed and placed at an identical potential as the PMT photocathode. The PMT will be negatively polarized to about 1 kV such that the PMT signal can be readout in DC. We are presently in contact with Hamamatsu Photonics to define the most optimal configuration of PMT satisfying our requirements, in particular large area (8" or 12" PMT options are being discussed), cryogenic operation, high pressure operation (the PMTs will feel about 2 bar absolute), and potentially high QE photocathodes.

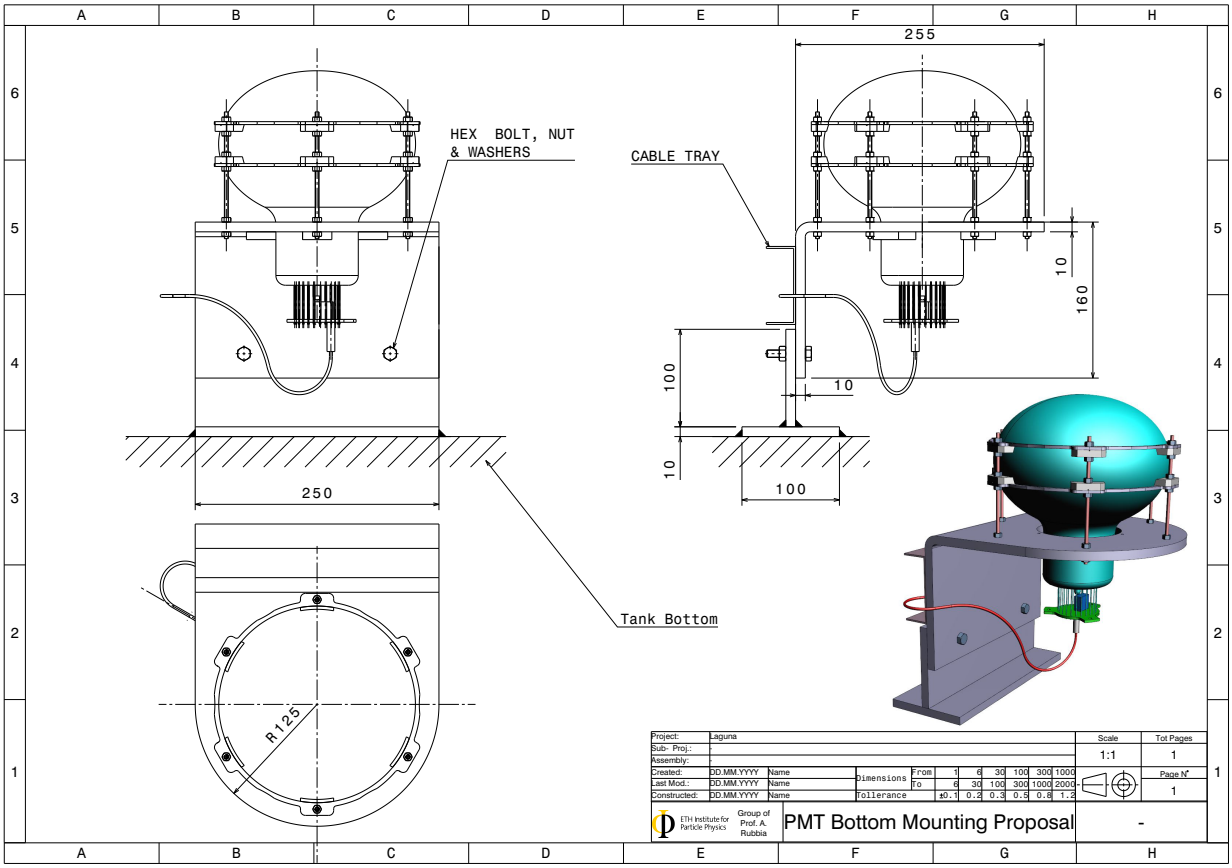

FIG. 46: PMT mounting arrangement on the bottom of the vessel and its fixation.

4.5.3 Light readout front-end digitiser and DAQ

In view of the large scale application for the 20 kton detector, which will include about 1000 photomultipliers with a density of one per square meter, the LBNO prototype will allow developing and testing low-cost and high-integration level solutions for the photomultipliers signals digitisation on large equipped surfaces. Solutions of this kind have been naturally studied, in the framework of the

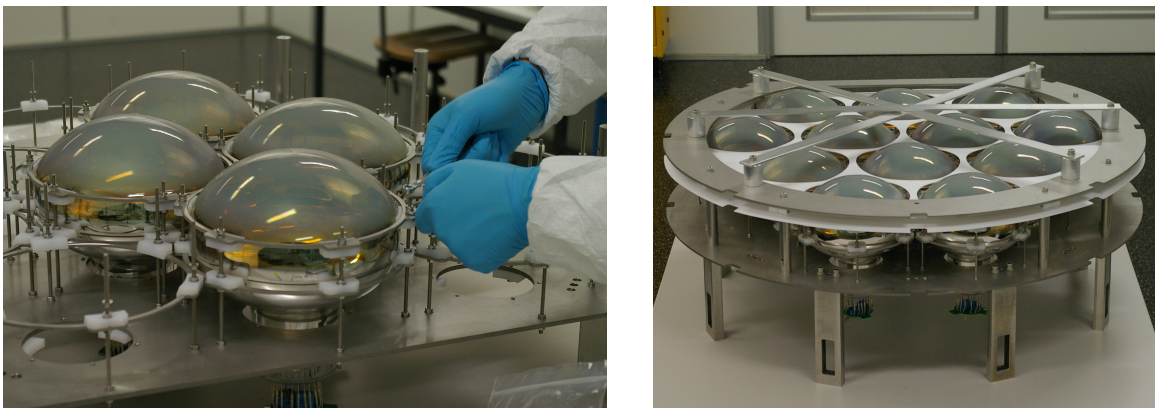

FIG. 47: The installation and final PMT array for the ArDM experiment [57, 92] in the ETHZ clean room. The aluminium crosses over the final array are only for protection during the transport to the Canfranc Underground Laboratory (LSC).

R&D program PMm2 [93, 94], for the instrumentation of giant water Cerenkov detectors with 12 inches photomultipliers. In the solution developed by this R&D, representing an important handle for costs reduction, the signals digitisation is performed by grouping the photomultipliers in arrays of 16. Each photomultipliers array is then read out by an ASIC (Application Specific Integrated Circuit) chip in AMS SiGe 0.35 μm technology. The ASIC, which is called PARISROC (Photomultiplier ARrray Integrated in Si-Ge Read Out Chip) [93, 95], provides a complete readout system for trigger-less acquisition. It integrates 16 independent and auto-triggered channels with adjustable gain (on 8 bits) and a high speed discriminator. The charge measurement is performed by a Wilkinson 10-bits ADC with a charge resolution of 0.2 photoelectrons and a dynamic range going from 1/3 of photoelectron to 600 photoelectrons (50 fC to 100 pC). The time measurement is based on coarse 24-bit gray counter running at 10 MHz (100 ns steps). This coarse measurement is then refined by adding a fine time measurement with an analog TDC on a 100 ns ramp, achieving about 600 ps resolution. Data are formatted by the ASIC and sent through network cables, which are water tight and include also the clock and slow control connections, to the external data storage. This contributes in appreciable savings in the connection cables and feedthroughs. The power consumption of the chip is 15 mW per channel.

A traditional digitisation scheme with one cable per photomultiplier and external fast digitisers could be easily setup for the LBNO prototype, however, in view of the large scale application for the final detector it is certainly worth to test this high-integration solution which may contribute in reducing the cabling connections and feedthroughs. The PARISROC ASIC can in principle work in liquid argon. An ongoing development foresees to test and adapt it for this application by possibly increasing the depth of the SCA and speeding up the digital readout section.

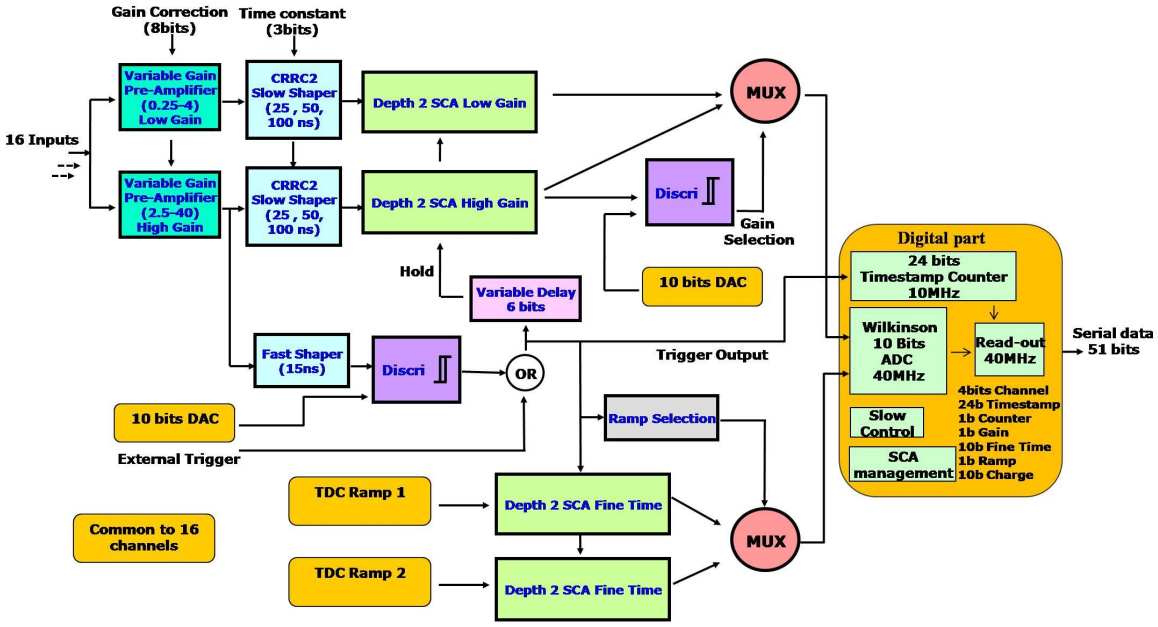

FIG. 48: PARISROC global schematic.

4.6 Cryogenic vessel

The inner vessel has a cubic shape with inner dimensions 8.3×8.3×8.3m^3. This volume ensures enough space surrounding the drift cage, acting as electric insulation (~1 m of LAr), for safe operation at HV with up to 300 kV at the cathode (and possibly up to 600 kV, to be tested as part of the demonstrator). This volume shall also be used for access and movement inside the vessel during the construction phase. A manhole and a detail-introduction hole are located at the top face of the vessel. During the inner detector assembly, additional chimneys are used to install a controlled air circulation (see Section **??**). These additional chimneys are available for the implementation of the liquid argon process during normal operation. The cryogenic vessel is built using technologies developed by the petro-chemical industry. This topic has been the subject of several developments between LAGUNA and industry over many years (since 2004). The so-called corrugate membrane panels technique (licensed by GTT/France), has been envisaged as an attractive solution for the LAGUNA LAr prototype. For practical reasons, we adopt the panels that come in standard sizes and shapes. A preliminary panel configuration, developed specifically for us by GTT, is shown in Figure 50. The membrane is 1.2mm thick stainless steel. The thermal insulation is passive, based on GRPF (glass reinforced polyurethane foam) layers, interspersed with pressure distributing layers of plywood. The pressure from the product is transmitted to a concrete envelope through polyurethane foam. Its thickness and composition is such to reach a residual heat input of 5 W/m^2 in cold operation. The

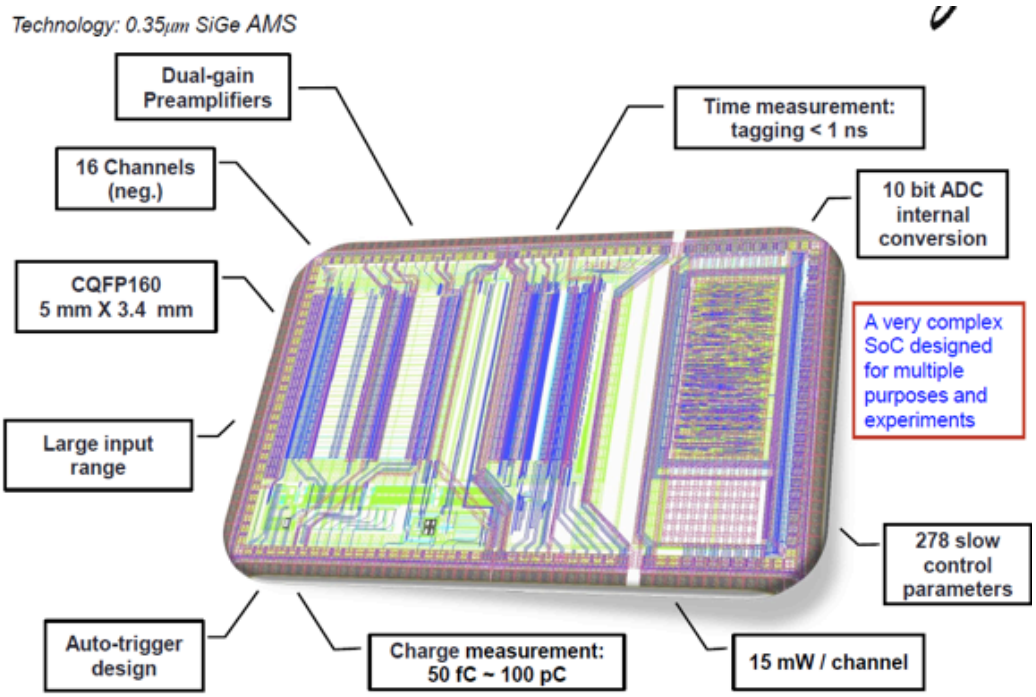

FIG. 49: PARISROC ASIC layout.

total heat input (including the input from the roof and the cables) in cold operation at LAr temperature is ~2 kW. The passive insulation is contained in a reinforced concrete "vessel" with ~0.5 m thick walls. The top outer ceiling is made by a framework reinforced stainless steel plane, able to support the inner anode and outer instrumentation (electronics, cryogenics, control). A beam pipe (evacuated) for the charged particles is crossing the concrete outer vessel and the thermal insulation layers. Its vertical orientation is adapted to the charged beam vertical axis in its last section. A top closed space ("penthouse") is constructed for hosting the electronic equipment, and various control and monitoring devices. A gap space shall remain between the reinforced concrete vessel and the walls of the pit. The airflow created by the ventilation and conditioning system of the hall will be sufficient to keep the temperature of the walls of the pit constant and avoid condensation on the walls.

4.7 Liquid Argon process

4.7.1 Effect of impurities on scintillation light

Electronegative impurities in the liquid argon do not only affect the lifetime of the free electrons but also quench the scintillation light, especially its slow component. In pure argon the total scintillation

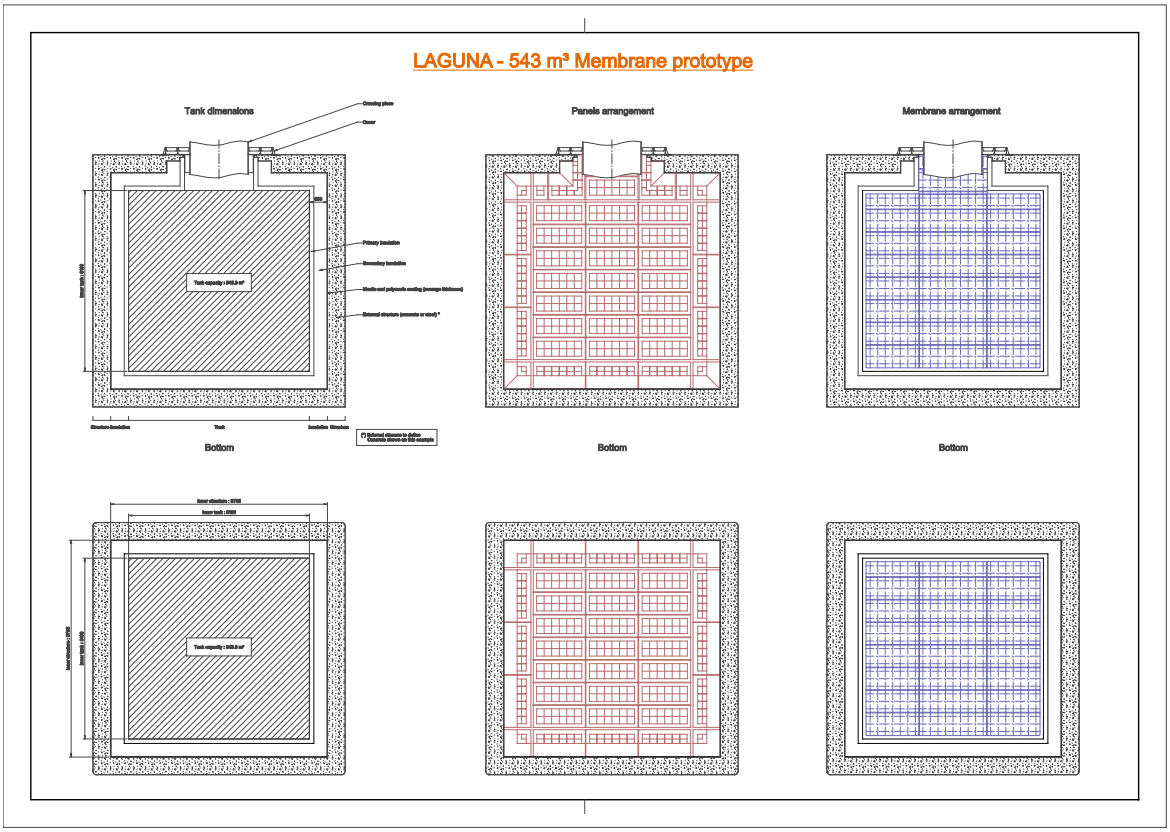

FIG. 50: Schematic of the 540 m^3 membrane vessel developed specifically for this proposal by GTT/France.

light emission rate $l(t)$ is given by the simple exponential equation

$$l(t) = \frac{A_S}{\tau_S} \exp\left(-\frac{t}{\tau_S}\right) + \frac{A_T}{\tau_T} \exp\left(-\frac{t}{\tau_T}\right), \tag{4.4}$$

with A_S the relative amplitude of the singlet and A_T the relative amplitude of the triplet state. The sum of the two is normalized to $A_S + A_T = 1$. In case of impurities, mainly O_2, N_2 and H_2O, the argon excimer $Ar_2^\star$ is de-excited by collisions with the impurity molecules and the average lifetime is therefore reduced [96].

$$\tau_T' = \frac{\tau_T}{1 + k[X_2]\tau_T} \tag{4.5}$$

with $k[X_2]$ the rate constant of the light quenching for different molecules X_2. The measured values for oxygen and nitrogen are $k[O_2] = 0.54 \pm 0.03\ \mu s^{-1} ppm^{-1}$ and $k[N_2] = 0.11\ \mu s^{-1} ppm^{-1}$ respectively [96]. Comparing the actual measured lifetime and the maximum lifetime of the triplet state of $\sim 1.6\ \mu s$, the purity of the liquid argon can be measured down to a contamination of $\sim 10 - 100$ ppb.

In the case of a detector that reads out charge and light, the quenching of the light is not important, since the purity needed for drifting large distances is the limiting factor. It is much lower than the

purity needed to recover all the light produced. For example, drifting over 1 m with an electric field of 1 kV/cm gives, according to Figure 15, a total drift time of ~ 500 μs and therefore, according to Equation (3.15) a maximum allowed O_2 equivalent contamination in the order of ~ 0.6 ppb. This is too small to affect the lifetime of the scintillation light. The light quenching is useful for quickly checking the quality of the commercial argon when delivered. It also gives an immediate alarm in case of a leak in the cryostat, since the lifetime can be analyzed in every PMT signal instantaneously without time consuming processing of the data.

4.7.2 Sources of impurities from outgassing

When pumping a volume from atmospheric pressure, the gas in the volume is removed whereas the speed of evacuation is mainly based on the speed of the vacuum pump. Down to a pressure of ~ 1 mbar, this is done with a roughing pump and at lower gas pressures, when the air resistance is low enough, with a turbo molecular pump. The pressure drops exponentially with the time as a function of the pumping speed S and the to be evacuated volume V:

$$p(t) \approx p_0 \, e^{-\frac{S\,t}{V}} \tag{4.6}$$

The gas flow while pumping can be assumed to be laminar. This behavior is true down to about 10^{-3} mbar, depending on the used pump. At lower pressures there is no longer any gas flow, but a molecular flow, since single molecules are removed. This is where the turbo molecular pumps become most efficient. In this pressure range, other effects, usually summarized as outgassing, become important. They are complex processes and different mechanisms at different pressure ranges and will be discussed in the following sections:

a) Zero order desorption

A first effect, after most of the gas in a volume is removed, is desorption from the surfaces. When there are multiple layers of material sticking to the surface, (e.g. there is water laying in the chamber) the desorption rate is constant. The rate with which molecules are desorbed depends on the latent heat of vaporization E_v and the temperature T [97]:

$$-\frac{dn}{dt} = \alpha \, e^{\frac{-E_v}{kT}} \tag{4.7}$$

where α is a constant depending on the initial pressure.

b) First order desorption

When coming to a monolayer of molecules sticking to the surface, the behavior changes. The desorption rate becomes time dependent, according to the molecular density on the surface. To a first approximation it can be assumed that particles are released from the surface, and do not return to it, with a rate proportional to their surface concentration C [98]. This process can be written as:

$$\frac{dC(t)}{dt} = -K_1 C(t) = \frac{e^{-E_d/N_A kT}}{\tau_0} C(t) \tag{4.8}$$

where the rate constant K_1, strongly depends on the activation energy of desorption E_d (per mol) and the temperature T. N_A is the Avogadro number and τ_0 the nominal vibration period of an adsorbed molecule; typically of the order of 10^{-13} s.

By integrating Equation (4.8) the surface concentration can be written as:

$$C(t) = C_0\, e^{-K_1 t} = C_0\, e^{-t/\tau_r} \tag{4.9}$$

where τ_r is the average time of a molecule sticking to the surface, i.e. the residence time of a molecule on the surface. It is, using Equation (4.8), given by

$$\tau_r = \frac{1}{K_1} = \tau_0\, e^{E_d/N_A kT} \tag{4.10}$$

c) Second order desorption

A lot of gas atoms are bound in a diatomic molecular state and they can only be desorbed as a molecule. For example, hydrogen bound to the surface first has to become an H_2 molecule before being able to be desorbed. This process, called second order desorption, is given by a different rate constant K_2 and the concentration can be written as [98]

$$\frac{dC(t)}{dt} = \frac{-K_2\, C_0^2}{(1 + C_0\, K_2\, t)^2} \tag{4.11}$$

K_2 depends on the desorption energy E_d and the temperature. Therefore, it is clear that second order desorption rate, proportional to $1/t^2$ is much smaller than the exponential decay of the first order desorption.

4.7.3 The desorption from real surfaces

In a real vessel, gas is not automatically pumped out when desorbed from the surface. A particle will bounce on the walls several times and can be re-adsorbed. With each re-adsorption, it sticks on average for the time τ_r to the surface before being desorbed again. This leads to an experimentally measured outgassing rate q of

$$q \propto \frac{1}{t^{\alpha}} \tag{4.12}$$

where α is a coefficient approximately equal to 1 [99]. This coefficient can be time dependent and varies with the composition of the outgassing components. In general the $1/t$ behavior is given for all molecules but for different kind of molecules the time constant of outgassing varies. Therefore, the total desorption is the sum of the desorption of the different molecules.

Since the residence time (Equation (4.10)) is a function of E_d and T, heating up the walls is increasing the speed of outgassing. For example, for water molecules sticking to a stainless steel surface, the desorption energy E_d is 23 kcal/mol = $96 \cdot 10^3$ J/mol and the residence time is 10^4 seconds at room temperature of 22 °C. Increasing the temperature of the chamber walls, gives a strong decrease of the residence time and for 350 °C it is about 10^{-5} s. It is therefore favorable to bake out the components and the inside walls of the vacuum chamber. But doing so, it has to be taken into account that all the chamber must be heated up and not only one part of it. As mentioned before a molecule released is most likely adsorbed again on another surface. Having now, for example, heated up half of the surface to 350 °C while keeping the other half at 22 °C gives an average residence time of $\frac{1}{2}(10^4 \text{ s} + 10^{-5} \text{ s}) \approx 5 \cdot 10^3$ s corresponding to an average temperature of 27.4 °C. This shows, that always the coldest surface is dictating the outgassing rate. Thus partial heating of one and later another part of the vessel is not having a significant impact on the overall performance of the vacuum.

4.7.4 Diffusion

At a certain pressure most residual gases on the surface of a chamber have been evacuated and diffusion is the major source of gas molecules. This is the transport of molecules inside materials. Gas molecules are moving from inside the detector parts and the walls of the cryostat to the surface where they desorb into the vacuum. Because diffusion is on a much slower time scale than desorption, the residence time for releasing the molecules from the surface can be neglected. The outgassing from

diffusion of a solid material for an initial gas concentration C_0 is

$$q = C_0 \left(\frac{D}{t}\right)^{1/2} \left[1 + 2\sum_{0}^{\infty} (-1)^n \exp\left(\frac{-n^2 d^2}{Dt}\right)\right] \tag{4.13}$$

where $[D] = \mathrm{m}^2/\mathrm{s}$ is the diffusion coefficient and $2d$ the thickness of the material. The gas concentration C_0 is given as residual pressure in Pascal and the diffusion rate q in $[q] = (\mathrm{Pa} \cdot \mathrm{m}^3)/(\mathrm{m}^2\,\mathrm{s})$ [98, 100].

Instead of solving this equation one has a look at its asymptotic solutions. For short times ($t \simeq 0$), only the first term is of importance and Equation (4.13) becomes approximately

$$q \approx C_0 \left(\frac{D}{t}\right)^{1/2} \tag{4.14}$$

This shows a decrease in the rate proportional to $t^{-1/2}$, which is much slower than the rate given by desorption. For long times, the infinite sum of Equation (4.13) has to be taken into account and, by a translation of the mathematical zero of the summation from the center of the volume, at distance d to one of the surfaces, Equation (4.13) reduces to a rapidly converging sum and becomes

$$q = \frac{2D\,C_0}{d} \exp\left(-\frac{\pi^2 D\,t}{4\,d^2}\right) \tag{4.15}$$

This change in slope is a result of the depletion of gas particles inside the outgassing material [98, 100]. The diffusion coefficient D not only depends on the diffusing gas and the material it diffuses from, but it is also a function of the thermal activation energy of the gas in the solid.

$$D = D_0\, e^{-E_D/kT} \tag{4.16}$$

Therefore, similar as for desorption, heating up the material leads to a much faster outgassing and is preferred.

4.7.5 Permeation

A surface facing the atmosphere is never completely depleted but also is adsorbing gas molecules of the atmosphere, which then diffuse through the material (walls) and get desorbed into the vacuum. The total motion can be described as an adsorption followed by diffusion and finally a desorption in the vacuum. Having a combination of the above described processes shows that the rate is much smaller than from the individual processes. This is called permeation. Because of the constant supply with new molecules form the atmosphere, permeation cannot be stopped. The only possibility to further reduce the pressure in a vessel is to seal the chamber wall on the outside with another, less permeable material

Material	Surface $[m^2]$	Outgassing rate @ t = 24 hr $[torr\,l/s\,cm^2]$	Total outgassing @ t = 24 hr $[mbar\,l/s]$	Reference
Steel	10.74	$2.00 \cdot 10^{-10}$	$2.86 \cdot 10^{-5}$	[102]
G10	5.60	$1.22 \cdot 10^{-7}$	$9.11 \cdot 10^{-3}$	[103]
Copper	1.25	$3.01 \cdot 10^{-11}$	$5.03 \cdot 10^{-7}$	[104]
Nylon	0.013	$2.50 \cdot 10^{-7}$	$4.20 \cdot 10^{-5}$	[105, 106]
Polyethylene	0.53	$6.00 \cdot 10^{-8}$	$4.25 \cdot 10^{-4}$	[107]
Kapton	0.30	$7.50 \cdot 10^{-8}$	$3.00 \cdot 10^{-4}$	[105]
Polyolefine	1.6	$5.25 \cdot 10^{-8}$	$1.12 \cdot 10^{-3}$	[108]
Teflon	0.02	$8.49 \cdot 10^{-9}$	$2.72 \cdot 10^{-6}$	[105]
Total outgassing after 1 day			$\mathbf{1.1 \cdot 10^{-2}}$	

TABLE V: Material and calculated outgassing rate of the 40×80 cm^2 LEM TPC, tested in the ArDM cryostate. All rates are given for t = 24 hr from the beginning of the evacuation.

or, more radically, change the chamber to one made of a different material or with thicker walls. For steel surfaces, hydrogen is the main element permeating through. The hydrogen molecule cannot permeate as a molecule but it dissociates on the metal surface into two single atoms that then diffuse through the metal. On the vacuum side of the steel wall the atoms have to recombine to a molecule to be desorbed. The permeation rate is proportional to the square root of the pressure difference [98]. Different from metals, in plastics, ceramics and glass the whole molecules can permeate through. For glass that is mainly the smallest existing molecule, the helium atom. This is of importance since photomultipliers are glass bulbs. Helium atoms diffusing into the tubes ionize in the strong electric field and destroy the photocathode. For this reason, leak testing a chamber, containing PMTs, with a helium leak tester should be omitted. Note, that permeation is only observed in ultra high vacuum chambers and was never observed in tests performed in smaller LAr TPC by the ETHZ group.

4.7.6 The ETHZ 40×80 cm^2 LEM TPC as an example

To give a practical example, the test of the 40×80 cm^2 LEM TPC is considered [39, 101]. The detector is mainly made from glass epoxy boards (G10). This material has a lot of epoxy resin and therefore solvents in it and a strong outgassing must be expected. Besides the actual detector, there are also cables, electronic components and the support system for hanging the setup inside the ArDM cryostat. All these components are outgassing and possible sources of impurities. Table V gives an overview of the material budget and the corresponding surface areas. The table also gives an expected outgassing rate per square meter after 24 hours of pumping, derived from several sources. These rates are average values to get a feeling, what is contributing how much to the outgassing. If there were several values given for the same material, an average has been taken, normalised to 24 hours by assuming an outgassing rate of $R(t) \propto 1/t$.

To test our model, outgassing measurements were taken several times during the pumping of the volume. The overall pumping time was around 65 days. Figure 51 shows the pressure inside the cryostat as a function of the days since pumping started. The curve is not smooth but has several spikes, above as also below the actual pressure curve.

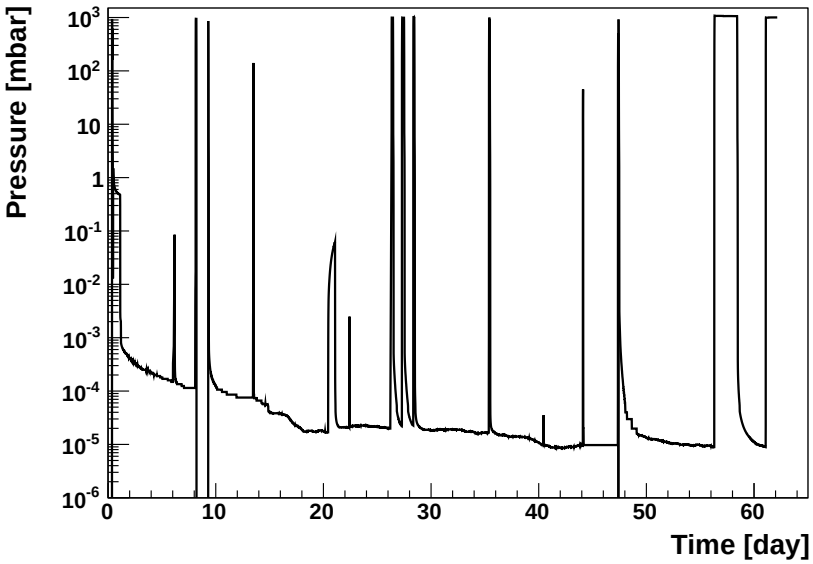

FIG. 51: The pressure as a function of the evacuation time for the 40×80 cm^2 LEM TPC. The pumping started on August 10, 2011 and lasted for 62 days, before starting to fill the detector with argon. The peaks in the curve are coming from tests with pure argon gas and also from venting the vessel. (See text for details)

Values below 10^{-6} mbar are indicating the times when the vacuum gauge was switched off and the spikes above the smooth curve have different origins. There are, for example at ~ 6 days and at ~ 20 days, measurements of the outgassing with the Rate-Of-Rise method. Other spikes, when reaching more than 1 mbar, are from moments when the detector was filled with argon gas for calibrating the PMTs or to do tests with the charge readout. Also, the cryostat was filled with argon gas when a flange or other components on the top flange had to be replaced. At ~ 48 days the detector was completely opened again for a few hours, because of a problem with an electrical contact. It can be seen that it took a while to reach the previous vacuum again because of newly installed PCB parts. In the few hours while the detector was exposed to air some water molecules attached to the detector but the main reason for the slow reaching of the previous vacuum value is presumably the water (and other residual gases) in the new glass epoxy parts.

The reason for showing Figure 51 in the context of outgassing rates is, that every time the detector is filled with gas, there is a short period of a few minutes when the gate valve to the pump is closed but still there is no gas filled in the detector. During these periods the detector is outgassing and, analyzing the outgassing with the Rate-Of-Rise method, the rate as a function of the time can be measured.

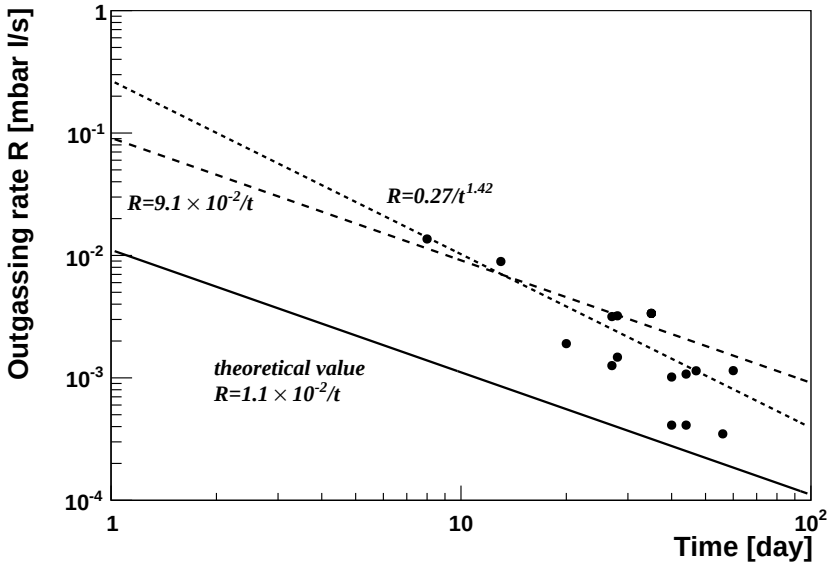

FIG. 52: The outgassing of the 40×80 cm^2 LEM TPC as a function of the pumping time. The full line indicates the calculated value from Table V and the two dashed lines the fit functions for the measured data.

The values obtained are presented in Figure 52. Also the calculated value of 1.1×10^{-2} mbar l/s, from Table V, is drawn (full line), assuming a simple $1/t$ law. The dashed lines are a fit, strictly proportional to $1/t$ as also to a general power law, giving $R = 0.27/t^{1.42}$ with $[t]$ = hr and $[R]$ = mbar l/s. The theoretical outgassing rate and the measured outgassing rate are different by about one order of magnitude. The actual outgassing is faster than $1/t$. A possible explanation is that, when filling the chamber with argon to atmospheric pressure, water, that is frozen at low pressures, re-liquifies and gets dissolved in the gas. This effect can be seen in Figure 51 at about 14 days. After a short period of venting the chamber with argon gas, the pressure drops faster, when the pumps are turned on again, compared to the rate before the venting.

4.7.7 Leaks

Eventually, the outgassing becomes so small that permeation is the main source of impurities. This is the point, where there is no way to improve the vacuum without changing to a bigger, more powerful pump. It is hardly reached with a normal turbo pump and other methods, e.g. using getter pumps, have to be applied. Permeation only gets notable at pressures below 1×10^{-8} mbar. Because of its time independence, the best vacuum reached is

$$p = \frac{Q_{permeation}}{S} \tag{4.17}$$

here S is the pumping speed.

If this absolute possible vacuum is never reached and the pressure becomes constant, this is an indication for a leak. Leaks behave similar to permeation. Also they are letting a constant, time independent, flux of gas into the vacuum. The leak rate, therefore, is given, similar to Equation (4.17) by

$$Q_{leak} = \frac{\Delta p \cdot V}{\Delta t} = p_{min} \cdot S \tag{4.18}$$

where p_{min} is the pressure at the best vacuum obtained. $[Q_{leak}]$ = mbar l/s the leak rate of the biggest leak. In general each leak has a different "size" and therefore the largest has most influence on the final pressure and it is the one to be found first.) Fixing smaller ones will not make any major effect and cannot be noted by looking at the pressure. After the main leak is found, the next smaller is the leading one to be fixed.

Permanent leaks are actual holes or cracks in the structure, where gas molecules can pass through. Most of the time they occur on connections, where two vacuum parts are flanged together. More rarely they happen to be from production errors like weldings that are not done properly. A third, very critical place, are connections of different materials like for example feed-throughs. In this case there is a material boundary between the stainless steel flange and the insulator and again between insulator and conductor. The vacuum tightness is done with glue, a soft metal like indium or by mechanical force, just pressing together the two parts. This kind of leaks sometimes can be cured by having a very liquid epoxy resin. Having vacuum on one side the epoxy can be put on the insulator and, through the leak it is sucked in and blocks the channel where the molecules went in.

Temporary leaks open and close, under certain conditions. Most of the time a temperature effect is the reason. Having the large gradients form room temperature to cryogenic temperatures in ArDM, the contraction of different materials becomes important. Normally plastics have a thermal contraction of a few percent for a ΔT of ~ 200 °C. Metals on the other hand contract about ten times less. The connection between two different materials can be tight at room temperature but by cooling it down it becomes leaky. Figure 53 shows the correlation between the pressure in the vacuum insulation of ArDM (described later in **??**) and the temperature of tubes containing the argon inside it. In the beginning the normal behavior of evacuation is visible. With the start of cooling down the detector, at T ~ 2 days, the vacuum improves because of the cold surfaces. Later, it goes back on its original curve with a lot of fluctuations, which already indicates the release of a gas from a leaky connection. When cooling down more, to ~ 100 K, the leak seems to close again and the pressure drops again. At T = 10 days liquid was filled in the cryostat (what can be seen by the sudden temperature drop to 89 K). In exactly the same moment, the pressure is rising what is a clear indication for a cold leak. This

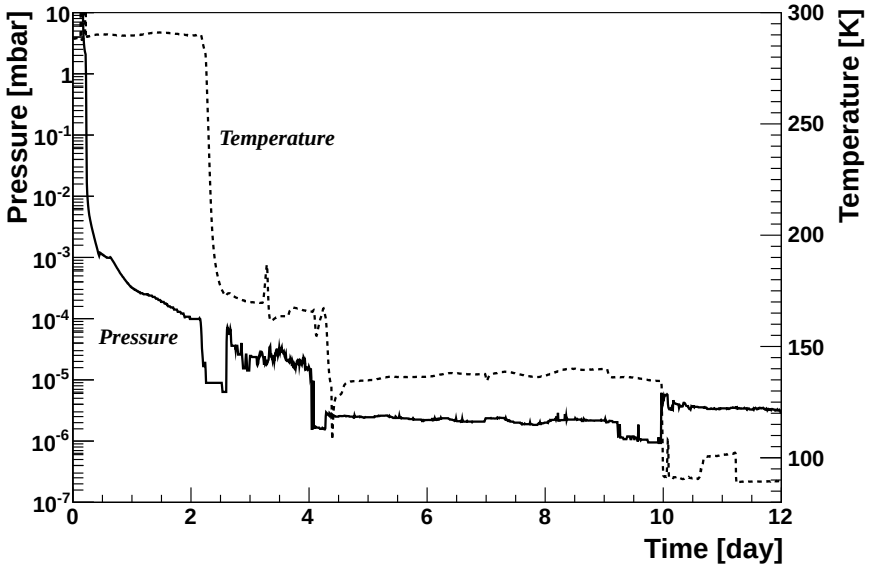

FIG. 53: The correlation between the pressure of the vacuum insulation (full line) and the temperature of a cold line inside it (dotted line) shows the behavior of cold leaks. Most obvious is it at T = 10 days where a temperature drop from gaseous to liquid argon immediately gives an increase in the pressure.

example shows that the cold temperature created a small leak in one of the joints that only opens when the temperature falls below 150 K.

4.7.8 Gas recirculation

The best way to reduce the amount of impurities is to pump the cryostat for a reasonably long time, if possible for several months, before filling with argon. But even after a long evacuation phase there is outgassing. After stopping of the pump the impurities can diffuse into the volume without being pumped away. The argon has to be purified constantly. To make an example, taking the lowest value for outgassing of 3.4×10^{-4} mbar l/s from Figure 52 and the total volume of 1700 l of the system, with a total pressure at the moment when the gate valve is being closed of $\sim 2 \times 10^{-7}$ mbar. 15 minutes later, it is only $\sim 1.8 \times 10^{-4}$ mbar, which corresponds to 180 ppb of impurities when assuming the volume filled with 1 bar of argon gas at room temperature.

One possibility to slow down the outgassing process is to cool down the vessel while still pumping it. The time $t(T)$ for the outgassing of stainless steel at temperature T can be found by fitting the values given in [100], with an exponential function:

$$t(T) = \alpha \cdot e^{-0.0164 \cdot T} \tag{4.19}$$

The 15 minutes at 300 K therefore become $\sim$ 400 min at 100 K. Further, the cold gas is 3 times more

dense than the argon at room temperature. Therefore, filling with pure argon and cooling it to ~ 100 K, reduces the ratio of impurities by a factor 3 compared to warm argon gas. When filling with pure liquid argon, it is reduced even by a factor of ~ 800 with respect to argon gas at 20 °C.

This example shows that an initial cool down, with vacuum inside the chamber has a positive effect on the concentration of impurities diffused into the volume as also the ratio is improved. The disadvantage is, that all molecules that did not desorb are still on the surfaces and eventually some are dissolved in the liquid. A constant recirculation and purification of the liquid is needed.

Another approach is, to actually fill the chamber with pure argon gas, while it is still warm. The outgassing in the gas is large but, contrary to cryogenic liquids, purification of the warm gas is not difficult and commercial cartridges can be used. Having a given gas flow S ($[S] = \mathrm{l/s}$) and an outgassing rate R ($[R] = \mathrm{mbar\,l/s}$) the total amount of impurities $N(t)$ as a function of time can be estimated by the following idea:

The change of impurities is given by

$$\frac{dN(t)}{dt} = \frac{dN_{in}(t)}{dt} - \frac{dN_{out}(t)}{dt} \tag{4.20}$$

Where the total outgassing rate can be assumed to be constant and the total molecules outgassing into the vessel is given by

$$N_{in} = N_0 + \frac{R}{k \cdot T} \cdot t \tag{4.21}$$

with N_0 being the number of molecules still inside the volume after pumping. They are given by the general gas equation

$$N_0 = \frac{p \cdot V_{tot}}{k \cdot T} \tag{4.22}$$

with p the pressure before closing the gate valve. The differential outgassing rate into the vessel is given by

$$\frac{dN_{in}}{dt} = \frac{R}{k \cdot T} \tag{4.23}$$

The change of impurities filtered out depends on the pump speed and the total impurity concentration inside the vessel. It is given by

$$\frac{N_{out}}{dt} = \frac{S}{V_{tot}} \cdot N(t) \tag{4.24}$$

where the efficiency of the filter has been assumed to be 100%, i.e. all impurities passing through it are filtered out.

Combining the two parts leads to the following differential equation:

$$\frac{N}{dt} = \frac{R}{k \cdot T} - \frac{S}{V_{tot}} \cdot N(t) = A - B \cdot N(t) \tag{4.25}$$

and solved to

$$N(t) = \frac{A}{B} + C \cdot e^{-B \cdot t} = \frac{R \cdot V_{tot}}{k \cdot T \cdot S} + C e^{-\frac{St}{V_{tot}}} \tag{4.26}$$

The constant C depends on the initial amount of impurities N_0 in the vessel.

Taking a total volume $V_{tot} = 1700$ l for the dewar, an outgassing rate of $R = 3.4 \cdot 10^{-4}$ mbar l/s and an actual gas flow of $S = 80$ l/min for the gas recirculation, the equilibrium is reached when the rate of impurities, that can be trapped, is equal to the rate of new impurities produced by outgassing, i.e. $N(t \to \infty)$ in Equation (4.26):

$$\begin{aligned} N &= \frac{R}{k \cdot T} \cdot \frac{V_{tot}}{S} \\ &= \frac{3.4 \cdot 10^{-4} \text{ mbar l/s}}{k \cdot 297 \text{ K}} \cdot \frac{1700 \text{ l}}{80 \text{ l/min}} = 1.05 \cdot 10^{19} \text{ particles} \\ &= \sim 255 \text{ ppb @ SATP} \end{aligned} \tag{4.27}$$

Using Equation (4.26) the contamination of the argon gas with impurities (in ppb) is plotted as a function of time in Figure 54. For comparison, there is the actual gas flow of the ArDM system of 80 l/min as also an increased gas flow of 200 l/min shown. Analyzing these curves shows that it is most important to reduce the outgassing rate as much as possible. Once stopping to pump pollutes the volume in a few minutes with more than 100 ppb of impurities. Also it can be seen that the maximum contamination with impurities is given by the gas flow through the filter and not the initially reached vacuum.

4.7.9 Liquid argon purification

The initial purity of commercial liquid argon is in the order of ppm of oxygen equivalent impurities. It is not sufficiently clean for the experiment and has to be purified in situ. Different techniques, hereafter discussed, are used to filter out different molecules.

For large setups evacuation is not possible and the majority of the air inside the dewar is removed by flushing the setup with argon gas. A big help is that argon (40 g/mol) is heavier than the other

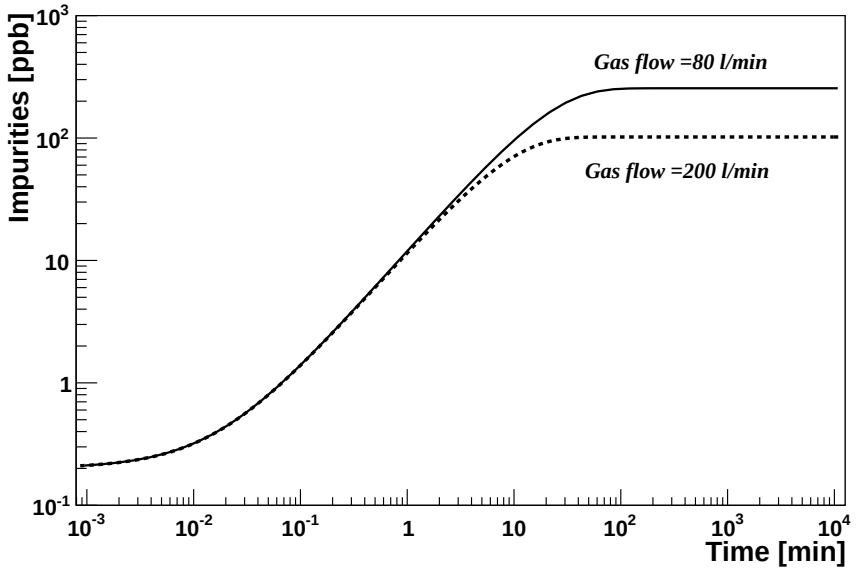

FIG. 54: The contamination of the argon gas at SATP conditions with impurities as a function of the time, from the moment on when the gate valve has been closed and pure argon gas was filled in the system. The curve is calculated according to Equation (4.26) for the values discussed in the text for the 40×80 cm^2 LEM TPC in the ArDM dewar.

molecules like O_2 (16 g/mol), N_2 (14 g/mol) and H_2O (10 g/mol). Filling up a volume with argon presses out the other gases and after a few exchanges of the whole volume the contamination in a vessel can be reduced to the level of ppm, equivalent to the initial purity of the liquid argon. An example for a large, non evacuable volume is a dewar of about 6 m^3. After ten volume exchanges the oxygen concentration was measured to be ~ 4 ppm [109].

Having reached the initial purity of the liquid argon, the only way of improvement is to actually purify the argon. Depending on the kind of molecule to be removed different filters are used. Also an important role plays the argon state in which the purification takes place, i.e. whether the argon is purified as gas or liquid. In general impurities in the liquid argon are filtered out by binding them to a surface. This can be a cold trap (freezing impurities to a cold surface), physical adsorption (van der Waals force) or chemical adsorption (reaction with other atoms).

4.7.10 Molecular sieve

For filtering out water molecules, in general physical adsorption is used. This can be silica gel, aluminum oxide or a molecular sieve. While the silica gel has the biggest capacity for holding back water, the molecular sieves are the strongest adsorbents. In general the power of adsorption is given at the temperature of the dew-point. For silica gel it is ~ -5 °C and for a molecular sieve up to ~ -100 °C [110]. Assuming a vapor pressure of 1×10^{-4} mbar for water at -100 °C, this gives a ratio of ~ 100 ppb for gaseous argon at room temperature and ~ 0.1 ppb of water for liquid argon. This increase in purity

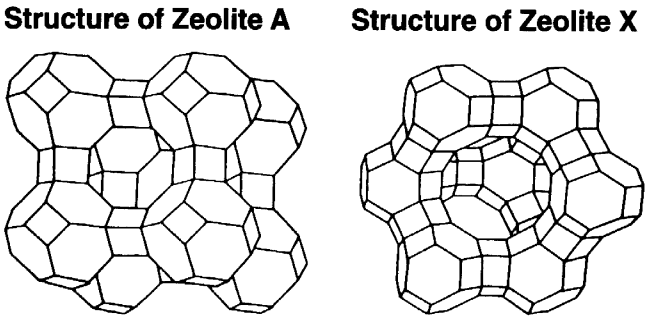

FIG. 55: Molecular structure of the two most common types of zeolites. The pore size in the center depends on the element with which some of the sodium atoms are replaced. It is between ~ 3 Å and ~ 5 Å in diameter for type A and ~ 10 Å for type X.

for liquid is due to the 800 times higher density of argon atoms in liquid compared the gas/vapor at room temperature. For the water molecules there is no such increase assumed since the amount is given by the partial pressure of 10^{-4} mbar and independent of the other molecules in the mixture.

Usually a molecular sieve consists of porous aluminosilicates, so called zeolites. They are able to adsorb water and when heated up to release it. For commercial use these kind of crystals are synthetically produced and specially designed to have a uniform and precisely defined pore size. Figure 55 shows the crystalline structure of the two most common types of zeolite. Each "ball" of the structure (in the Zeolite A structure in the eight corners) has a silicon or an aluminum atom in each corner of the square surfaces, interconnected with oxygen atoms. Because the aluminum atom is trivalent the structure as a whole becomes an anion. To become electrically inert there are sodium, calcium or potassium cations attached to the molecule. Depending on the ratio and the type of these exchangeable cations the properties of the molecule can be influenced.

A crystal with sodium atoms has a pore size of ~ 4 Å, while replacing a sodium atom with a potassium atom shrinks the diameter to ~ 3 Å. Replacing it with a calcium atom increases the diameter to ~ 5 Å. In such a crystal, molecules smaller than the diameter of the pore can enter, larger ones are blocked. Capillary condensation takes place with the molecules entering to a much larger scale than to others since most of the surface of the crystal is inside the structure. So molecules, smaller than a certain size can be attached, while larger ones flow around the crystal. Considering only this property, also the argon atoms should be filtered out and the sieve immediately would saturate. This is not the case since, besides the capillary condensation, there is a second effect The polarity of the sieve material makes molecules stick to the surface. Because of the crystal structure made out of electrically unbalanced charged parts at fixed positions, the crystal has a polar surface. Therefore, polar molecules like water are attracted and stick to the surface while apolar molecules only are held very weakly. The attachment of argon and nitrogen atoms, can be found in [111]. With this property water can

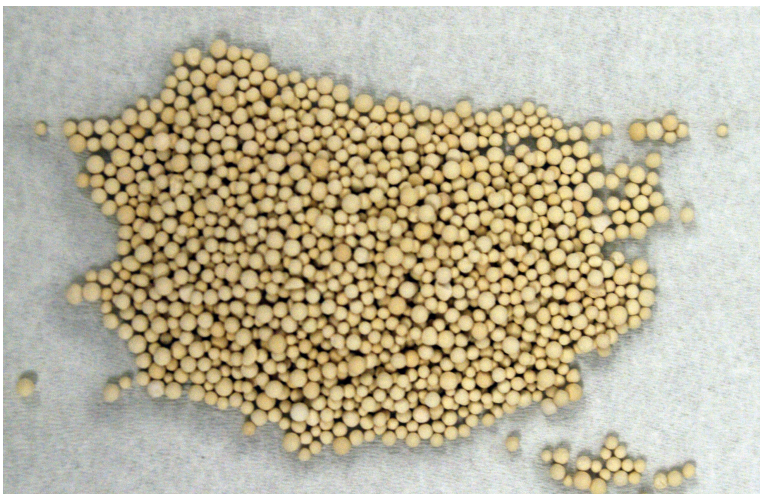

FIG. 56: Molecular sieve *ZEOCHEM 3A*© grains before inserting them in the regeneration cartridge. Each grain has a diameter of about 2 mm.

be trapped up to ~ 28% of the crystal weight and these kind of crystals really act as a "sieve" for filtering out certain molecules. The amount of trapped molecules depends on the temperature of the crystal since at higher temperature molecules are easier detached again. This behavior is also used to regenerate the material. By heating it up to ~ 250 °C and flushing it with dry nitrogen/argon gas the trapped water is released and the zeolite can be used again.

Commercially, there are different molecular sieves available, depending on the diameter of the pore, they are called 3A, 4A or 5A, where "A" stands for Angstrom. Zeolites of type X in general have bigger pores of about 10 Å.

In ArDM, a molecular sieve is not included in the standard recirculation circuit. Water is removed as much as possible from the detector by evacuating the volume for a long period before filling with argon. The remaining water, if attached to a surface, is sticking to it very strongly due to the low temperatures. If it is dissolved in the liquid argon, it (partly) sticks to the oxygen filter described in Section 4.7.11. Therefore, the only way for water to enter the detector volume is to be already dissolved in the liquid argon, used for filling the detector. For this reason a purification cartridge, partly filled with a 3A molecular sieve is placed before the inlet to the detector. It is filtering out the water from the commercial liquid argon. Figure 56 shows the 3A crystals with a diameter of ~ 2 mm each. In total the cartridge contains 0.7 l of molecular sieve.

4.7.11 Oxygen filters

As mentioned before, the most critical impurity for drifting electrons in liquid argon is oxygen. A constant recirculation and purification of the argon is mandatory to keep the contamination low. Oxygen is entering the detector volume through micro leaks in the detector shell or, more dramatically,

through cold leaks, discussed in Section 4.7.7. Also not to be neglected is the outgassing of the detector material. By evacuating the detector, a lot of the residual gases are pumped out but, by lowering the partial pressure of the vessel, impurities might condense or freeze and can no longer be pumped. Breaking the vacuum with pure argon gas and re-pumping it helps to reduce them.

For filtering out oxygen from argon gas or liquid, chemical adsorption is used. More specifically, the argon oxygen mixture is guided over a surface of a reduced material. It oxidizes and only argon is left. The challenge is to find a material with a low reaction potential for an efficient oxidation and a large surface. Elements in question are easy to be oxidized metals. We have successfully developed filters containing pure copper powder. Oxidation is an exothermal reaction and takes place according to

$$\mathrm{Ar} + \mathrm{O_2} + 2\,\mathrm{Cu} \rightarrow \mathrm{Ar} + 2\,\mathrm{CuO} \tag{4.28}$$

The heat of adsorption is ~ 82 kcal/mole on the true oxidation and goes down to ~ 55 kcal/mole for the partly oxidized copper grains [112]. This reaction is a surface process and takes place in a monolayer of the copper. In fact the thickness of the layer is increasing with the temperature. At 87 K it is ~ 4 Å while at 300 K it is ~ 17 Å [113]. Since the temperature is given by the liquid argon, it is important to have a maximum possible surface per volume. It can be reached by the use of sintered copper pellets[136]. Each grain of copper has a diameter of a few 10 μm. It is not a single junk of copper but sintered together from smaller grains in the nanometer scale. Figure 57 shows an image of such a grain taken with an electron microscope. Because of its exothermal reaction with oxygen, copper is sold already oxidized to copper(II)oxide (CuO), not to be confused with copper(I)oxide ($\mathrm{Cu_2O}$).

Before being used as a filter it has to be regenerated. This happens by another exothermal reaction where the copper(II)oxide is flushed with hydrogen. The oxide is reduced to pure copper and water according to

$$\mathrm{CuO} + \mathrm{H_2} \rightarrow \mathrm{Cu} + \mathrm{H_2O} \tag{4.29}$$

Since the reaction is exothermal, the temperature has to be monitored by measuring the temperature of the exhaust gas from the cartridge in oder not to harm the pellets. The temperature is controlled by the amount of hydrogen entering the cartridge. To initiate the reaction, a temperature of ~ 150 °C of the copper(II)oxide is needed, which is achieved with heating bands wound around the purification cartridge. By the reaction the temperature rises and, as a clear indication of a complete regeneration, the temperature drops back to the value of the heater. Another indication for the cartridge to be

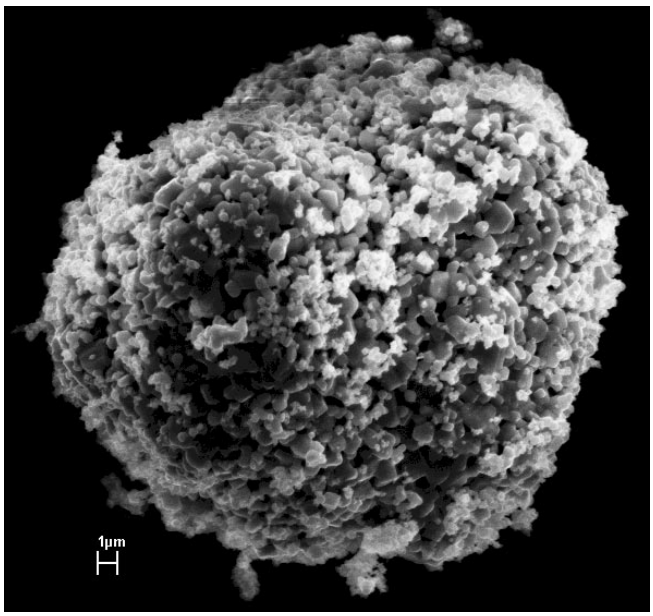

FIG. 57: The copper grains, sintered together from smaller grains, have a diameter of a few 10 μm. This technique grants a large ratio of surface to volume.

FIG. 58: Collected water from regeneration of a copper cartridge.

regenerated is to see how much water is extracted from the cartridge by cooling the output gas. The water condenses and can be measured as seen in Figure 58.

Hydrogen is a dangerous gas and the concentration must stay below 3% in order not to take the risk of an explosion. For this reason the regeneration does not take place with pure hydrogen but with a mixture of hydrogen and argon. Also at the end, when the copper is regenerated, the cartridge

is flushed with pure argon gas, at ~ 150 °C, to clean out all the water vapor trapped in the sintered material. For transporting and storing, the regenerated cartridge is filled with pure argon gas to an overpressure of ~ 0.5 bar.

4.7.12 Concept for the gas and liquid purification of the $6 \times 6 \times 6$ m^3 prototype

The liquid argon process and the performance of its sub-units are a critical item for the successful operation of the $6 \times 6 \times 6$m^3 prototype. The basic parameters are summarised in Table VI. The inner-

TABLE VI: Overview of the parameters for the liquid argon process

General properties	
Total inner-vessel volume	$600\,\mathrm{m}^3$
Membrane surface in inner-vessel	$430\,\mathrm{m}^2$
Liquid level above floor	$7\,\mathrm{m}$
Amount of liquid	$\approx 530\,\mathrm{m}^3$
Amount of gas	$\approx 70\,\mathrm{m}^3$
Instrumented volume	$6 \times 6 \times 6\,\mathrm{m}^3 = 216\,\mathrm{m}^3$
Gas purification	
With 2 pumps of 500 l/min each	$\approx 10\,\mathrm{hr}$/vol. for warm gas (300 K) $\approx 30\,\mathrm{hr}$/vol. for cold gas (100 K)
Boil-off	
Heat input (vessel)	$2150\,\mathrm{W}$ ($5\,\mathrm{W/m}^2$)
Evaporation rate	$450\,\mathrm{l_{gas}/min}$
Liquid purification	
Purification speed for $\tau = 1\,\mathrm{day}$	$22\,\mathrm{m}^3/\mathrm{hr} \approx 400\,\mathrm{l/min}$

vessel volume which contains all equipment and the argon is about 600 m^3. It must be a totally sealed volume with no leaks towards the outside in order to avoid the penetration of any contaminant or the loss of pure argon.

During construction and assembly phase, the inner-vessel volume will be maintained in a controlled air environment. Starting from that state, the volume will be first replaced with argon. In [71] we have experimentally demonstrated on a volume of 6 m^3 that the replacement of air with argon gas down to ppm impurities concentration is achievable through flushing.

4.8 Process control and monitoring

The main function of the process control and monitoring system is the monitoring of the condition of the prototype and the regulation of the cryogenics and high voltage systems in order to allow a safe operation of the detector. In addition, the control system is a safety monitor that alerts people in case of an imminent danger, such as oxygen deficiency or fire. The control system allows for process control

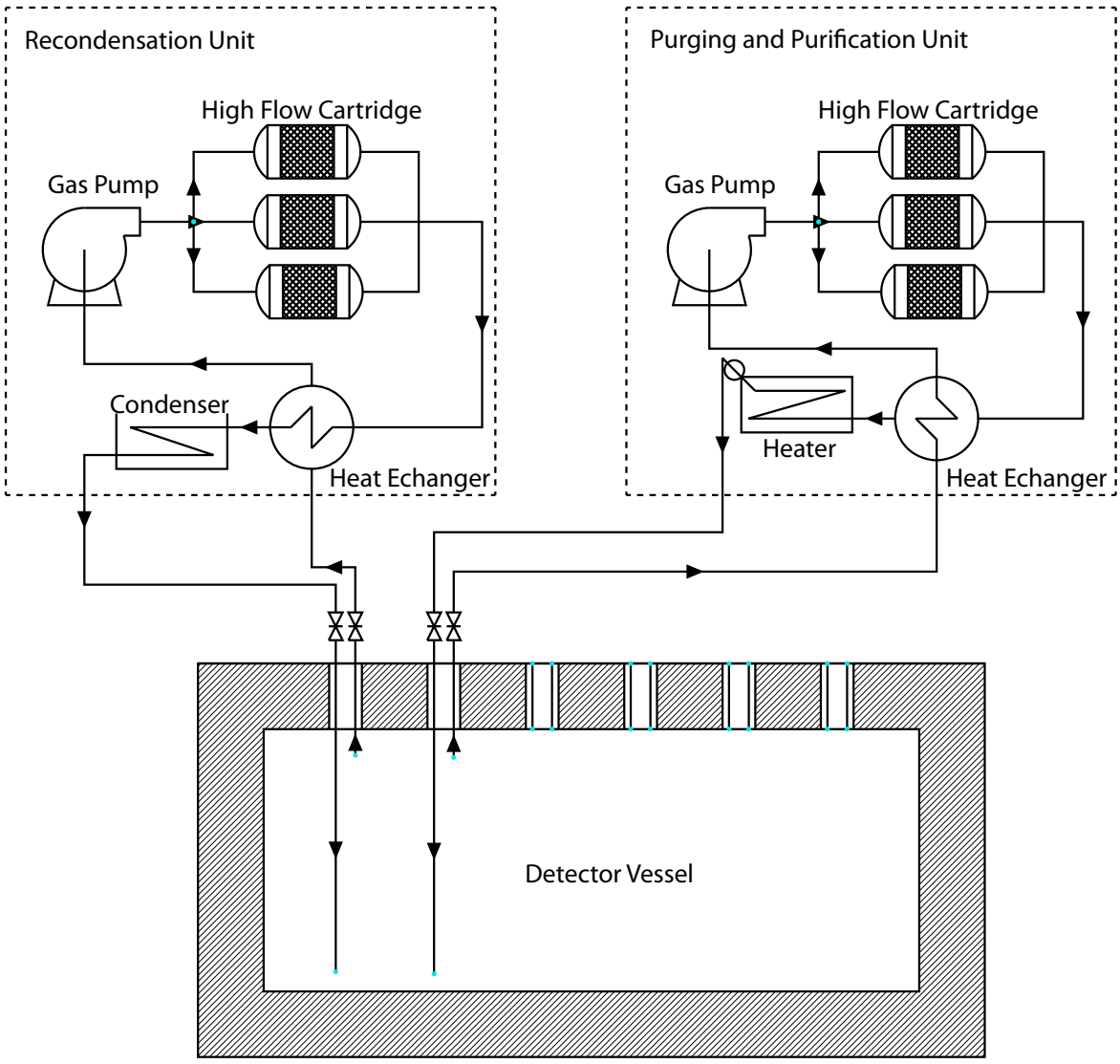

FIG. 59: Schematic diagram for the gas recirculation system.

and is based on a programmable logic controller (PLC). A PLC is a computer specially designed for process automation with a large number of inputs and outputs for sensors and actuators. PLCs possess a high reliability due to specialised hard- and software and therefore the control system serves as a safety system.

The control system developed for the ArDM (RE18) experiment built in Collaboration with the CERN/PH-DT group, is shown in Figure 62. The control system for ArDM is located in seven standard 19 racks next to the detector together with the high voltage supply for the PMTs (HV rack in Figure 62) and the data acquisition system (DAQ rack in Figure 62). The PLC modules are installed in the PLC1 and PLC2 racks. The processor module and the analog input and output modules are in the PLC1 rack, the digital input and output modules are in the PLC2 rack. The INT1 and INT2 racks contain the interfaces for the sensors and actuators and displays for pressure and vacuum sensors whereas

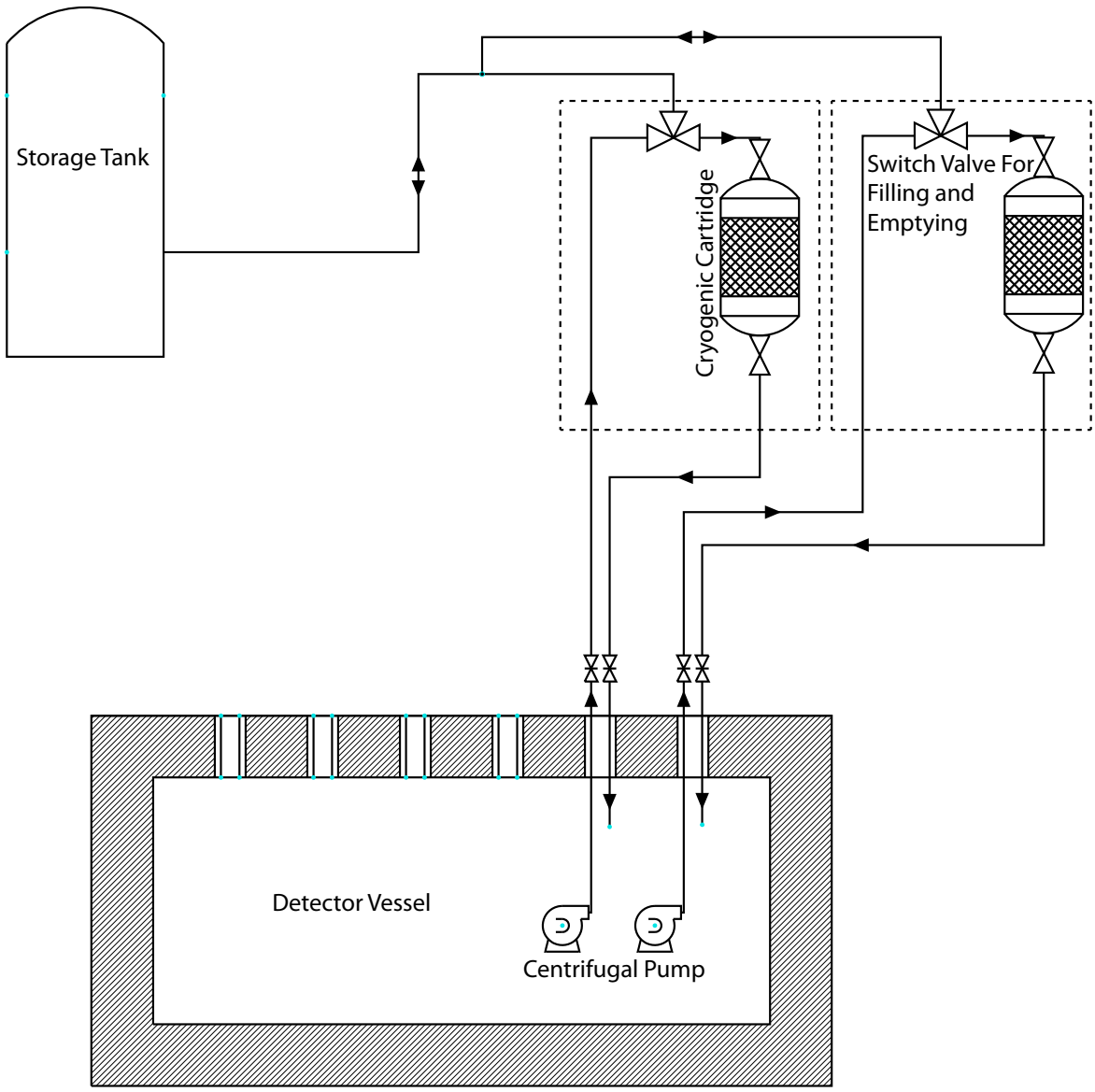

FIG. 60: Schematic diagram for the liquid phase purification system.

the COM rack contains the supervisory computer and its accessories. For safety reasons every rack contains its own power distribution unit that provides the power for the entire rack and allows to cut the power of the complete rack with one single circuit breaker. The main power line of ArDM (three-phase, 400 V, 80 A per phase) arrives to the power distribution unit in the INT1 rack. From there all the power distribution units in the other racks, with the exception of the PLC1 and PLC2 racks, are supplied with single-phase current (230 V, 20 A). The PLC1 and PLC2 racks are supplied with 24 VDC which are delivered by a rectifier in the COM rack. Also all the sensors and actuators installed in the ArDM experiment are powered from the racks of the control system. To protect the control system from short power cuts, all the equipment, with exception of the devices supplied by the INT1 rack, are connected to two UPSs (uninterruptible power supplies), UPS 12 and UPS 23 , with a

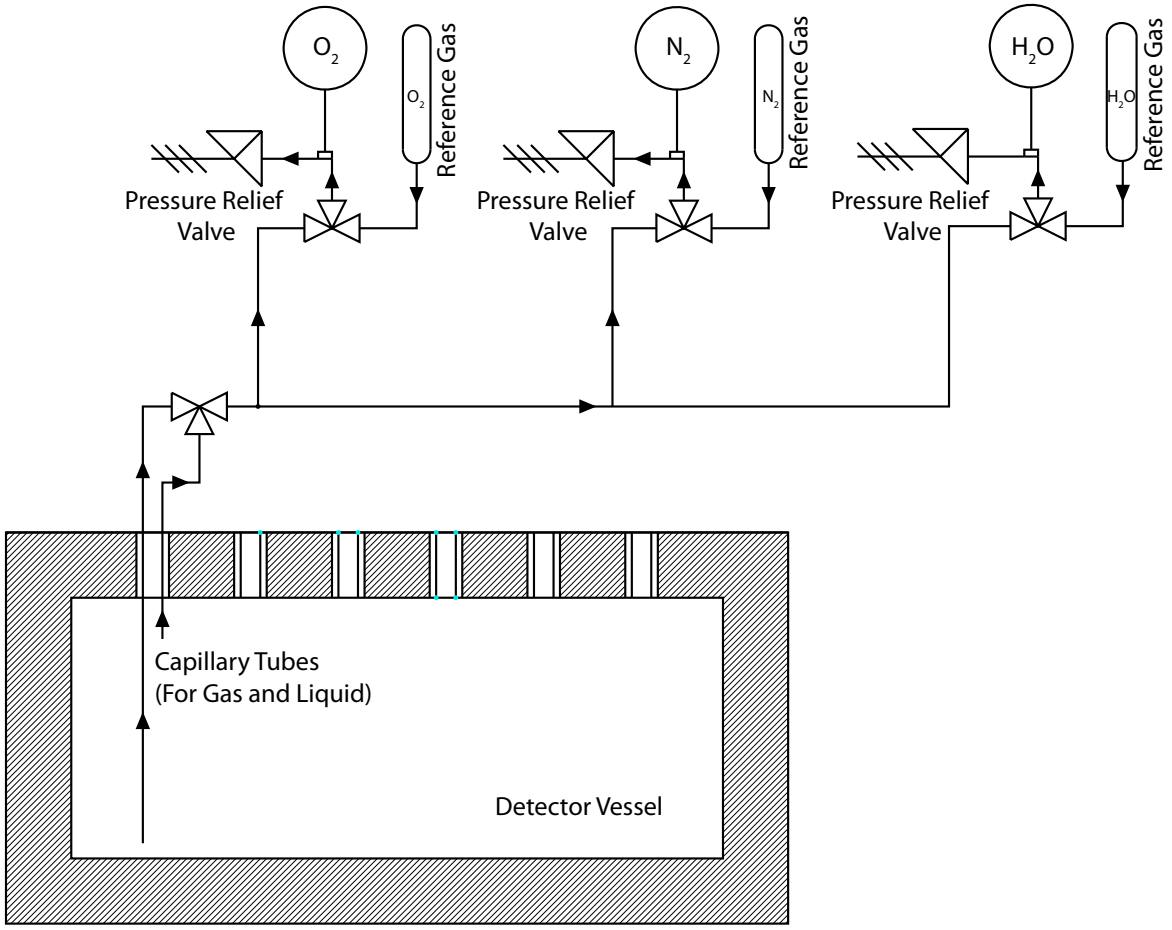

FIG. 61: Schematic diagram for the liquid and gas phase impurity analyser systems.

total power of 6300 W. The two UPSs can cover the power consumption of the connected equipment for about 15 min. In case of a power cut, the UPS 1 supplies the equipment in the INT2, the DAQ and the HV rack, the UPS 2 supplies the COM rack and thus also the PLC1 and PLC2 racks. The control software is based on PVSS (Prozessvisualisierungs- und Steuerungssystem, process visualisation and control system) used by CERN.

Although larger in scale, we expect that the process control and monitoring system for the $6\times6\times6\text{m}^3$ prototype will be functionally very similar to the one developed and successfully operated for ArDM. We therefore expect that it will be rather straight-forward to develop and implement a new dedicated process control and monitoring system.

5 Offline requirements and software

5.1 Overview

LAr TPCs record the complete electronic image of an ionizing event. Due to the optimal electron transport properties of the LAr medium (high electron mobility and small diffusion), large volumes

FIG. 62: The seven standard 19 racks containing the ArDM (CERN RE18) control system (COM, PLC1, PLC2, INT1 and INT2 rack), the high voltage supply of the PMTs (HV rack) and the data acquisition system (DAQ rack). The system was built in Collaboration with the CERN/PH-DT group.

can be instrumented with a spacial resolution down to the millimeter-scale. Ionization electrons drift over the distance $z = v \cdot t_{drift}$ towards the charge readout passing from liquid to gas phase, where they induce signals on different sets of readout electrodes, hereafter referred to as *views*. The readout views provide at each sampling time two or more projections of the (x, y) image of the event. In addition to the event topology, the amplitude of the recorded signals give a direct measure of the produced ionization charge along each track, providing calorimetry.

Track reconstruction aims at the extraction of the relevant information, such as the types and the momenta of the detected particles. In the simplest case, where particles stop inside the detector, the stopping power along the produced track allows to identify the particle [114, 115]. In case the particle does not stop inside the fiducial volume, an estimation of the momentum can be obtained by measuring the multiple scattering of the traversing particle [116]. Besides the reconstruction of tracks, it is possible to reconstruct showers: in this case, it is not needed to reconstruct each single hit in three dimensions. A strategy is to reconstruct global event parameters like the total charge, the shower direction, the charge profile and the vertex as well as the initial part of the shower. This latter is used to discriminate e^-/e^+ from γ/π^0 showers [117].

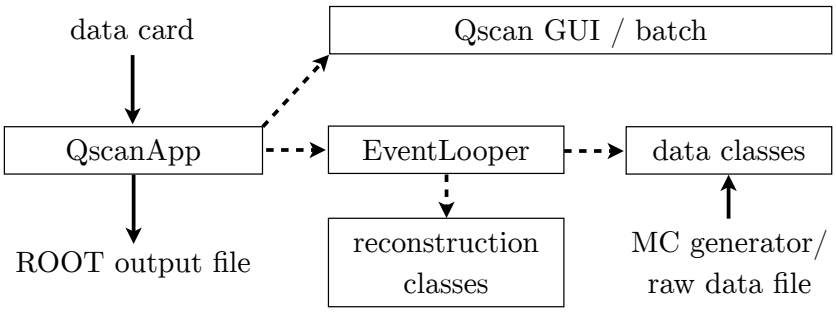

FIG. 63: Basic organisation of the Qscan software: boxes without frame are calibration, in and output files, while framed boxes name different classes.

5.2 The Qscan software

Qscan is a multipurpose software framework to simulate, reconstruct and visualize events from LAr TPC detectors. It was originally created and developed by the ETHZ group for the ICARUS experiment and was then adapted to other detectors. It was employed for all analyses the ICARUS data collected in Pavia [9–11, 118] as well as to reconstruct quasi-elastic neutrino events in the 50 L ICARUS TPC that was exposed to the CERN West Area Neutrino Facility WANF [115, 119]. Qscan allows to simulate, reconstruct and visualize events for various detectors. It is able to read raw-data of all our hardware setups developed since 1997. Due to the development of several new double phase LAr TPC prototypes, including the 3 L [19], the 120 L at J-PARC and the 200 L detector at CERN [17, 18], a set of new algorithms and a new ROOT[137] [120] based graphical user interface have been implemented. It is a precursor of other more recent software, such as the LArSoft[138] package that is being used by ArgoNeuT [121] and the future experiments MicroBooNE[139] and LBNE[140].

The Qscan software framework comes along with three main functionalities:

- It provides a set of tools to decode, store and reconstruct data from all our hardware setups.
- Being interfaced to VMC (and currently GEANT3 and GEANT4) to propagate particles through any detector geometry, it allows to produce fully digitized MC events that can be post-processed similar to real data from a detector.
- A batch-mode
- An interactive mode with graphical user interface that allows to scan raw data online or offline. Moreover, Qscan has a 3D event display to visualize MC truth events as well as the reconstructed event for both real and MC generated data inside the detector geometry.

In order to have a well structured software package that allows to add new detectors with minimal efforts, Qscan is written in the object oriented C++ language. As shown in the diagram in Figure 63, the main program *QscanApp* can either run in batch mode in order to process a large amount of data, or it initiates the graphical user interface of Qscan. Depending on which detector and which kind of reconstruction is asked by the user in the so called *data cards* file, the proper data class with the detector geometry is initialized as well as the reconstruction menu. After the initialization, the *EventLooper* goes from event to event, either reading an external data file or generating artificial events via MC simulation. Once all the signal waveforms are stored in the data class, the event is processed by the reconstruction algorithms. The resulting reconstructed objects are finally written into a file with the common ROOT format that can later be used for a further analysis. More details on the software layout are presented in [122].

5.3 Event simulation

Despite the fact that LAr TPCs ideally provide a high resolution image of any ionizing event, MC simulations are an important tool to validate reconstruction algorithms and to study the detector performance. Moreover, a working MC simulation of a detector allows to study different effects like non-uniform drift fields, different noise levels, impurities, *etc.* This is in particular important for physics performance studies of giant LAr detectors for future long baseline neutrino oscillation experiments [1]. All the MC simulation code and in particular the digitization procedures that are presented hereafter, have been validated with both testbeam and cosmic ray data, as reported in [122].

5.3.1 Particle propagation in detector geometries

Qscan uses the Virtual Monte Carlo package VMC[141] (see [123] and references therein) to interface with GEANT4[142], a toolkit for the passage of particles through matter [124]. Since the VMC interface loads the MC libraries at runtime, Qscan is completely independent from the MC simulation code, allowing for instance to use GEANT3 instead of GEANT4. The second advantage is that the ROOT geometry package *TGeo* can be used to define the geometry of the experimental setup. This feature is important since the same geometry definition can be used to track particles in GEANT3 and GEANT4. Moreover, TGeo is also the preferred geometry format to display the detector together with its reconstructed event objects in the three dimensional, ROOT based, event display. An example of a MC simulated muon event in the 200 L detector [17, 18] is displayed in Figure 64. (1) shows the overview of the geometry, consisting of the cylindrical cryostat and the cuboidal detector. The isolated TPC volume with the MC truth tracks are shown in (2) and (3) shows a closeup of the μ^- track in

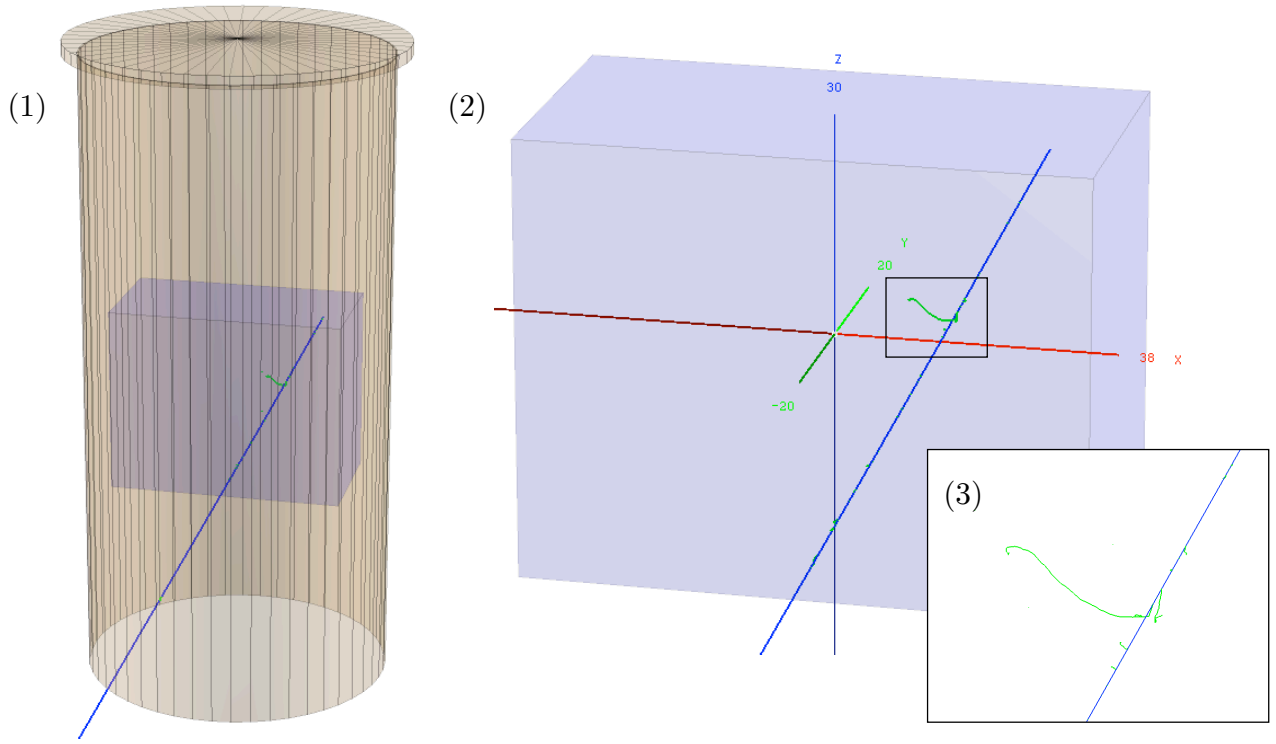

FIG. 64: Three dimensional event display of Qscan, showing the ROOT geometry of the 200 L detector and μ^-, tracked through the geometry by GEANT4. The figure shows an overview of the geometry (1), the extracted fiducial volume together with its local coordinate system (2) and a closeup of the μ^- track with several δ-electrons (3).

blue with some δ-ray electrons in green.

GEANT4 provides a large set of different physics processes. Depending on the required level of details and physics models, it is possible to enable or disable different electromagnetic and hadronic processes via physics lists. Typically we are using the QGSP_BERT physics list that uses the Quark Gluon String model for simulating high energy hadronic interactions. To provide accuracy at energies below 10 GeV, the list is extended with the Bertini cascade model [125]. Concerning the tracking configuration, depending on the readout pitch of the simulated detector, one usually has to define an upper limit for the stepping size in order not to see any descrete effects. Typically the maximum step length is fixed to about 10% of the readout pitch. Unlike in the case of typical GEANT4 simulations, particle propagation cut-offs are defined as kinetic energies, rather than ranges. In order to properly implement charge quenching effects, one wants to track secondary electrons, being produced along ionizing tracks, down to very low energies. As discussed elsewhere [11, 126], an electron tracking cut-off of 10 keV is a good compromise between microscopic accuracy and computing speed.

A first version of the $6 \times 6 \times 6$ m^3 detector geometry has been implemented in Qscan. The geometry is described with the ROOT *TGeo* package and the particle tracking through the detector can be

performed with either Geant4 or Geant3 using the Virtual Monte Carlo interface, as discussed above. The materials and their densities used in the simulation are listed in Table VII. Figure 65 shows a simulated event of a 5 GeV/c π^+ shot trough the beam pipe and initiating a shower in the liquid argon fiducial volume. Most parts of the detectors can be seen in the figure: the fiducial (cyan) and liquid argon (blue) volumes, the corrugated membrane (too thin to be visible), the insulating polyurethane foam (dark gray) the concrete outer vessel (light gray) and the beam pipe (green). The latter consists of a horizontal vacuum cylinder placed at 1.5 m from the top of the liquid argon level. The beam axis is oriented at 45 degrees with respect to the readout strips of both views.

Detector component	Material	Density[g/cm^3]
tracking medium	liquid argon	1.396
membrane	stainless steel	8.030
thermal insulator	polyurethane foam	0.100
outer vessel	concrete	2.500

TABLE VII: Materials and densities for the simulated $6 \times 6 \times 6$ m^3 detector.

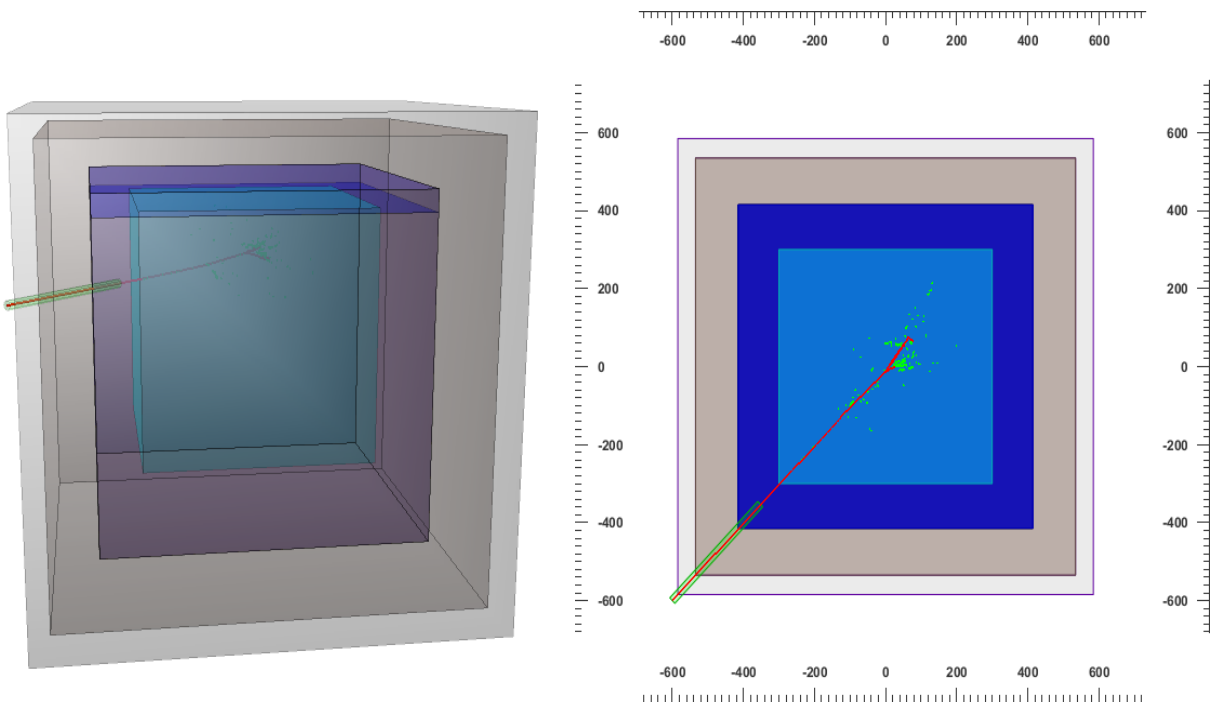

FIG. 65: Simulation of a 5 GeV/c π^+ event in the $6 \times 6 \times 6$ m^3 detector. 3 dimensional view (left) and top projection of the detector (right).

5.3.2 Waveform generation

The goal of the waveform generation is to convert the MC truth information to LAr TPC data, as it would be recorded in a real experiment. Based on the energy deposit ΔE_{dep} and the length Δx, given at each step of every tracked particle in the MC simulation, the readout signals are produced as explained in the following:

1. The deposited energy ΔE_{dep} is converted into the amount of produced ionization charge $\Delta Q_0 = e\,(\Delta E_{dep}/W_{ion})$ with the elementary charge e and the ionization work $W_{ion} = 23.6$ eV, as given in Table II. Due to electron ion recombination, which depends on the ionization density as well as on the applied electric field, a fraction of the produced electrons recombine. Since Birks' approximation gives the best fit to the reconstructed data [11], it is reasonable to implement quenching at MC level by multiplying the charge with $\mathcal{R}_{Birks}(\Delta E_{dep}, \Delta E_{dep}/\Delta x)$. The two parameters of the model $A_{MC} = 0.8$ and $k_{MC} = 0.05$ (kV/cm)$\left(\frac{\text{MeV}}{\text{g/cm}^2}\right)$ provide good agreement with the data.

2. The remaining charge is then transported up to the collection plane. After choosing the coordinate system such that the anode plane is parallel to the (x, y) plane, the charge, being initially produced at (x, y, z), is drifted along the electric field lines until it leaves the fiducial volume or it reaches the readout plane. In case of a constant field $(0, 0, \mathcal{E})$, the final charge position equals $(x' = x, y' = y, z' = z_{anode})$ and the corresponding drift time is $t_{drift} = (z_{anode} - z)/v_{drift}(\mathcal{E})$. Otherwise, in case of an inhomogeneous electric field, an external look-up table, providing the final coordinate as well as the drift time for any point within the fiducial volume, is used. After including also charge attenuation effects due to an imposed finite free electron lifetime τ_{MC}, the charge is given by

$$\Delta Q = \frac{\Delta E_{dep}}{W_{ion}} \cdot e \cdot \frac{A_{MC}}{1 + k_{MC}/\mathcal{E} \cdot \Delta E_{dep}/\Delta x} \cdot e^{-t_{drift}/\tau_{MC}}. \tag{5.1}$$

   Longitudinal diffusion effects are included by convoluting the charge with a Gaussian of width given by Equation (3.2).

3. Depending on the arrival position $(x', y', z' = z_{anode})$ of the drift charge ΔQ, currents are induced on the corresponding readout electrodes of the different views. These currents are then further processed by a charge sensitive preamplifier. The finally recorded signal $V_{out}(t)$ is a convolution

of the induced current $I(t)$ and the response of the preamplifier $h(t)$:

$$V_{out}(t) = I * h(t) = \int_{t_0}^{t} I(t') \cdot h(t - t')dt'. \tag{5.2}$$

Obviously both the preamplifier response and the induced currents depend on the readout type and the used electronics. The simplest case is the LEM readout with a 2D anode: due to the fast electron drift in gas and the short induction gap between LEM and 2D anode, the induced current $I(t)$ approaches a δ-function and the signal is directly given by the fast response of the preamplifier.

After finishing this procedure for each step, noise of a given amplitude can be added on top of the signal waveforms. Besides the generation of white noise, it is also possible to use a specific frequency spectrum that has e.g. been taken from real data. The final step is the digitization of the generated waveforms. Figure 66 shows on top the generated waveforms of the MC μ^- from Figure 64 and on the bottom the corresponding event display.

5.4 Event Reconstruction

After recording data from the detector, the data is processed by several reconstruction algorithms. Starting from the local, channel-by-channel signal discrimination, the final goal is to reconstruct physical objects like tracks, showers and event vertices. As there can be large differences among detectors and event types, Qscan provides various methods to reconstruct events. The reconstruction basically goes through the following steps:

1. The raw waveforms are processed: this involves noise reduction as well as the subtraction of the baseline (see Section 5.4.1).

2. Hits, defined as signals that are discriminated from the noise, are identified and reconstructed (see Section 5.4.2).

3. Clusters are formed by grouping close hits together (see Section 5.4.3).

4. Tracks are identified for each view (see Section 5.4.4).

5. Finally, the three dimensional track reconstruction is done by matching coincident tracks from different views (see Section 5.4.5).

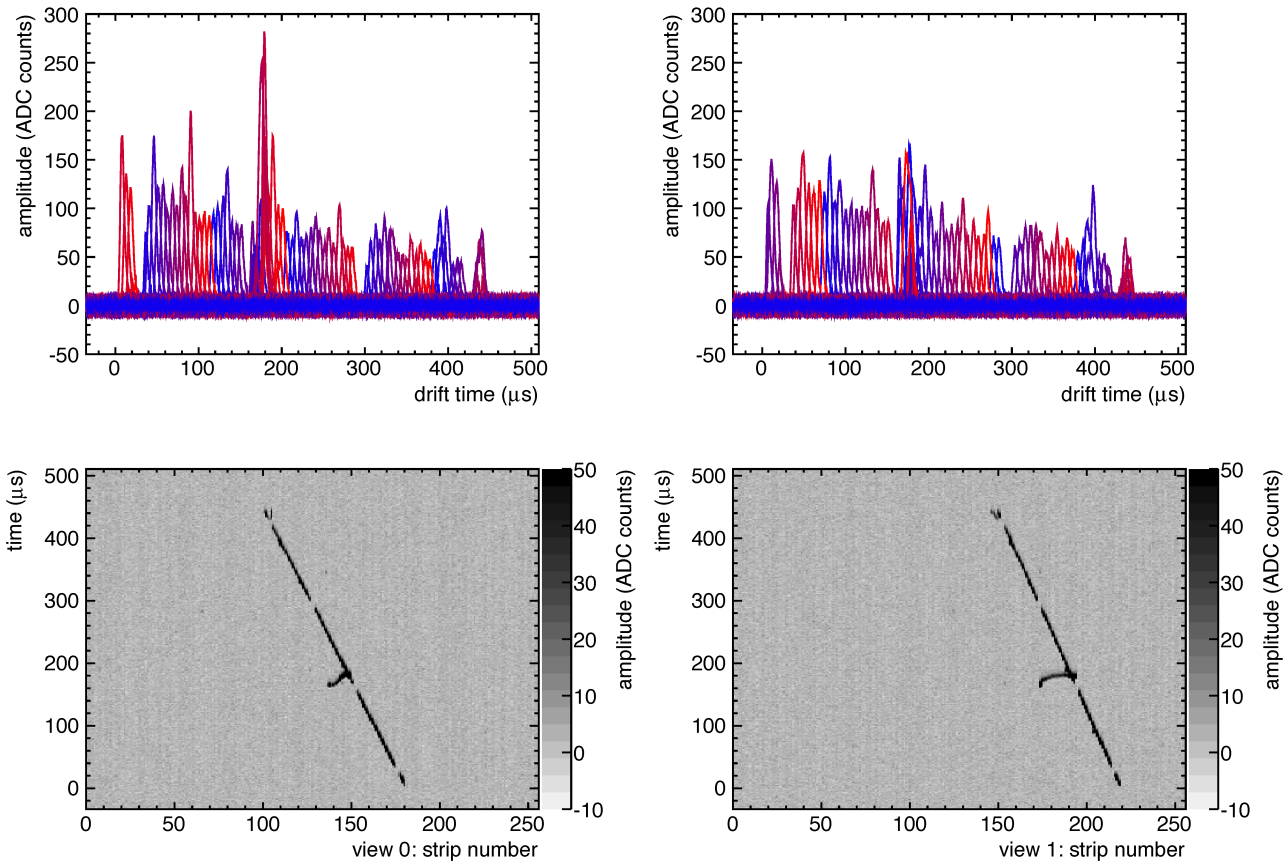

FIG. 66: Example of a fully MC generated μ^- event in the 200 L detector. The MC steps of the same event are shown in Figure 64. The waveforms for the two views (left and right) have been generated, using the known ETHZ preamplifier response, and Gaussian noise with an RMS value of 3 ADC counts. Top: waveforms $V_{out}(t)$ of all the readout channels are shown with different colors. Bottom: typical event display, showing the drift time vs strip number. The greyscale is proportional to the amplitude.

5.4.1 Signal processing

The data acquisition system records the amplified, shaped and digitized output voltage $V_{out}(t)$ for each electrode with a discrete time sampling. In order to extract physical signals efficiently and accurately, a minimal signal to noise ratio of about 10 is required. Although the electronics is in principle designed to fulfill this requirement, experimental data can be distorted by external noise sources and an imperfect shielding of the detector and the signal lines. In order to suppress noise without affecting the signal component too much, hence improving the signal to noise ratio, two different algorithms are used: the *Fast Fourier Transform (FFT) filter*, and the *coherent noise subtraction* algorithm.

The *FFT filter* makes use of the fact that induced noise, being produced by external sources like switching power supplies, computers, *etc*, is often dominated by a few specific frequencies. After transforming the waveforms $V_{out}(t)$ to the frequency space, the Fourier transformed waveforms $\hat{V}_{out}(\omega)$ are processed in order to reduce the noise components. The final, noise suppressed waveforms $V_{out,filt}(t)$

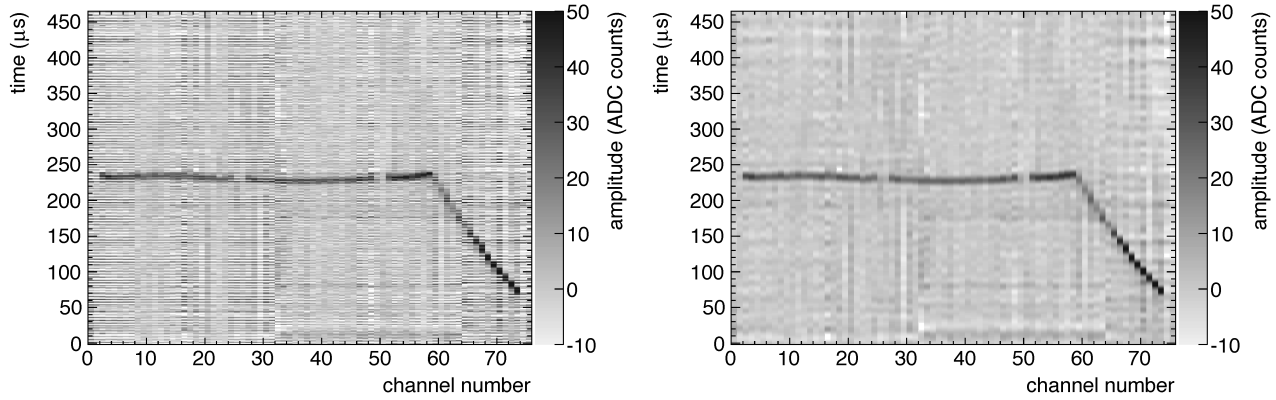

FIG. 67: Raw (left) and FFT filtered (right) stopping K^+ event from the 120 L single phase LAr TPC in a beam test at J-PARC ([126]). The noise pattern, shown on the raw event on the left, is removed by the low pass filtering with a smoothened cut-off at the frequency of 80 kHz.

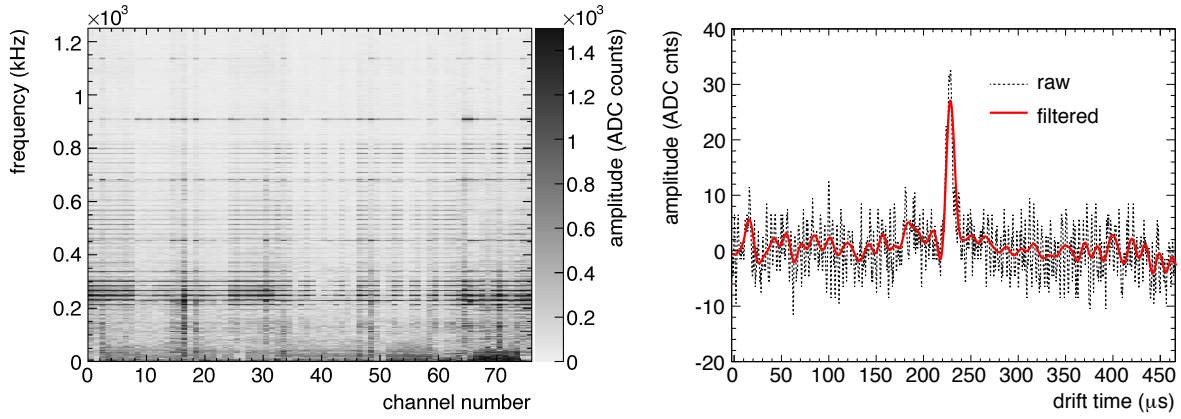

FIG. 68: Left: power spectrum of the raw event from Figure 67. The two dimensional histogram shows the amplitude for each readout channel and frequency bin. Common noise frequency on all the channels are visible well above the 80 kHz cut-off. Right: single readout channel raw (dashed black line) and the filtered waveform (solid red line).

are then obtained by applying an inverse FFT to $\hat{V}_{out,filt}(\omega)$. Due to the fact that the waveforms are discrete and the total number of samples is an integer power of two, the computing time is minimized by using the FFT implementation from [127].

A concrete example of the FFT algorithm is presented in Figures 67 and 68: the K^+ beam event, recorded with the 120 L single phase LAr TPC in the beam test at J-PARC [126], demonstrates the effect of the filter. The high frequency noise, seen in the raw event on the left of Figure 67, is efficiently removed in the filtered event on the right. In this case the best way to improve the signal to noise ratio was to suppress frequencies above 80 kHz. The left plot of Figure 68 shows the amplitude for each channel and frequency. In this plot it can be seen that a continuous background is superimposed

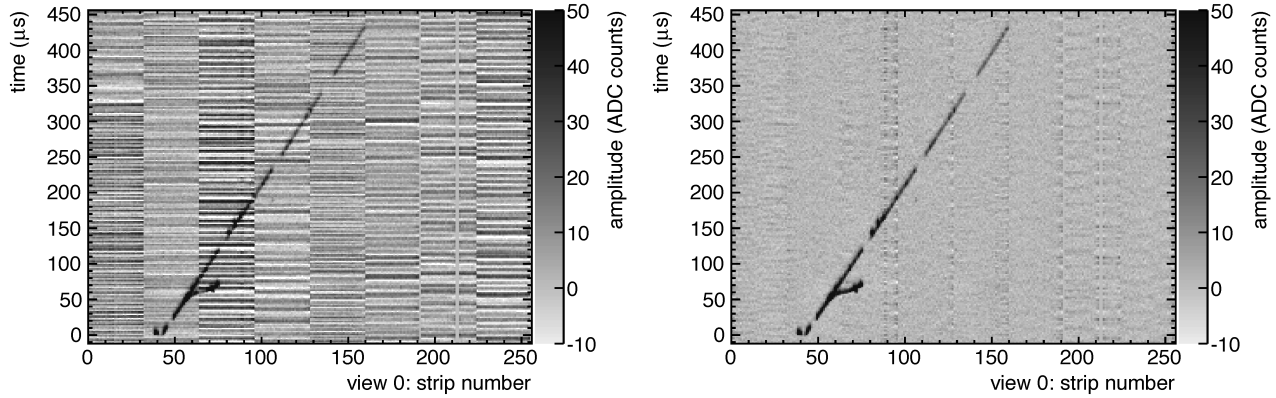

FIG. 69: Cosmic ray event from the 200 L LAr LEM-TPC that is described in **??**. Left: raw event that shows a characteristic coherent noise pattern. Right: final event, after applying the coherent noise filter.

with discrete frequency lines. While the continuous component is due to the signals and the intrinsic preamplifier noise, the sharp lines correspond to discrete noise frequencies that are induced by external sources. Due to the fact that most of the noise frequencies are above 100 kHz, a smooth cut-off, implemented with a Fermi potential of width 3 kHz, efficiently suppresses the noise, while keeping the signals, besides a reduction of the bandwidth, unaffected. Unlike a smooth cut-off, a sharp cut in the frequency spectrum introduces artefacts in the time domain. Figure 68 shows the effect on a single waveform before (dashed black line) and after filtering (solid red line).

The *coherent noise filter* is implemented to remove identical noise patterns that are seen on larger sets of readout channels. Unlike in the case of the FFT filter, which directly suppresses the frequencies of single channels and thus reducing the signal bandwidth, the coherent noise filter ideally subtracts only the noise while keeping the signals unchanged. During the operation of detectors it is often observed that all the readout channels, being hosted on the same readout board, have exactly the same noise in terms of frequency, phase and amplitude. An example of such an event, recorded with the 200 L double phase LAr LEM-TPC [17, 18], is given in Figure 69. Since the noise of every channel that belongs to the same acquisition board is almost identical, it can be considered as disturbance of the baseline. This time-dependent baseline first has to be computed for each single time sample, including all the channels on a physical readout board. Finally, similar to the subtraction of a constant pedestal, the baseline is subtracted from each sample. The difficulty of the calculation of the time-varying baseline is to select only the channels without a signal. Since signals are amplitude fluctuations with respect to the baseline, a good way to compute the baseline value for a given time sample is to use only the N channels with the smallest voltage values. Depending on the needs, N can be chosen between 1 and 32: in the case of $N = 1$, the baseline is defined at each time sample t by the minimum

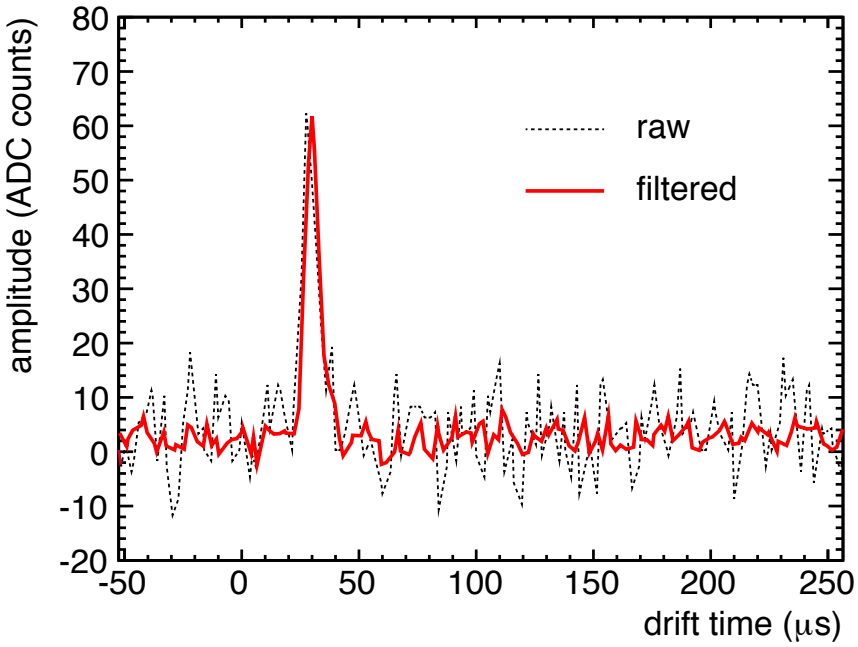

FIG. 70: Single waveform, extracted from the event shown in Figure 69. Both the raw (dashed black line) and coherent noise filtered (solid red line) waveform are shown.

Voltage $V_{out}(t)$ of all the 32 readout channels per acquisition board. On the other hand, in the case of N = 32, signals are discarded and all the channels are used to calculate the baseline. The choice $N \approx 16$ allows that signals are not affected, even in case they are present in half of the readout channels. Figure 70 shows a single readout channel, taken from the same event that is presented in Figure 69. The noise fluctuations that are present in the unfiltered event (dashed black line) are significantly suppressed after applying the filter (solid red line). It can also be seen that the algorithm does not affect the signals, despite its significant effect on the noise.

After suppressing the noise, the (constant) pedestal of each waveform has to be computed and subtracted from each sample. In order to avoid any bias due to physical signals, only pre-trigger samples are used to compute the mean value. Another possibility is to use the most probable value since it does not depend on tails, which are due to signals.

5.4.2 Hit identification and reconstruction

The smallest sub-unit of the reconstructed event is the *hit*. Physically, a hit corresponds to a track segment below a readout strip. The charge of this segment is then drifted towards the strip, where it induces a signal. The information that is attributed to a hit is the deposited charge ΔQ, the three-

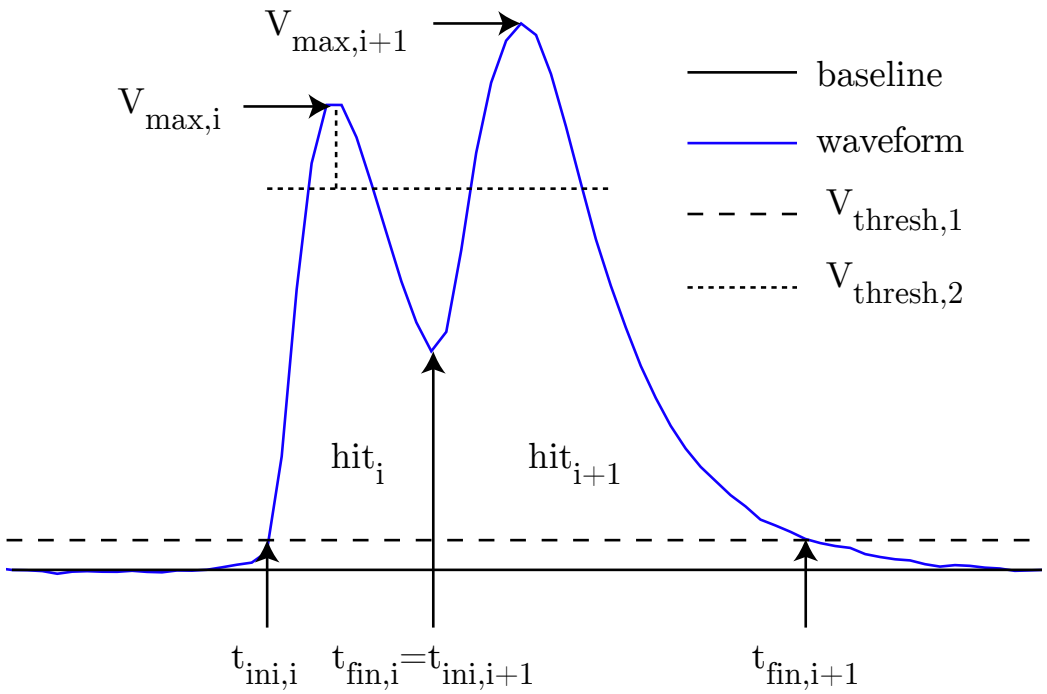

FIG. 71: Waveform (blue line) from a cosmic ray event that was recorded with the 3 L detector, showing a double hit structure (hit$_i$ and hit$_{i+1}$). It defines the hit variables t_{ini}, t_{fin} and V_{max} as well as the *baseline* (black line) and the two thresholds $V_{thresh,1}$ and $V_{thresh,2}$.

dimensional length Δx of the track segment, the drift time, which is equivalent to the drift coordinate z, the readout view and the electrode strip number. Hits have to be extracted from the signal waveforms by means of a standard threshold discrimination. Due to changing noise conditions, the threshold is defined in relation to the measured RMS noise value σ, which is measured for each event and readout strip, using the pre-trigger samples. A typical value for the threshold is $V_{thresh} = 3\sigma$. In the general case there can be several close, or overlapping tracks per event, producing a superposition of several signals/hits on a single readout strip. The shaping time constants of the preamplifiers are chosen such, that double tracks being separated by a few μs can be resolved. In order to explain the working principle of the *hit-finding* algorithm, Figure 71 shows an example of two subsequent hits in a single readout channel. The waveform was recorded with the 10×10 cm^2 LAr LEM TPC prototype [19] and shows a single waveform from a cosmic ray track with an emitted knock on electron.

Moving from the left to the right, a hit candidate hit_i is initiated in case the signal waveform (blue) exceeds a pre-defined threshold $V_{thres,1}$ (dashed line) and terminated, when it either goes again below the same threshold or in case a new, subsequent hit candidate hit_{i+1} is triggered. The imposed trigger condition for subsequent hits is that the minimum voltage between the two hit candidates goes below the value $min(V_{max,i}, V_{max,i+1}) - V_{thres,2}$. $V_{thres,2}$ (dotted line) is a secondary pre-defined threshold, responsible for the re-triggering of subsequent hits. Besides increasing the threshold, the number of

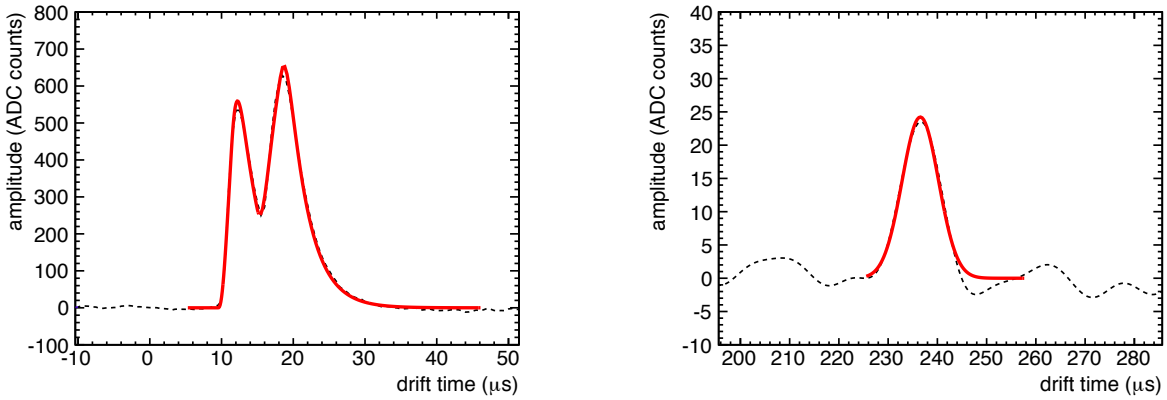

FIG. 72: Waveforms (dashed black line) from two different detectors, superimposed with the fitted functions (solid red line). Left: the cosmic ray event from the 3 L double phase LAr LEM-TPC [19] is, due to the fast response, fitted with a function that is based on the preamplifier response function. Right: beam event from the 120 L single phase LAr TPC [126], due to its slow signals fitted with a Gaussian.

fake hits due to noise can be reduced by imposing a minimum time over threshold $t_{fin} - t_{ini} > \Delta T$. Initial and final drift times (t_{ini} and t_{fin}), as well as the hit amplitudes V_{max} are defined as indicated in Figure 71. In order to calculate the integral of each hit, the waveform is integrated from the initial to the final time sample. To reduce any bias, coming from the height of the threshold, the window, in which the integral is computed, can be extended in case there is no other hit attached.

The main parameters of the hits that need to be reconstructed are the *hit time* and the *hit integral*: together with the location of the corresponding readout channel, the hit time directly provides the information of the hit location in the considered view (projection), whereas the hit integral is related to the produced ionization charge and therefore provides the calorimetric information. In order to improve the accuracy of these two evaluated parameters, the signal waveforms can be fitted with a pre-defined function. Two examples of waveform fits are shown in Figure 72: the left plot shows the waveforms of a double hit from a cosmic ray event, recorded with the 3L double phase LAr LEM-TPC [19], whereas the right plot is a beam event, recorded with the 120 L single phase LAr TPC [126]. As the LEM-TPC has a faster signal induction, the used fitting function is a convolution of a constant current

$$I(t) := I_0 \cdot \delta(t - t_0) \cdot \delta(t_0 + \Delta t - t) \tag{5.3}$$

of duration Δt and integral I_0 and the normalised response of the ETHZ preamplifier $h(t)$ [17]:

$$V(t) = I * h(t) = \int_{t_0}^{\infty} I(t')h(t-t')dt'. \tag{5.4}$$

The function is analytically computed and since the response with the integration and differential time constants is already known, the only three fitting parameters are the integral I_0, the time t_0 and the signal width Δt.

5.4.3 Cluster finding

After a successful hit-finding, adjacent hits of different readout channels are grouped together. Since physical objects like tracks or showers are extended, the *hit clustering* is the first step towards a more global reconstruction of the event. The second advantage of clustering is that single hits can easily be suppressed by applying a cut on the cluster size. Besides the improvement of the purity, also the hit finding efficiency can be increased, since it is possible to search for more hits around the borders of clusters with a lowered threshold. The clustering algorithm is based on the search of directly adjacent hits: starting from a single hit, the *nearest neighbour* algorithm (*NN*) iteratively expands the cluster by adding close hits. Looping over all hits in the cluster, it searches for unclustered hits within a pre-defined time and readout channel range around the current hit. Once a new hit is found, it is added to the cluster. The algorithm continues looping, until no more hits are found in the vicinity of the cluster. Like in the case of the hit-finding algorithm, the parameters of the algorithm depend on the detector as well as on the event type. Since the NN clustering is optimised to reconstruct connected objects, like tracks, it was perfectly suitable for the reconstruction of the 3 L, 120 L and 200 L TPC data. A more detailed description of the implementation of the NN clustering algorithm is presented in [118].

5.4.4 Track reconstruction

Starting from general clusters that can assume any topology, the tracking algorithm, which was used for the reconstruction of the 200 L LAr LEM-TPC data [17, 18], aims at the identification of straight tracks. The straight track assumption is justified, since the multiple scattering is negligible for the maximally 60 cm long cosmic ray tracks. The method being described here can be easily generalized to the case of bent tracks.

In the following, we first describe a Hough-transform based tracking algorithm for the identification of the main, through-going cosmic rays and then a second algorithm to reconstruct knock-on electrons, appearing as secondary tracks. The basic idea of the track identification, being described here, is to

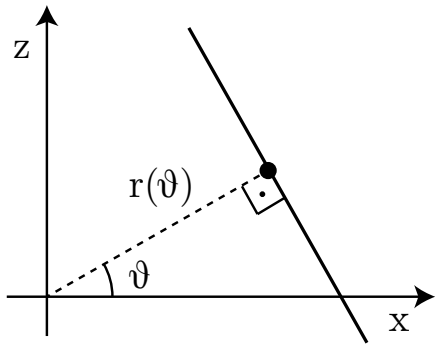

FIG. 73: Straight line parametrization, used for the Hough transformation.

convert the problem of finding aligned hits into the trivial problem of finding a maximum. The *Hough Transform (HT)* [128] transforms hits with coordinates (x, z), where x is given by the readout strip number and z by the drift time, into the parameter space of straight lines, also called *Hough space*. The basic procedure of the HT is to evaluate the parameters of all the straight lines, going through each hit in the (x, z) plane. If a subset of points are aligned, there is a single line going through all of them and its parameter pair (angle θ and offset $r(\theta)$) will appear as a maximum in the two dimensional, binned Hough space. Looping over each cluster, the HT based track identification algorithm goes through the following steps:

1. Each hit coordinate pair (x, z) is transformed via HT to the parameter space. As shown in Figure 73, straight lines are parametrized by an angle θ and the minimal distance to the origin of the coordinate system r. The transformation to the Hough space is then given by

$$r(\theta) = x \cdot \cos\theta + z \cdot \sin\theta. \tag{5.5}$$

   After defining the binning of the Hough space with the variables (r, θ), the algorithm computes $r(\theta)$ for each angle θ and adds the point with weight 1 to the two dimensional histogram. This step is then repeated for each hit of the cluster.

2. The bin with the largest number of entries (θ_{max}, r_{max}) gives then directly the parameters of the straight line that crosses most of the hits. In order to avoid fake tracks, a minimum threshold of typically $N_{min} = 4$ hits is required. The two dimensional track is then defined by all the hits that are close to the found straight line.

3. In case it is needed to find other straight tracks, step number 2. can be repeated for the residual hits that belong to the cluster but not to a track, until the number of hits in a track candidate goes below the user-defined threshold N_{min}. Finally, the main track is again fitted with a straight

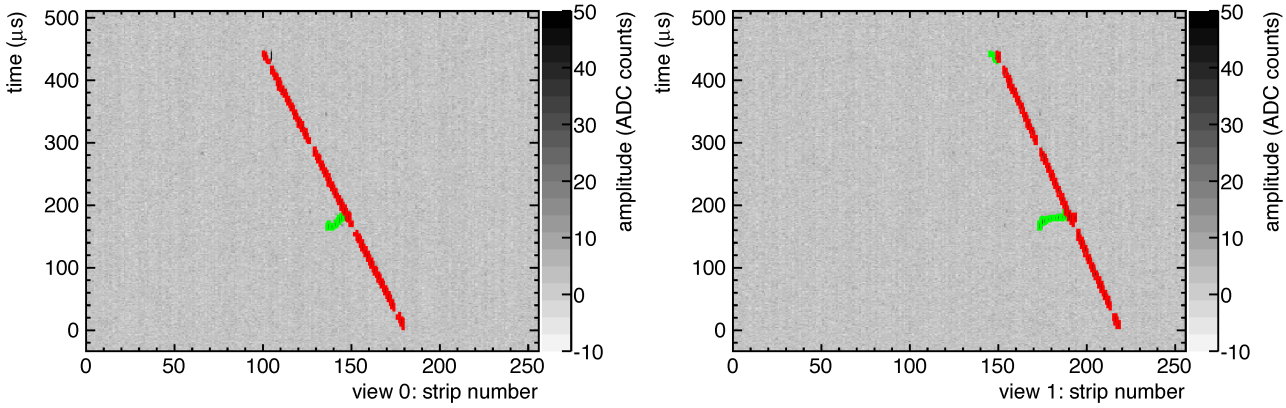

FIG. 74: Two views of a fully reconstructed MC generated muon with a knock-on electron in the TGeo geometry of the 200 L double phase LAr LEM-TPC [17, 18]. Hits belonging to the main track are highlighted in red; hits belonging to secondary tracks that are attached to the main tracks are green.

line.

4. After finding the main track, all residual hits that belong to the cluster but not to the track, are tagged as δ-ray hit candidates. Then, the algorithm groups and tags close δ-ray hit candidates as δ-rays. Since single hits can easily be produced by noise, δ-rays require at least two consecutive hits. Figure 74 shows the MC generated μ^- with a δ-ray. The event display for both views 0 (left) and 1 (right) show in red the hits that belong to the main track and in green the hits that belong to δ-rays.

5.4.5 Three dimensional track reconstruction

The most important information, obtained from the hits, is the charge ΔQ that is related to the signal integral and the three dimensional track length Δx. The information of the two dimensional tracks from complementary views have to be combined in order to reconstruct Δx as well as the complete three dimensional image of the event. Due to intrinsic ambiguities coming from the projection technique, this task is in general complex. However, the fact that only straight tracks are considered, simplifies the three dimensional reconstruction a lot, since the problem is reduced to the simple matching of two-dimensional tracks: comparing the drift times of the first hits of tracks, an algorithm loops over all two dimensional track candidates until a unique pair of tracks from both views is found. In case of the event shown in Figure 74, the algorithm links the two red tracks, since the first hits from view 0 and 1 both have a similar drift time $t_{drift} \approx 0$ (the μ is entering from the top of the chamber through the anode). To reconstruct the three dimensional hit coordinates (x_0, y_0, z_0) and (x_1, y_1, z_1) for the views 0 and 1, the straight line approximation is used: first, the tracks of both views (view 0

and view 1) are fitted with the linear equation

$$z(x) = a_0 \cdot x + b_0 \text{ and } z(y) = a_1 \cdot y + b_1 \tag{5.6}$$

with the slopes $a_{0,1}$, the offsets $b_{0,1}$ and the common drift coordinate $z = t_{drift} \cdot v_{drift}$. Equation (5.6) makes use of the fact that the strips of the two readout views are perpendicular and the coordinate system is chosen such that view 0 (1) directly provides the x (y) coordinate. Besides the naturally provided readout coordinate z_0 (z_1) and x_0 (y_1) for view 0 (view 1), inverting Equation (5.6), the missing coordinates y_0 (x_1) are given by

$$y_0 = \frac{z_0 - b_1}{a_1} \text{ and } x_1 = \frac{z_1 - b_0}{a_0}. \tag{5.7}$$

Besides the absolute position of the hits of view 0 and view 1, the three dimensional track length

$$\Delta r_{0,1} = \sqrt{\Delta x_{0,1}^2 + \Delta y_{0,1}^2 + \Delta z_{0,1}^2} \tag{5.8}$$

has to be computed for both views independently. In the case of view 0 (view 1), Δx_0 (Δy_1) is equal to the readout pitch that is typically for both views equal to 3 mm. Further, Δy_0 and Δx_1 can be computed according to Equation (5.7) and $\Delta z_{0,1}$ is given by Equation (5.6). As final result for the three dimensional track pitch we get

$$\Delta r_0 = \Delta x_0 \sqrt{1 + a_0^2/a_1^2 + a_0^2} \text{ and } \Delta r_1 = \Delta y_1 \sqrt{1 + a_1^2/a_0^2 + a_1^2}. \tag{5.9}$$

Finally, using the proper charge calibration of the readout and $\Delta r_{0,1}$ from Equation (5.9), the expression $\Delta Q_{0,1}/\Delta r_{0,1}$ can be computed for both views. For reasons of simplicity, hereafter the same expression is often renamed to $\Delta Q/\Delta x_{0,1}$ or $dQ/dx_{0,1}$.

The hits that have been tagged as δ-ray hits (see Section 5.4.4), do not necessarily form straight tracks. Therefore, the best way to reconstruct those hits is to find for each δ-ray hit of view 0 a coincident δ-ray hit of view 1. This means, that the resulting coordinate of each hit on view 0 are defined as (x_0, y_1, z_0), where y_1 is taken from a hit on view 1 with a similar drift time, i.e. $|t_{drift,1} - t_{drift,0}| < \epsilon$. In case no coincident δ-ray hit is found on the other view, it is matched with the main track, since in such a case it can be assumed that δ-ray and μ are superimposed. An example for the final, three dimensionally reconstructed MC generated event from Figures 64 and 74 is shown in Figure 75: the coordinates of all reconstructed hits of view 0 are shown in the 3D display, superimposed with the MC tracks. It can be seen that the through-going μ^-, as well as the δ-ray in green match with the

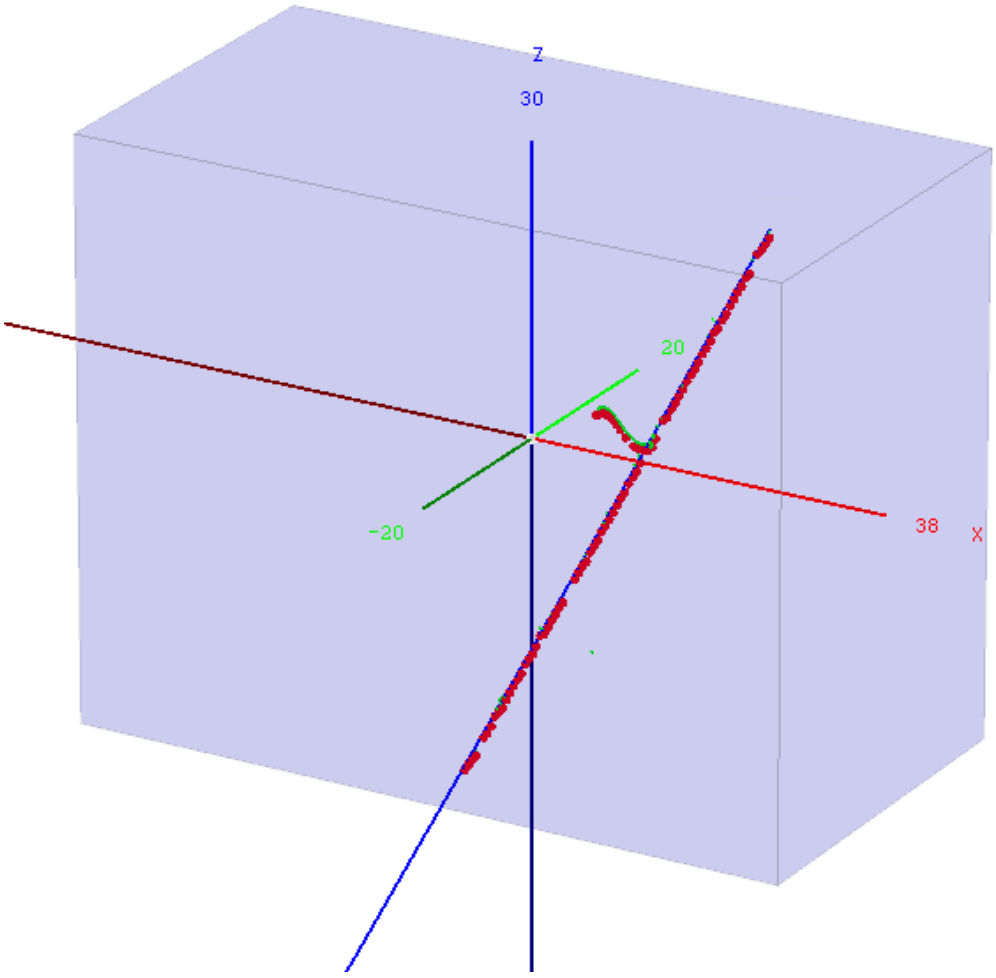

FIG. 75: Full reconstruction of view 0 hits (red dots) of the MC generated cosmic ray event from Figures 64 and 74. The MC truth μ^- track is shown in blue, the emitted δ-ray in green.

reconstructed hits in red.

5.4.6 Particle flow - the PANDORA methodology

Alternative ways of reconstructing events starting from Qscan hits are being developed, in an effort to create a fully-automatic reconstruction package capable of handling all expected neutrino interaction topologies.

The PANDORA framework [129] was originally written for particle flow calorimetry in heterogeneous collider detectors, specifically the ILC and CLIC, by a group at the University of Cambridge led by Mark Thomson. This method of reconstruction attempts to identify all primary final-state particles in an event, and then associate all energy deposits in the detector with a specific primary particle, thus allowing to estimate the energies of all final-state particles through calorimetric methods.

The original PANDORA algorithms are not immediately suitable for reconstruction of neutrino

events in LAr TPCs. For example, in a non-collider environment, there is no a priori knowledge of the vertex location from the beam geometry, and so the primary vertex must be reconstructed from event data. In addition, the original algorithms use the fact that different particle species deposit their energy in different parts of a heterogeneous detector (e.g. tracker, ECAL, HCAL, MRD) – this is not the case in a homogeneous liquid argon detector.

For this reason, the PANDORA developers have produced a suite of algorithms designed specifically for Liquid Argon reconstruction [130]. Essentially, the algorithms do the following:

- Split data into separate 2D projections.
- Perform first-pass hit clustering, by
  - clustering individual hits using a nearest-neighbour method; then
  - associating subclusters based on proximity and direction.
- Split clusters using a kink search algorithm.
- Find the primary vertex based on presumed beam direction and cluster positions/directions.
- Identify primary final-state particles ("seed clusters"), based on cluster length and proximity to vertex.
- Association of each remaining, "non-seed" cluster, with "seed" clusters, so that all energy deposits from a single final-state particle are grouped together.

In practice, this process is rather involved and each step is split into several discrete algorithms, each performing a tightly specified operation on the existing list of clusters; the philosophy followed is that each step should be as conservative as possible, since it is much easier to combine objects later than to separate objects which have already been combined. The present version of the PANDORA reconstruction reconstructs hits in 2D projections rather than in 3D; an algorithm for matching the views to produce a 3D event does not yet exist, but is in development.

Examples of successfully reconstructed Monte Carlo events in liquid argon can be seen in Figure 76.

5.4.7 Preliminary performance evaluation

The performance of PANDORA is presently being evaluated by the GLACIER working group, and feedback is being sent back to the PANDORA developers to aid continuing development of the algorithms. Interfaces have been written to convert Qscan Monte Carlo data into the format expected

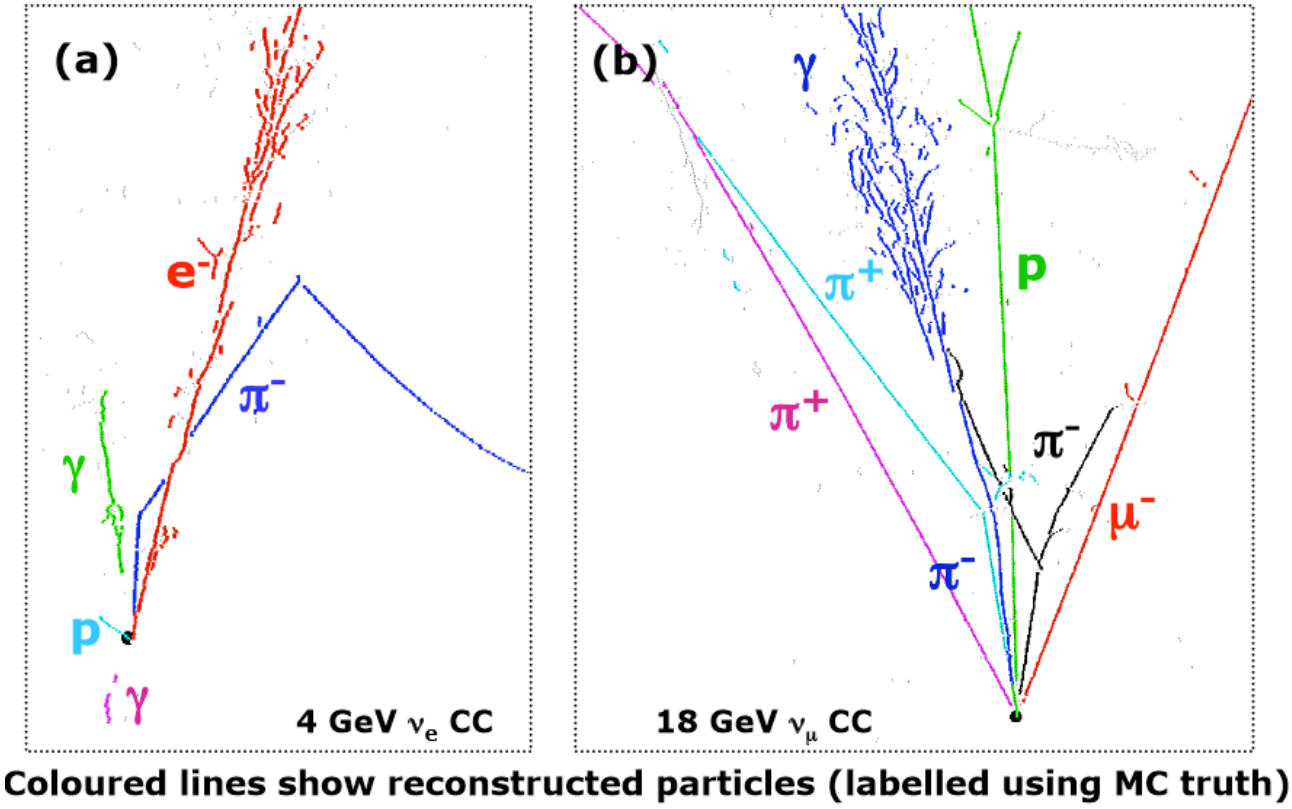

FIG. 76: Examples of successfully reconstructed Monte Carlo events in liquid argon, produced by the PANDORA developers (taken from [130]). Black circles indicate the reconstructed primary vertex.

by the PANDORA framework, and used to test the response of PANDORA to both particle gun Monte Carlo and neutrino events.

Proton tracks were generated using Qscan, and those stopping with no hadronic interactions were examined to check the capability of PANDORA to reconstruct simple tracks. It is observed that tracks are reconstructed with negligible loss of hits, except when they are close to perpendicular to the defined beam direction – this is shown in the examples in Figure 77, and in the efficiency plot in Figure 78. The drop in efficiency becomes significant only at $\sim 20^\circ$ from the perpendicular.

The variability as a function of angle may be understood by noting that several PANDORA algorithms make use of the beam direction to order hits into pseudo-layers when making clustering decisions; however improving the algorithm behaviour for sideways tracks is currently a high priority for the developers. Of course, tracks running parallel to a wire in projection are also intrinsically more difficult to reconstruct, since the number of discrete hits observed is smaller.

A similar sample to the above was generated, but with two protons, one along the beam axis and one at a variable angle to it (in a single 2D projection) – see Figure 79. It is observed that for tracks covering a significant number of strips, the tracks are successfully separated with 100% efficiency at

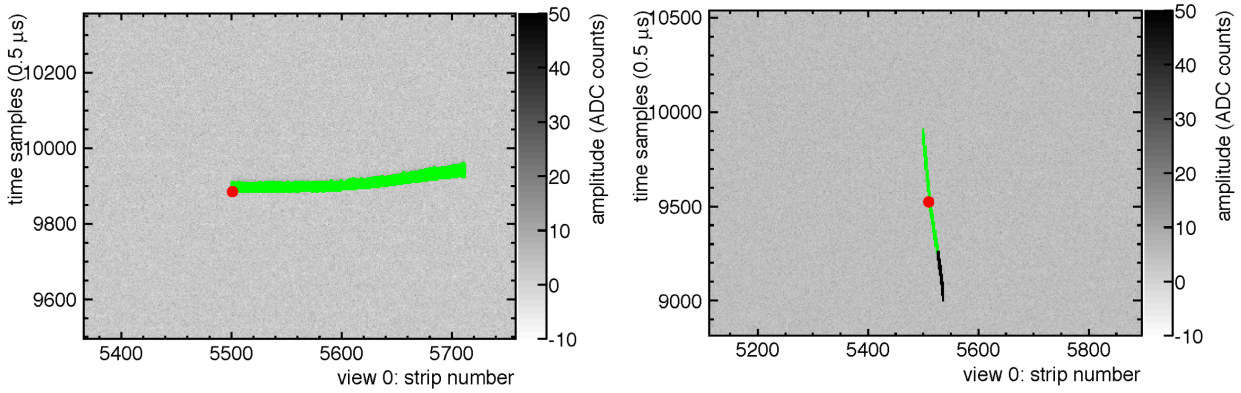

FIG. 77: Examples of PANDORA reconstruction of single proton tracks green hits are those which have been clustered, black hits are those which have been missed. The track in the right plot is almost perpendicular to the beam direction, and is not fully reconstructed.

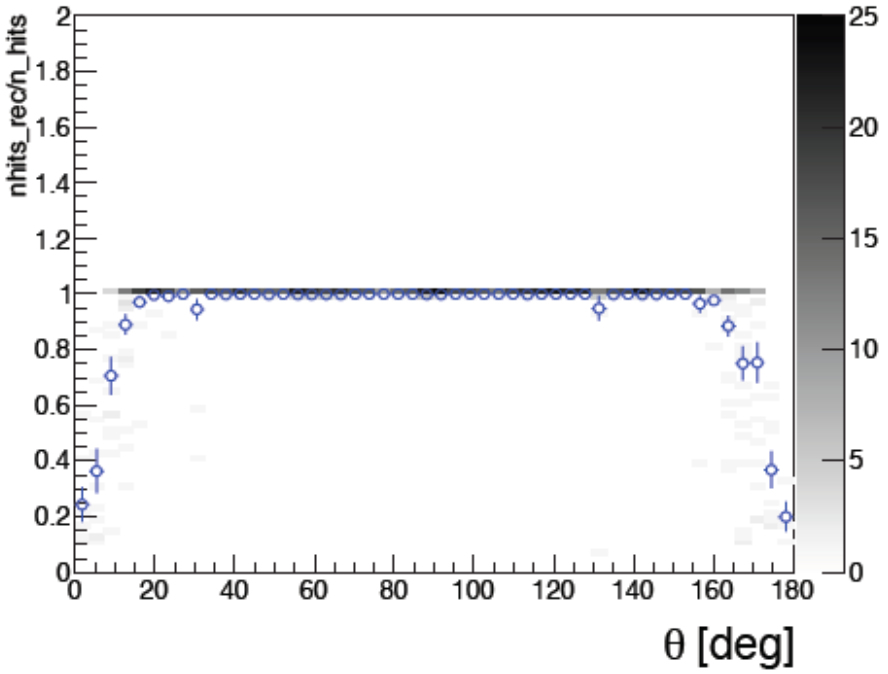

FIG. 78: 2D histogram showing the distribution of the proportion of reconstructed hits for a single proton track, as a function of track angle. A graph showing the mean proportion of reconstructed hits at each angle is overlaid.

angles greater than about 5 degrees (Figure 5).

The vertex finding performance of PANDORA has been evaluated using around 300 muon neutrino CCQE interactions produced using GENIE and Qscan. The neutrinos used to produce the interactions were at energies below 4 GeV. The beam direction for these events was perpendicular to the wires in one view (view 0) of the detector, but parallel to the wires in the other view (view 1). This meant that in view 1, the pseudo-layering axis used by PANDORA was perpendicular to the simulated beam direction.

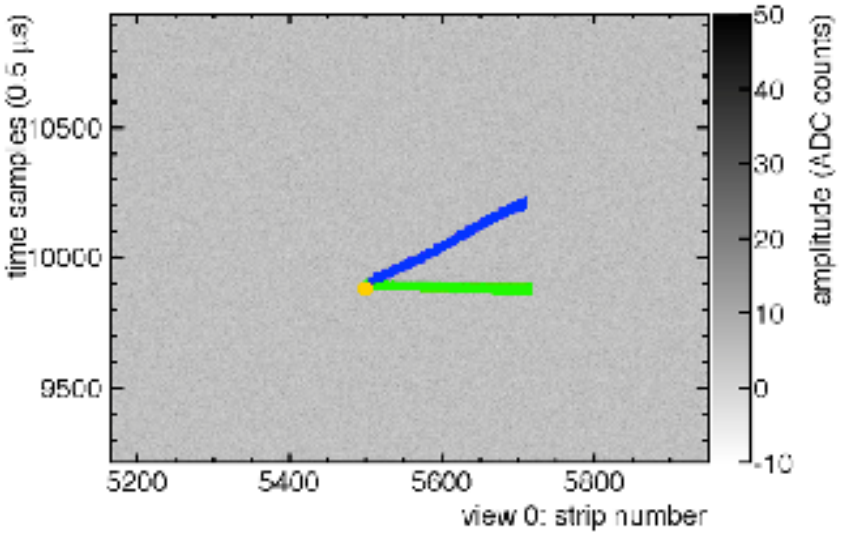

FIG. 79: Example of a double proton gun event, with the two protons correctly reconstructed (two clusters in different colours).

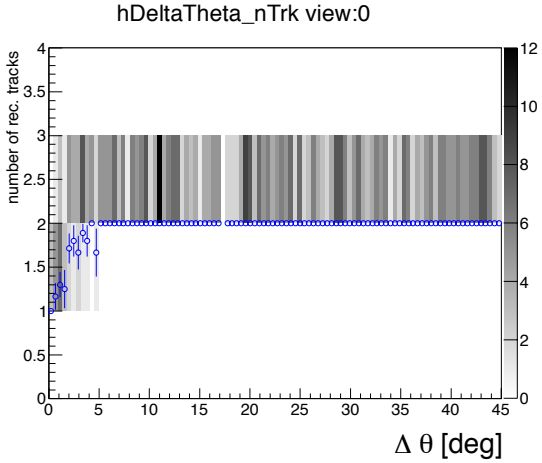

FIG. 80: Histogram showing the distribution of number of reconstructed tracks for different double proton gun opening angles. The mean number of tracks for a given angle is overlaid as a graph.

Figure 81 shows the distributions of distance between true and reconstructed vertices, for both detector views. It can be seen that the performance in view 0, where the beam is parallel to the strip axis, is excellent, but in the other view then the vertex is routinely misreconstructed. This can be attributed to the issues identified above with sideways-going tracks, which are currently under review by the PANDORA developers.

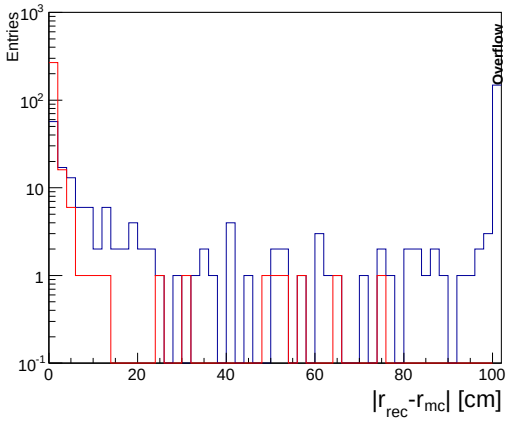

FIG. 81: Distribution of the distance between true and PANDORA reconstructed vertices, for muon neutrino CCQE interactions produced using GENIE and Qscan.

6 Overall layout and space requirements

6.1 General Requirements

The Experimental Hall EHN1, being at present largely occupied by other fixed target experiments, must be extended to host the LAGUNA prototypes. This choice allows not perturbing the existing experimental program in EHN1. Services (i.e. crane, electricity, water, etc...) could still be derived from the existing area, provided that the experiment does not suffer or generates perturbations related to the operation of other experiments or activities in the Hall.

Space requirements:

- >256 m^2 recessed floor space: The LAGUNA LAr prototype is located in a recessed floor region (a pit of ≥16m large, ≥16m long, ˜7m deep) of the extension of the EHN1 experimental hall (EHN1-X).
- 5mx16m = 80m^2 clean assembly + control room
- 5mx16m = 80m^2 unloading area
- 15mx15m should be left open for future developments (could be shared with other users).

The pit can house the prototype in such a way that the detector can receive the beam of charged particles. The geometry and tolerance for the direction of the incoming charge particles are presented in Section 7. The floor of the pit should be designed to support a weight of 800 tons. The detector should be standing on pillars whose number and size must be appropriately chosen. The supporting pillars act as thermal insulation (to avoid freezing of the floor) and as anti-seismic shock absorbers.

6.2 Additional space in pit

An upstream space of 10 m and downstream space of 4 m shall be reserved in the recessed pit to allow for future detector upgrades or prototypes, such as e.g. LBNO near detector prototype.

6.3 Control room

The control room hosts the computers responsible for the data acquisition and the local storage. The control room hosts several screens to monitor the various functions and statuses of the experiment. The control room is the location where physicists take shifts (24/24, 7/7 during beam time). The noise level should be, according to safety rules, such that extended period of stays are possible by staff. The ventilation of the control room should be dimensioned to dissipate up to 50 kW.

6.4 Clean-room

During assembly of the inner detector, the inner vessel shall become a clean room and be connected to an external clean room. The external clean room shall have a section with an external door to bring in preassembled and sealed components. The external clean room is used to open the shipped sealed packages and install individual components inside the inner vessel by means of the 10T crane (see Section 6.10). The environment in these volumes should be a class 1:100'000 (ISO Class 8).

6.5 Access to EHN1-X area

Equipment needed during the various phases of the installation and assembly will be transported by truck, truck-containers or with internal CERN vehicles (likely from the Meyrin site e.g. Blg 182). Unloading from the trucks will be done with the cranes or with forklifts. A convenient and unobstructed road access and a truck-unloading zone accessible from the cranes and with the forklifts should be available. During the initial construction phase of the vessel and the installation of the cryogenic facilities (see Sections 6.6, 6.7 and 6.9), the 40T crane will be used. During the inner detector construction within the clean room, trucks will be unloaded with a forklift. The 10T crane to be located within the clean tent will be used to insert elements into the vessel from the top roof openings.

6.6 Liquid Argon filling and emptying

A liquid argon receiving and transmitting station will be used. The total liquid argon volume is ~500 m^3 or approximately the equivalent amount transported by 25-30 trucks, with a maximum rate of several trucks per day giving a filling or emptying time of ~10 days. The delivered Liquid Argon

shall be of the Welding Grade with following maximum contaminants at the arrival (contaminants at departure + contamination during loading and by truck itself):

- Purity > 99.99% molar
- Oxygen < 4 ppm molar
- Nitrogen < 2 ppm molar
- Water < 1 ppm molar
- Hydrocarbons < 0.5 ppm molar

In order to reduce nuisance and interference caused by the many trucks in the experimental hall, the LAr receiving and transmitting zone should be located externally, outside the experimental hall, and connected with the prototype cryogenic facilities via appropriate vacuum-insulated cryogenic transfer lines. An immersed LAr pump is necessary to empty the vessel (See Section Section 6.9). Heaters will be located inside the vessel to warm up the detector after emptying the liquid argon. Alternatively purging warm argon gas inside the tank can be considered to warm up the inner detector (See Section 6.8). In order to test the aging of the membrane weldings and the potential creation of micro-leaks, which would deteriorate the liquid argon purity even after complete outgassing of the inner detector materials, the vessel will be purposely cycled several times by filling and emptying several times. For an efficient filling and emptying, a local external storage with a capacity of 500m3 LAr should be available, using e.g. nr. 10 cryogenic standard tanks Linde LITS 2 of net capacity 58,500 lt / each[143].

6.7 Liquid argon boiloff recondensation

With the insulation thickness chosen, the average heat input is ˜5 W/m2 and the total heat input (including also the roof input) is about ˜4 kW at LAr temperature. The corresponding boiloff rate is ˜2 ton LAr/day (˜0.3%/day). A cryogenic plant must re-condense the boiloff rate in order to keep the pressure and the level of liquid argon constant. The absolute pressure of the argon remains constant ±1 mbar, and can differ ±75 mbar relative to the atmospheric pressure. In order to avoid contamination of the pure liquid argon, the boiloff will be re-condensed via heat exchangers connected to a nitrogen loop. The re-condensed argon will be purified (see next section) before it is returned to the main vessel. The LAr condensation can be made using liquid nitrogen at 1.5 barg and -187.1°C in a cross current heat exchanger. Liquid nitrogen is introduced at bottom of exchanger and exits on top in gaseous state. Gaseous argon goes at top of exchanger and exits at bottom in liquid form. Gaseous nitrogen is compressed and expanded in the thermodynamic cycle. Preliminary calculations indicate a

thermodynamic efficiency of about 10%, so an electrical power of 40kW is needed to re-condense the boiloff argon.

6.8 Gas phase argon purging and purification

Gas purging in warm phase has been shown to be a very effective method to remove air from the vessel and to reduce the impurities to *ppm* level [71]. A forced gas recirculation and filtration is implemented to remove molecules (mostly water) outgassed from materials at warm temperature, before the detector is cooled down. Flushing gaseous argon at a temperature of ~40-50°C improves the outgassing warming up the surfaces of the detector components.

6.9 Liquid Argon filtration

The free-electron lifetime in liquid must be more than 10 ms in order to drift over 6 m without significant charge amplitude degradation. The impurities in the liquid argon should be less than 0.030 ppb = 30 ppt O_2 equivalent. A filtration system removes the impurities from the commercially delivered bulk argon (see Section Section 6.6) to the required level. Filtration is done by flowing liquid argon through custom-made purification cartridges, made of sections of molecular sieves followed by oxygen-reduced copper oxide powder, such as e.g. those successfully operated in CERN Blg182 in the context of ArDM (CERN RE18). The total volume of liquid argon in the vessel is continuously extracted by an immersed pump, and forced to flow through purification cartridges to filtrate residual impurities and those arising from outgassing materials inside the vessel. The flow of recirculation is at least 20 m^3 LAr/hr. The heat input into the LAr caused by the liquid argon filtration is about 4 kW.

6.10 Cranes

A 40T crane to be used during the initial phases of construction (e.g. tank assembly) and to install the cryogenic and liquid argon filtration plants. A dedicated 10T crane is located within the clean room tent (see Section 6.3) and is used during the phase of installation of the inner detector.

6.11 Ventilation requirements

The temperature and humidity in the hall are controlled by the ventilation and air conditioning system. An exhaust pipe from the recessed floor region is necessary. Dimension and location will be specified in agreement with the safety review. An exchange of the air volume in the recessed pit in which the LBNO LAr prototype is mandatory in order to mitigate the risk of accumulation of argon at the bottom of the recessed pit. The flow is to be defined in agreement with safety regulations. An

increase air flow (two- or three-fold) which should be activated in case of emergency, might be required by safety regulations.

6.12 Cryorefrigeration requirements

The cryorefrigerator has a total of 10 kW cooling power at the LAr temperature. The operation at the full capacity dissipates about 100-150 kW. A totally redundant system (i.e. 20 kW) might be required to satisfy safety regulations. External buffers of LN2 (~30 m^3 LN2/each) are used as cold source to ensure boil-off re-condensation in case of major event on the cryorefrigerator system. The total storage volume of the external buffers will be defined after the safety review. An area of 10x10 m2 must be foreseen to install the cryo-refrigerators.

6.13 HVAC requirements

The total heat dissipation is dominated by the cryo-refrigerators. The heat generated by the cryo-compressors is evacuated via water-cooling (see Section 6.14). The heat dissipated by the rest of the equipment (electronics, power supplies, pumps, control systems, computers, ...) can be removed by air-cooling via an appropriate air conditioning system. The temperature and humidity of the hall should be controlled and stable. The dew point in the hall should be ~10° C.

6.14 Cooling water requirements

The heat generated by the cryo-compressors is evacuated via water-cooling, using a flow of fresh demineralised water is foreseen with standard CERN pressure (4-6 bar) and modest flow (˜1m3/h). The temperature of the inflow water is in the range 6˜10°C.

6.15 Electrical requirements

The area should be equipped with an arrival and a switchboard with protected lines dedicated. In the first phase, the electrical power consumptions are:

- 200 kW 400V/3P for the cryocoolers
- 100 kW 400V/3P for the cryogenic system, pumps, etc.
- 100 kW 400V/3P, 220V/1P for the detector electronics, power supplies, slow control, computers, etc.

The available electric power might be upgraded in a second phase to accommodate magnetised detectors.

6.16 Additional laboratory space at CERN

The chain for the assembly, Q&A and test area to assemble the 36 m2 for the charge readout components requires 30x20 m2 laboratory space. The amount of space and the already existing infrastructure used by CERN RE18 (ArDM experiment) is adequate and can be in large part reused/upgraded.

7 Test beam requirements

The charged particles momentum should be selectable and cover the range 1-20 GeV/c. The beam composition should be pions, muons, electrons, protons,.... The fraction of particles and purity is not critical and is to be optimised later. The electrical charge sign should be selectable. The rate of particles should not exceed 200 Hz. External instrumentation should include counters and chambers to determine the momentum $\Delta p/p \approx 1\%$, provide particle identification (which kind of PID and over which momentum range are to be described later), and early trigger signals. The incoming direction should be at 45 ± 15^{o} w.r.t. the two perpendicular readout views orientations of the LAr TPC, and vertically point to the center of the active volume $\pm15^{o}$.

8 Organization, cost estimate, schedule and risk assessment

8.1 Organisation

8.2 Cost estimate

The total estimated cost of the LAGUNA $6 \times 6 \times 6$ m^3 LAr prototype is presented and detailed in Table VIII. The figures based on preliminary discussion with industrial partners and on extensive experience of the groups on smaller scale prototypes are assumed to have an error at the level of 20-30%.

TABLE VIII: Total estimated cost of the LAGUNA $6 \times 6 \times 6$ m^3 LAr prototype

Item	Nr.	Cost (CHF)	Remark
Grand Total		**x'xxx'xxx**	bargain

8.3 Assembly schedule

8.4 Risk assessment

A set of measures will be implemented to ensure H&S of people, protect equipment, and to mitigate risks associated to the storage and process of large amounts of cryogenic liquids. Additional equipment might be necessary as the results of detailed risk analyses and CERN specific safety regulations. Fire hazards are expected to be predominantly located in specific areas of the facility such as (1) the electronic racks located on top of the detector and (2) the high current cryogenic facilities. Measures to limit fire propagation from those areas might be required. The cryogenic infrastructure should be separated and protected from the regions of potential fire hazard. CERN is expected to contribute to the infrastructure resulting from the CERN safety rules (see e.g. CERN Safety Instruction IS 47 - The use of cryogenics fluids, `http://edms.cern.ch/file/335812/LAST_RELEASED/IS47_E.pdf`). CERN provides and installs remote cabinets, which are connected to appropriately located ODH and fire detectors, and which the CERN fire brigade remotely monitors. The building extension is equipped with fire detectors and evacuation alarms. CERN takes the responsibility for the measures needed to mitigate risk interference between the LBNO prototypes and potential other experiments or equipment to be installed in the EHN1 extension hall. The present design concept might be affected by so-far unforeseen and additional requirements set by safety regulations and identified by safety reviews. CERN will take possible measures to implement these additional requirements.

8.5 Data storage and computing

Gigabit Ethernet connections to the CERN backbone are expected. The needed storage of raw data in CASTOR of the order of 100TB per year of running.

9 Conclusions

Acknowledgements

We are grateful to the CERN Management for their encouragements, recognizing the importance of CERN in the coherent definition of a potential future program for the European neutrino community.

References

[1] A. Stahl *et al.*, CERN Report No. CERN-SPSC-2012-021. SPSC-EOI-007, 2012 (unpublished).

[2] C. Rubbia, (1977).

[3] E. Aprile, K. Giboni, and C. Rubbia, Nucl.Instrum.Meth. **A241**, 62 (1985).

[4] ICARUS-Milano Collaboration, F. Arneodo *et al.*, Phys.Rev. **D74**, 112001 (2006), physics/0609205.

[5] P. Cennini *et al.*, Nucl.Instrum.Meth. **A345**, 230 (1994).

[6] F. Arneodo *et al.*, Nucl.Instrum.Meth. **A498**, 292 (2003).

[7] ICARUS Collaboration, S. Amerio *et al.*, Nucl.Instrum.Meth. **A527**, 329 (2004).

[8] F. Arneodo *et al.*, Nucl.Instrum.Meth. **A508**, 287 (2003).

[9] ICARUS Collaboration, S. Amoruso *et al.*, Eur.Phys.J. **C33**, 233 (2004), hep-ex/0311040.

[10] S. Amoruso *et al.*, Nucl.Instrum.Meth. **A516**, 68 (2004).

[11] ICARUS Collaboration, S. Amoruso *et al.*, Nucl.Instrum.Meth. **A523**, 275 (2004).

[12] ICARUS Collaboration, A. Ankowski *et al.*, Eur.Phys.J. **C48**, 667 (2006), hep-ex/0606006.

[13] ICARUS Collaboration, A. Ankowski *et al.*, Acta Phys.Polon. **B41**, 103 (2010), 0812.2373.

[14] C. Rubbia *et al.*, JINST **6**, P07011 (2011), 1106.0975.

[15] A. Rubbia, p. 321 (2004), hep-ph/0402110.

[16] A. Rubbia, J.Phys.Conf.Ser. **171**, 012020 (2009), 0908.1286.

[17] A. Badertscher *et al.*, JINST **8**, P04012 (2013), 1301.4817.

[18] A. Badertscher *et al.*, JINST **7**, P08026 (2012), 1204.3530.

[19] A. Badertscher *et al.*, Nucl.Instrum.Meth. **A641**, 48 (2011), 1012.0483.

[20] A. Badertscher *et al.*, Nucl.Instrum.Meth. **A617**, 188 (2010), 0907.2944.

[21] RD51 Collaboration, M. Chefdeville, J.Phys.Conf.Ser. **309**, 012017 (2011).

[22] F. Sauli, Nucl.Instrum.Meth. **A386**, 531 (1997).

[23] Y. Giomataris, P. Rebourgeard, J. Robert, and G. Charpak, Nucl.Instrum.Meth. **A376**, 29 (1996).

[24] A. Breskin *et al.*, Nucl.Instrum.Meth. **A598**, 107 (2009), 0807.2026.

[25] W. Willis and V. Radeka, Nucl.Instrum.Meth. **120**, 221 (1974).

[26] B. A. Younglove and H. J. M. Hanley, J. Phys. Chem. Ref. Data **15**, 1323 (1986).

[27] C. Ramsauer, Ann. Phys **369**, 513 (1921).

[28] H. N. Kucukarpaci and J. Lucas, J. Phys. D **14**, 2001 (1981).

[29] S. Biagi, Nucl. Instr. and Meth. A **283**, 716 (1989).

[30] F. Sauli, CERN 77-09; Academic lecture (1977).

[31] Y. Nakamura and M. Kurachi, J. Phys. D **21**, 718 (1988).

[32] M. Suzuki, T. Taniguchi, and H. Tagashira, J. Phys. D **23**, 842 (1990).

[33] J. Lekner, Phys. Rev. **158**, 130 (1967).

[34] W. Walkowiak, Nucl. Instr. and Meth. A **449**, 288 (2000).

[35] A.Badertscher *et al.*, arXiv:0811.3384v1 [physics.ins-det] (2008).

[36] S. Amoruso *et al.*, Nucl. Instr. and Meth. A , 68 (2004).

[37] E. Buckley *et al.*, Nucl. Instr. and Meth. A **275**, 364 (1989).

[38] L. S. Miller, S. Howe, and W. E. Spear, Phys. Rev. **166**, 871 (1967).

[39] A. Badertscher *et al.*, JINST **7**, P08026 (2012).

[40] D. W. Swan, Proc. Phys. Soc. **83**, 659 (1964).

[41] E. Shibamura, T. Takahashi, S. Kubota, and T. Doke, Phys. Rev. A **20**, 2547 (1979).

[42] A. Einstein, Ann. Phys **322**, 549 (1905).

[43] A. Rubbia, arXiv:hep-ph/0402110v1 (2004).

[44] B. A. Dolgoshein *et al.*, JETP Lett. **11**, 351 (1970).

[45] E. M. Gushchin *et al.*, Sov. Phys. JETP **55**, 860 (1982).

[46] A. Borghesani *et al.*, Phys. Lett. **149**, 481 (1990).

[47] E. L. Murphy and R. H. Good, Jr, Phys. Rev. **102**, 1464 (1956).

[48] T. Sometani and K. Hasebe, Am. J. Phys. **45**, 918 (1977).

[49] A. I. Bolozdynya, Nucl. Instr. Meth. **A422**, 314 (1999).

[50] R. Lagushenko and J. Maya, J. Appl. Phys. **55**, 3293 (1984).

[51] T. H. V. T. Dias *et al.*, J. Phys. D: Appl. Phys. **19**, 527 (1986).

[52] C. Monteiro, J. Lopes, J. Veloso, and J. dos Santos, Phys. Lett. B **668**, 167 (2008).

[53] E. M. Gushchin *et al.*, Sov. Phys. JETP **55**, 650 (1982).

[54] C. M. B. Monteiro *et al.*, IEEE Trans. Nucl. Sci. **48**, 1081 (2001).

[55] E. Aprile *et al.*, arXiv:1104.2549v1 [astro-ph.CO] (2010).

[56] P. Benetti *et al.*, Astroparticle Physics **28**, 495 (2008).

[57] A. Rubbia, J.Phys.Conf.Ser. **39**, 129 (2006), hep-ph/0510320.

[58] Y. P. Raizer, *Gas Discharge Physics* (Springer-Verlag, 1991).

[59] S. F. Biagi, Nucl. Instr. Meth. **A421**, 234 (1999).

[60] R. Veenhof, `http://garfield.web.cern.ch/garfield` [11/2011].

[61] I. Velchev, W. Hogervorst, and W. Ubachs, J. Phys. B: At. Mol. Phys. **32**, L511 (1999).

[62] T. Ficker, Acta Polytechnica **47**, 31 (2007).

[63] W. H. Furry, Phys. Rev. **52**, 569 (1937).

[64] D. W. Swan, Proc. Phys. Soc. **82**, 74 (1963).

[65] G. Bakale, U. Sowada, and W. Schmidt, J. Phys. Chem. **80**, 2556 (1976).

[66] S. Suzuki, Liquid Argon Purification for ICARUS, in *Proceeding of the 4^{th} Miniworkshop on Low Level Couning and Space-Based use of Liquid Argon and Xenon Detectors*, Waseda University, 1990.

[67] R. Andrews *et al.*, Nucl. Instr. and Meth. A **608**, 251 (2009).

[68] MicroBooNE Collaboration, H. Chen *et al.*, (2007).

[69] LBNE Collaboration, T. Akiri *et al.*, arXiv (2011), 1110.6249.

[70] LAGUNA Collaboration, A. Rubbia, Acta Phys.Polon. **B41**, 1727 (2010).

[71] A. Curioni *et al.*, J.Phys.Conf.Ser. **308**, 012024 (2011), 1009.4073.

[72] A. Breskin *et al.*, Nucl. Instrum. Meth. A **598**, 107 (2009).

[73] F. Resnati, *Modeling, design and first operation of the novel double phase LAr LEM-TPC detector*, PhD thesis, ETH Zurich, 2012.

[74] A. Bressan *et al.*, Nucl. Instrum. Meth. A **425**, 254 (1999).

[75] W. Shockley, J. Appl. Phys. **9**, 635 (1938).

[76] S. Ramo, Proc. of the IRE **27**, 584 (1939).

[77] Y. Giomataris, P. Rebourgeard, J. Robert, and G. Charpak, Nuclear Instruments and Methods in Physics Research Section A: Accelerators, Spectrometers, Detectors and Associated Equipment **376**, 29 (1996).

[78] I. Giomataris *et al.*, Nuclear Instruments and Methods in Physics Research Section A: Accelerators, Spectrometers, Detectors and Associated Equipment **560**, 405 (2006).

[79] A. Delbart, Nuclear Instruments and Methods in Physics Research Section A: Accelerators, Spectrometers, Detectors and Associated Equipment **623**, 105 (2010), ¡ce:title¿1st International Conference on Technology and Instrumentation in Particle Physics¡/ce:title¿.

[80] A. Delbart *et al.*, J.Phys.Conf.Ser. **308**, 012017 (2011).

[81] W. Walkowiak, Nucl.Instrum.Meth. **A449**, 288 (2000).

[82] V. Ushakov, Behavior of liquids in strong electric fields, in *Impulse Breakdown of Liquids*, Power Systems, pp. 1–51, Springer Berlin Heidelberg, 2007.

[83] S. Horikawa *et al.*, J.Phys.Conf.Ser. **308**, 012027 (2011), 1009.4908.

[84] E. Bechetoille and H. Mathez, WOLTE 8, Workshop On Low Temperature Electronics , [in2p3-00339737] (2008).

[85] C. Girerd *et al.*, arXiv:0906.2325 [physics.ins-det] (2009).

[86] P. group, (2006).

[87] T. Doke, K. Masuda, and E. Shibamura, Nuclear Instruments and Methods in Physics Research Section A: Accelerators, Spectrometers, Detectors and Associated Equipment **291**, 617 (1990).

[88] S. Kubota, M. Hishida, and J. Raun, Journal of Physics C: Solid State Physics **11**, 2645 (1978).

[89] T. Strickler and E.T.Arakawa, J. Chem. Phys. **41**, 1783 (1964).

[90] ArDM Collaboration, V. Boccone *et al.*, JINST **4**, P06001 (2009), 0904.0246.

[91] ArDM Collaboration, C. Amsler *et al.*, JINST **5**, P11003 (2010), 1009.3641.

[92] ArDM Collaboration, A. Marchionni *et al.*, J. Phys. Conf. Ser. **308**, 012006 (2011), 1012.5967.

[93] J. E. Campagne *et al.*, Journal of Instrumentation **6**, C01081 (2011).

[94] S. C. Di Lorenzo *et al.*, (2009), 0912.1269.

[95] B. Genolini *et al.*, Nuclear Instruments and Methods in Physics Research Section A: Accelerators, Spectrometers, Detectors and Associated Equipment **610**, 249 (2009), ¡ce:title¿New Developments In Photodetection NDIP08¡/ce:title¿ ¡xocs:full-name¿Proceedings of the Fifth International Conference on New Developments in Photodetection¡/xocs:full-name¿.

[96] R. Acciarri *et al.*, Nucl. Phys. Proc. Suppl. **197**, 70 (2009).

[97] P. Redhead, J. Vac. Sci. Technol. A **13**, 2791 (1995).

[98] J. F. O'Hanlon, *A User's Guide to Vacuum Technology*, 3 ed. (John Wiley & Sons Inc., 2003).

[99] P. Redhead, J. Vac. Sci. Technol. A **13**, 467 (1995).

[100] R. Calder and G. Lewin, British Journal of Applied Physics **18**, 1459 (1967).

[101] A. Badertscher *et al.*, arXiv:1301.4817 [physics.ins-det] (2013).

[102] D. Edwards, J. Vac. Sci. Technol. **14**, 1030 (1977).

[103] Lawrence Berkley National Laboratory Report No., , 1979 (unpublished).

[104] Y. Koyatsu, H. Miki, and F. Watanabe, Vacuum **47**, 709 (1996).

[105] M.Wong, http://home.fnal.gov/~mlwong/outgas_rev.htm (2002 last checked: July 2012).

[106] R. S. Barton and R. P. Govier, J. Vac. Sci. Technol. **2**, 113 (1965).

[107] E. D. Erikson, T. G. Beat, D. D. Berger, and B. A. Frazier, J. Vac. Sci. Technol. A **2**, 206 (1984).

[108] ICARUS-TM-98/14 Report No., , 1998 (unpublished).

[109] A. Curioni *et al.*, J. Phys. Conf. Ser. **308**, 012024 (2011), 1009.4073.

[110] R. E. Trent, Fundamentals of Molecular Sieve Design, in *Presented at the American Institute of Chemical Engineers Spring National Meeting*, Huston, Texas, 1992.

[111] R. M. Barrer and W. I. Stuart, Proc. R. Soc. Lond. A **249**, 464 (1959).

[112] R. M. Dell, F. S. Stone, and P. F. Tiley, Trans. Faraday Soc. **49**, 195 (1953).

[113] T. N. Rhodin, Journal of the American Chemical Society **72**, 5102 (1950), http://pubs.acs.org/doi/pdf/10.1021/ja01167a079.

[114] A. Bueno *et al.*, JHEP **0704**, 041 (2007), hep-ph/0701101.

[115] The ICARUS-Milano Collaboration, F. Arneodo *et al.*, Phys. Rev. D **74**, 112001 (2006).

[116] A. Ankowski *et al.*, Eur. Phys. J. C **48**, 667 (2006).

[117] Y. Ge *et al.*, ETH Zurich Report No. 3-5, 2003 (unpublished).

[118] J. Rico, *First study of the stopping muon sample with the ICARUS T600 detector*, PhD thesis, ETH Zurich, 2002.

[119] A. Martinez, *Study of accelerator neutrino interactions in a liquid argon TPC*, PhD thesis, Universidad de Granada, 2007.

[120] R. Brun and F. Rademakers, Nucl. Instrum. Meth. A **389**, 81 (1997).

[121] C. Anderson *et al.*, JINST **7**, P10019 (2012).

[122] D. Lussi, Qscan, http://indico.cern.ch/conferenceOtherViews.py?view=standard&confId=129268 [05/2012], 2011.

[123] I. Hrivnacova, J. Phys. Conf. Ser. **396**, 022024 (2012).

[124] S. Agostinelli *et al.*, Nuclear Instruments and Methods in Physics Research Section A: Accelerators, Spectrometers, Detectors and Associated Equipment **506**, 250 (2003).

[125] J. Apostolakis *et al.*, GEANT4 Physics Lists for HEP, in *Nucl. Sc. Symp. Conf. Rec. IEEE*, pp. 833–836, 2008.

[126] O. Araoka *et al.*, J. Phys. Conf. Ser. **308**, 012008 (2011), 1105.5818.

[127] W. H. Press *et al.*, *Numerical recipes in C (2nd ed.): the art of scientific computing* (Cambridge University Press, New York, NY, USA, 1992).

[128] P. Hough, Method and means for recognizing complex patterns, U.S. Patent 3.069.654, 1962.

[129] M. Thomson, Nuclear Instruments and Methods in Physics Research Section A: Accelerators, Spectrometers, Detectors and Associated Equipment **611**, 25 (2009).

[130] M. Thomson, LAr Event Reconstruction with the PANDORA Software Development Kit. Talk given at UK Liquid Argon meeting in Manchester on 28/11/12., 2012.

[131] see Equation 2.2 for a definition of reconstructed energy

[132] The actual function is $u(E) = 1.004 \cdot E^5 - 5.083 \cdot E^4 + 10.082 \cdot E^3 - 10.280 \cdot E^2 + 6.431 \cdot E - 0.016$ for $[E] =$ kV/cm and $[u] =$ mm/μs

[133] It was manufactured at ELTOS Circuiti Stampati Professionali, Italy (http://www.eltos.com/).

[134] COMSOL Multiphysics software, http://www.comsol.com

[135] `http://rd51-public.web.cern.ch/RD51-Public/Welcome.html`.

[136] The product in use is *FLUKA Copper(II)oxide purum, 98.0% (RT); 61202* from Sigma-Aldrich Chemie GmbH

[137] http://root.cern.ch

[138] https://cdcvs.fnal.gov/redmine/projects/larsoftsvn

[139] http://www-microboone.fnal.gov

[140] Long Baseline Neutrino experiment, http://lbne.fnal.gov

[141] http://root.cern.ch/drupal/content/vmc

[142] http://geant4.cern.ch

[143] http://www.linde-engineering.com/en/plant_components/cryogenic_tanks/index.html